



Delft University of Technology
Department of Geoscience & Engineering

The in-situ stress field in the Netherlands:
Regional trends, local deviations and an analysis of the stress
regimes in the northeast of the Netherlands

In partial fulfilment of the requirements for the degree of

Master of Science
in Applied Earth Sciences

by

Author:
Eelco Mechelse (4243900)

Supervisors:
Prof. Dr. Giovanni Bertotti
Dr. Marc Hetteema

Delft, the Netherlands
4th of August 2017

Title : “The in-situ stress field in the Netherlands: Regional trends, local deviations and an analysis of the stress regimes in the northeast of the Netherlands”

Author(s) : Eelco Mechelse

Date : 4th of August 2017

Professor(s) : Prof. Dr. Giovanni Bertotti

Supervisor(s) : Prof. Dr. Giovanni Bertotti
Dr. Marc Hettema

Assessment Committee : Prof. Dr. Giovanni Bertotti (Applied Geology)
Dr. Auke Barnhoorn (Applied Geophysics & Petrophysics)
Dr. Paul van den Hoek (Petroleum Engineering)
Dr. Marc Hettema (EBN B.V.)

Postal Address : Section for Applied Geology
Department of Geoscience & Engineering
Faculty of Civil Engineering & Geosciences
Delft University of Technology
P.O. Box 5028
The Netherlands

Telephone : +31 15 2781328 (Secretary)

Copyright © 2017 Section for Applied Geology

Alle rechten voorbehouden. Niets uit deze uitgave mag worden verveelvoudigd, opgeslagen in een geautomatiseerd gegevensbestand, of openbaar gemaakt, in enige vorm of op enige wijze, hetzij elektronisch, mechanisch, door fotokopieën, opnamen, of op enige andere manier, zonder voorafgaand schriftelijke toestemming van de uitgever.

All rights reserved. No part of this publication may be reproduced, stored in a retrieval system, or transmitted, in any form or by any means, electronic, mechanics, photocopying, recording or otherwise, without the prior written permission of the Section for Applied Geology.

Abstract

Knowledge of the state of stress is of significant importance to have a thorough understanding of subsurface geomechanics. The World Stress Map (WSM) is the main source of present-day stress data in Western Europe and indicates a regional NW-SE maximum horizontal stress (S_H) trend for the Netherlands. However, for more local studies the WSM lacks the required resolution. Therefore, the first objective of this research is to expand the Dutch Stress Map (DSM) database in which S_H orientations are collected. As such, a better understanding can be obtained of the horizontal stress field with depth and the S_H orientations that deviate from the regional trend. In addition, this research aims to characterize the in-situ stress regimes with depth in the Groningen field, using different one-dimensional stress models.

This research first highlights the importance of the stress state and indicates which in-situ stress information is currently lacking in the Netherlands. Moreover, it is shown how stress-induced borehole features serve as basis for the determination of horizontal stress directions. The datasets used to expand the DSM database are presented, after which an extensive analysis is performed on the collected S_H orientations. Subsequently, the stress magnitudes are quantified by studying the sensitivity of the in-situ stress regime to different 1D stress models. Moreover, the workflow is described for developing a 3D geomechanical model, which can serve as basis for future studies.

The research shows that the DSM database is expanded with 86 new boreholes across the Dutch on- and offshore regions. The analysis of the database indicates a dominant NW-SE S_H orientation, both spatially and with depth. In most stratigraphic groups, the S_H direction falls within the range of $315^\circ \pm 22.5^\circ$, although a larger degree of variation is observed in the post-salt stratigraphies. On a local scale, two case studies show that S_H orientations, which deviate from the regional NW-SE trend, can be related to the presence of a salt structure and a normal fault. The 1D in-situ stress models all indicate a normal faulting stress regime at reservoir depth (Rotliegend) and deeper. In the interval between the reservoir and Earth's surface, no unambiguous stress regime is identified as the regime is more sensitive to the different boundary conditions applied.

Acknowledgments

I would like to thank my supervisors Prof. Dr. Giovanni Bertotti (TU Delft) and Dr. Marc Hetteema (EBN B.V.) for giving me the unique opportunity to perform this research, but also to thank them for their enthusiasm, constructive criticism and willingness to give their time and effort. I am grateful for the support given by Guido Hoetz and Bastiaan Jaarsma (EBN B.V.) and the opportunities to discuss my findings with them. I want to express my gratitude for the support of Johan ten Veen (TNO) and Rob van Eijs (NAM) and their time to visit EBN and listen to my results. Their professional input has been greatly appreciated and was very useful during my time at EBN. In addition, I would like to thank Dr. Auke Barnhoorn (TU Delft) and Dr. Paul van den Hoek (TU Delft) for their willingness to be part of my assessment committee.

During this research, I have had the pleasure to use Petrel, Abaqus/CAE and JewelSuite, and therefore I would like to thank the companies Schlumberger, Dassault Systèmes and Baker Hughes, respectively. My special thanks go to Quinten Boersma (TU Delft) as I was fortunate to be assisted by Quinten during the usage of the Abaqus/CAE software. His knowledge and suggestions have been very valuable as well as his willingness to answer all my questions.

At EBN, I would also like to thank Jan Lutgert for sharing his valuable knowledge in the field of image logs and providing me useful coursework on image log interpretation. The access to Dutch subsurface data and advanced Petrel models would not have been possible without the help of Marloes Kortekaas and Marten ter Borgh, and therefore their assistance has been greatly appreciated. This appreciation is extended to all the other staff and interns for letting me feel at home the past nine months.

Finally, I would like to thank my mother and sister for their intrinsic support during my five years at Delft University of Technology. Special thanks to my best friend Darcy de Bijl for boosting my motivation by spending many hours in the flight simulator, watching F1 races and sharing other unforgettable moments during high school and university.

Eelco Mechelse
4th of August 2017, Voorschoten

i. Table of contents

Acknowledgments.....	iv
1. Introduction	1
2. The stress field in the Netherlands.....	2
2.1 Importance of the state of stress	2
2.2 What is not known in the Dutch stress field?.....	2
3. Identification of stress-induced borehole features	4
3.1 Compressive and tensile borehole failure	4
3.2 Image logging tools	4
3.2.1 Electrical imaging tools.....	5
3.2.2 Acoustic imaging tools.....	6
3.3 Four-arm caliper tools	7
3.4 Sonic logging tools.....	8
4. Datasets.....	9
4.1 Data collection.....	9
4.1.1 World Stress Map dataset	9
4.1.2 TNO dataset.....	9
4.1.3 Rondel and Everaars dataset.....	10
4.1.4 Van Eijs dataset	10
4.2 Comparison of datasets.....	10
4.3 Quality ranking system	13
5. Dutch Stress Map analysis.....	15
5.1 Overall horizontal stress orientations	15
5.2 Formation specific stress analysis	17
5.3 Pre- and post-salt stratigraphy stress analysis	18
5.4 Deviated wells stress analysis	19
6. Local stress deviations in the Dutch Stress Map	20
6.1 Base case scenario.....	20
6.2 Salt structures	22
6.3 Normal faulting	27
7. In-situ stress regimes in the northeast of the Netherlands.....	30
7.1 Overview of models.....	30
7.1.1 Gravity-only models	31
7.1.2 Gravity-tectonic models	32
7.1.3 Tectonic strain model.....	33
7.2 Results	34
7.2.1 Gravity-only models	34
7.2.2 Gravity-tectonic models	36
7.2.3 Tectonic strain model.....	37
7.2.4 Comparison of models	38

8. 3D Geomechanical modelling.....	39
8.1 Methodology	39
8.1.1 Model set-up	39
8.1.2 Modelling strategy	41
8.2 Results	41
8.3 Model accuracy and uncertainties	44
9. Discussion.....	46
9.1 Overall horizontal stress orientations	46
9.2 Local stress deviations in the Dutch Stress Map	46
9.3 In-situ stress regimes in the northeast of the Netherlands.....	47
9.4 3D Geomechanical modelling.....	48
10. Conclusions	49
11. Recommendations	50
References.....	51
Appendix A: World Stress Map project	56
Appendix B: Workflow TNO dataset	59
Appendix C: Dutch Stress Map database	61
Appendix D: Quality ranking system	72
Appendix E: Dutch Stress Maps.....	74
Appendix F: Sources 1D geomechanical model.....	84
Appendix G: Workflow 3D geomechanical model.....	85
Appendix H: Sources Dutch Stress Map database.....	87

i. List of Figures

Figure 1: Directions of the maximum horizontal stress as displayed by the orientation of the symbols. All data points are either based on break-outs or drilling-induced fractures. The colour of each symbol represents the stress regime at a specific depth, whereas the length of the symbol indicates the data quality as defined by the WSM (Heidbach et al., 2016b).	3
Figure 2: Example of break-outs on an electrical image log in the E18-A field (source: Appendix H).	5
Figure 3: Example of drilling-induced fractures on the logs of a FMI tool (Heidbach et al., 2016a).	6
Figure 4: Section of an acoustic image log (UBI) in the Dutch E17-FA field. The four pairs of break-outs are highlighted by the blue boxes (source: Appendix H).....	7
Figure 5: Sketch of the sonic logging tool set-up to determine stress-induced acoustic anisotropy in a formation (Haldorsen et al., 2006).	8
Figure 6: Horizontal stress data has been found in 86 new boreholes. More than 50% of these wells are drilled (sub)-vertical ($< 10^\circ$), 29% are deviated wells, whereas for 20% of the wells the deviation angle could not be determined.	11
Figure 7: (a) Map of the Dutch on- and offshore areas indicating the 45 boreholes of the WSM dataset. (b) Map showing the WSM dataset and the 86 boreholes that have been added to the DSM database. The blue-filled triangles indicate the 86 new boreholes.....	12
Figure 8: Frequency distribution indicating the number of stress data points per stratigraphic group for the WSM dataset and the DSM database.	12
Figure 9: Quality distribution of the (sub)-vertical wells in the TNO, Rondel and Everaars (1993) and Van Eijs (2015) datasets. A-quality wells have the highest quality of stress data, whereas E-quality wells need to be treated with more caution (Heidbach et al., 2016a).....	14
Figure 10: Map indicating the quality labels of the 61 (sub)-vertical wells found in the datasets of TNO, Rondel and Everaars (1993) and Van Eijs (2015).	14
Figure 11: Half rose diagram of the S_H directions based on all stress data in the DSM database.....	15
Figure 12: The Dutch Stress Map in which the symbols indicate the orientation of S_H . For each well, this map shows the average S_H direction per stratigraphy. If stress-induced features have been found in multiple formations, this map only shows the S_H orientation in the shallowest formation.	16
Figure 13: Half rose diagrams of the S_H directions based on stress data in the (a) Chalk Group, (b) Rijnland Group, (c) Scruff Group, (d) Schieland Group, (e) Upper Germanic Trias Group, (f) Lower Germanic Trias Group, (g) Zechstein and (h) Rotliegend.	17
Figure 14: Half rose diagrams of the S_H directions based on stress data in the (a) Limburg Group and (b) undefined stratigraphies.	18
Figure 15: Half rose diagrams of the S_H directions based on stress data in (a) the pre-salt stratigraphies and (b) the post-salt stratigraphies. The pre-salt stratigraphy includes the Limburg Group and Rotliegend, whereas the post-salt stratigraphy includes the Lower and Upper Germanic Trias Groups, Schieland Group, Scruff Group, Rijnland Group and Chalk Group.	19
Figure 16: Half rose diagram of the S_H directions based on stress data in the deviated wells ($> 10^\circ$) of the DSM database.	19
Figure 17: Zechstein thickness map including the major faults (in black) in the area of well K05-12. Faults have been mapped by NLOG (2015) and the location of the study area is displayed in the inset.	21

Figure 18: Cross line through well K05-12 in which the bases of the main stratigraphic groups are highlighted in two-way travel time. In the vicinity of the well, two normal faults and their displacement are indicated in black.	21
Figure 19: Distribution of break-outs and drilling-induced fractures with depth in well K05-12. Over an interval of 450 m, the variation in the horizontal stress directions is very limited. The blue dashed line indicates the regional NW-SE S_H trend. ROCL = Silverpit Formation; ROSL = Slochteren Formation; DC = Limburg Group.	22
Figure 20: Zechstein thickness map of the area surrounding well X.	23
Figure 21: Cross line through well X in which the bases of the main stratigraphic groups are highlighted in two-way travel time. At the crest of the salt structure, the Chalk and Rijnland Group are located directly below the base of the North Sea Group, which is not visualized at this scale.	23
Figure 22: Distribution of acoustic analysis data in well X. The red dashed line indicates the observed trend, whereas the blue dashed line indicates the regional NW-SE S_H trend. CK = Chalk Group; KN = Rijnland Group; ZE = Zechstein.	24
Figure 23: Horizontal depth slice at the Chalk Group data point (-1404 m). The white arrow indicates the observed N-S S_H orientation, whereas the black dashed arrow displays the expected S_H direction normal to the boundary of the salt structure. The boundary between the surrounding sediment and the salt structure (ZE) is highlighted with the black dashed circle.	25
Figure 24: Depth slice at the Rijnland Group data point (-1444 m) in which the white arrow indicates the observed E-W S_H orientation.	25
Figure 25: Depth slice at the Zechstein data point (-1464 m). The white arrow indicates the observed ENE-WSW S_H orientation.	26
Figure 26: Depth slice at the Zechstein data point (-1510 m) in which the white arrow indicates the observed NW-SE S_H orientation.	26
Figure 27: Zechstein thickness map including the major faults (in black) in the area of well L09-12. Faults have been mapped by NLOG (2015).	27
Figure 28: Cross line through well L09-12 in which the bases of the main stratigraphic groups are highlighted in two-way travel time. The normal fault and its major offset (± 346 m) on the northern side of the well has clearly affected the Lower and Upper Germanic Trias Groups.	28
Figure 29: (a) Distribution of break-outs with depth in well L09-12. The blue dashed line indicates the regional NW-SE S_H trend. RN = Upper Germanic Trias Group; RB = Lower Germanic Trias Group. (b) Map view of L09-12 with respect to the east-west trending normal fault in black. The mean S_H direction is given in black, whereas the blue dashed line shows the regional NW-SE S_H trend.	29
Figure 30: (a) Map view: In the vicinity of faults, which are mechanically stiffer than the host rock, S_H trajectories orient normal to the fault plane. (b) In case of mechanically weak faults, S_H trajectories align parallel to the fault plane.	29
Figure 31: Map of the northeast of the Netherlands in which gas and oil fields are coloured green and red, respectively. Well ZRP-01 is indicated with the black solid circle.	30
Figure 32: Model 1 - Stress profiles and pore pressure as function of depth, based on the stratigraphy of well ZRP-01. NU: Upper North Sea Group; NL = Lower North Sea Group; CK = Chalk Group; KN = Rijnland Group; RB = Lower Germanic Trias Group; ZE = Zechstein; RO = Rotliegend; DC = Limburg Group.	34
Figure 33: Model 2 – Stress profiles and pore pressure as function of depth. An ESR of one has been assumed for the horizontal stresses in the Zechstein formation (Y, XXXX).	35
Figure 34: Model 3 – Stress profiles and pore pressure as function of depth.	35

Figure 35: Model 4a - Stress profiles and pore pressure as function of depth for a tectonic stress component of 5 MPa. The arrows indicate the three different in-situ stress regimes.	36
Figure 36: Model 4b - Stress profiles and pore pressure as function of depth for a tectonic stress component of 10 MPa.....	36
Figure 37: Model 5 - Stress profiles and pore pressure as function of depth for a tectonically induced strain of $2E^{-4}$	37
Figure 38: S_H/S_h ratio as function of depth for the five different in-situ stress models.	38
Figure 39: (Left) Top view of the base of the Upper North Sea Group. The grey rectangle indicates the area of which a 3D geomechanical model has been made. All maps show elevation with negative values, whereas depths below surface are displayed by positive values. (Right) Within the model, the base Lower Germanic Trias Group (= top Zechstein) clearly illustrates the presence of a salt diapir and smaller salt structures.	39
Figure 40: The resulting 3D model in which no faults have been incorporated.	40
Figure 41: (Left) Top view of the 3D model which indicates that the boundaries do not allow displacement in the x- and y-direction. (Right) Cross-section in the YZ plane shows that the base of the model is also fixed.....	40
Figure 42: 1D Initial stress state for Case A based on the assumptions and equations of Model 1 (Section 7.1.1). OB = Overburden.	41
Figure 43: Zechstein thickness map of the modelled area. The model boundary is indicated with the black box, whereas the three analysed regions of 5 x 5 km are highlighted by the smaller black squares.	42
Figure 44: Pressure-depth plots at the three different locations when running case A. The hydrostatic pore pressure curve has been added manually and is not an output of the actual simulation.	43
Figure 45: Simulation case A: Distribution of the vertical, minimum and maximum horizontal stress in the XY plane when displaying the data of the entire field (44 x 24 km) between 4 and 4.5 km depth.....	44
Figure 46: Vector field of (a) the maximum horizontal stress and (b) the minimum horizontal stress at a depth of 3051 m. The same stress orientations are observed at all other depths.	44

ii. List of Tables

Table 1: An overview of the number of wells with S_H directions per dataset. A distinction is made between all wells (including deviated wells) and only (sub)-vertical wells.	10
Table 2: Quality ranking system for break-outs and drilling-induced fractures in a well. For the B- to D-quality labels, multiple conditions are stated but a well needs to satisfy only one of these conditions. ...	13
Table 3: Mean S_H direction and standard deviation per stratigraphy by applying circular statistics (Mardia, 1972).	18
Table 4: Mean S_H direction and standard deviation of the pre- and post-salt stratigraphies.	18
Table 5: Stratigraphic column of ZRP-01, as well as the corresponding bulk and fluid densities, and elastic properties.	31
Table 6: Overview of the assumptions and corresponding equations for the five different in-situ stress models.	33
Table 7: Depth intervals, relative stress magnitudes and the corresponding in-situ stress regime for (left) Model 4a with a tectonic stress component of 5 MPa, and (right) Model 4b with a tectonic stress component of 10 MPa.	37
Table 8: Rock and elastic properties for the four different units in the 3D geomechanical model (source: Appendix F).	40
Table 9: Case A: In-situ stress values at a depth of 5 km in the three different areas.	43
Table 10: Initial stress values at a depth of 5 km, as shown in Figure 42.	43
Table 11: Available data on depth uncertainties in the modelled area of Section 8.2 (NLOG, 2015).	45

1. Introduction

A proper characterization of the present-day stress state (directions and magnitudes) is of crucial importance for understanding geomechanical processes in the subsurface. In-situ stresses play an important role in understanding and predicting seismicity related to production/injection in hydrocarbon fields and geothermal projects. Besides that, knowledge of the stress state is of key essence during the process of well planning such that, for example, wellbore stability issues can be minimized.

The present-day stress state can either be measured (direct or indirect) or derived from methods such as stress-induced borehole features (Klein & Barr, 1986). Measurement techniques including hydraulic fracturing and overcoring provide information on both the in-situ stress orientation and magnitude. On the other hand, stress-induced borehole features such as break-outs and drilling-induced fractures are often only used to determine the horizontal stress orientation (Heidbach et al., 2016a). In any case, this stress data serves as input for the World Stress Map (WSM), which is the main source of regional present-day stress data in Western Europe and the Netherlands.

Numerous studies (e.g. Müller et al., 1992; Van Eijs & Dalfsen, 2004) have shown that a general NW-SE maximum horizontal stress (S_H) orientation can be observed in Western Europe and the Netherlands. However, for more local analyses, the WSM lacks the required resolution such that S_H orientations, which deviate from the regional trend, cannot be explained (Bell, 1996; Mariucci et al., 2002). The first objective of this research is therefore to expand the Dutch Stress Map (DSM) database in which S_H orientations are collected. The main input for this database are borehole break-outs, drilling-induced fractures and acoustic anisotropy data, which can be inferred from various wireline logs. In such a way, this database will allow for a better understanding of the anomalous S_H orientations that can be observed in the Netherlands. Moreover, this research has the objective to characterize the stress regimes with depth in a borehole of the Groningen field, using different one-dimensional in-situ stress models. As such, the sensitivity of the in-situ stress regime to different boundary conditions can be studied.

First, the importance of the state of stress will be emphasized and it will be described which in-situ stress data is currently lacking in the WSM dataset of the Netherlands. Subsequently, information will be provided about how wellbore features can give an indication of the horizontal stress orientations in a vertical borehole and how these features can be identified on various wireline logs.

The datasets that are used to expand the DSM database will be described to illustrate how data mining and processing has been carried out. Thereafter, the resulting database will be used to conduct a detailed analysis of the S_H orientations on both a national and local scale.

After analysing the in-situ stress orientations, a closer look is taken at the magnitudes of these stresses by analysing the stress regimes in several one-dimensional models. Finally, this research also includes a workflow that describes the process of performing a basic 3D simulation in the JewelSuite Subsurface Modelling software and which can serve as basis for future studies.

2. The stress field in the Netherlands

A sound understanding of the in-situ stress state is an essential component in the development of geomechanical models (Zoback, 2010). Moreover, in this research it plays a crucial role in understanding variations in the direction of S_H , both on a regional and on a more local scale. In this section, the importance of understanding the state of stress will first be highlighted, after which a closer look is taken at the in-situ stress data which is currently lacking in the Dutch stress field.

2.1 Importance of the state of stress

Knowledge of the state of stress is of key essence in understanding geomechanical aspects that are related to hydrocarbon and geothermal reservoirs, and the overburden. In such a way, a better understanding can be obtained of e.g. fluid flow in fractured reservoirs and wellbore stability in structural complex areas, such as near salt domes. This is of crucial importance to ensure that subsurface resources are recovered in a safe and successful manner (Zoback, 2010; Kingdon et al., 2016).

For the Netherlands in particular, detailed knowledge of the stress field is vital in understanding and predicting seismicity related to production and injection in hydrocarbon fields. The production of oil and gas and the injection of, for example, carbon dioxide, leads to pressure changes in a reservoir, which in turn can induce processes such as fault reactivation (Zoback & Gorelick, 2012). In addition, the stress state plays an important role in characterizing the stress conditions at large depths (> 4000 m) for the development of ultra-deep geothermal energy projects (Rijksoverheid, 2017).

These examples clearly illustrate the importance of understanding the in-situ stress field, however, knowledge of the subsurface stresses has been lagging behind. The WSM has played a key role in improving this understanding by systematically collecting stress data in the hydrocarbon industry (Fuchs & Müller, 2001). As such, a database with the present-day stresses in the Earth's crust is compiled such that a better understanding can be obtained of the patterns and sources of these stresses (World Stress Map, 2017).

2.2 What is not known in the Dutch stress field?

Müller et al. (1992) note that in the WSM three characteristic regions can be identified in Europe in terms of S_H orientation: Western Europe, Northern Europe, and the Aegean Sea and western Anatolia. In Western Europe, a present-day NW-SE S_H orientation has been identified, however, only a single S_H direction has been given per well. This NW-SE maximum horizontal stress coincides with the direction of compressional ridge push at the Mid-Atlantic Ridge and the direction of the collision between the Eurasian and African tectonic plates (Klein & Barr, 1986). As a consequence, the NW-SE S_H orientation shows that the horizontal stresses in Western Europe are mainly affected by the forces that drive plate tectonics (Müller et al., 1992).

The NW-SE orientation indicated by the WSM for Western Europe has been confirmed by e.g. Van Eijs and Dalfsen (2004) who performed a study specifically for the Netherlands. In the on- and offshore areas, they identified a dominant NW-SE S_H direction without specifying the depth of the data points. This regional

NW-SE S_H trend is displayed in Figure 1, which illustrates the stress data of the WSM for the Dutch on- and offshore areas. However, the extent of this NW-SE S_H direction with depth has not yet been studied as the map only shows one or two S_H orientations per well. As a result, the WSM cannot indicate whether the horizontal stress directions vary with depth. In addition, it does not provide any information about the stress magnitudes in a well, such that it remains unknown whether the in-situ stress regime changes with depth. More details about the WSM project and the data displayed in Figure 1 will be given in Section 4.1.1.

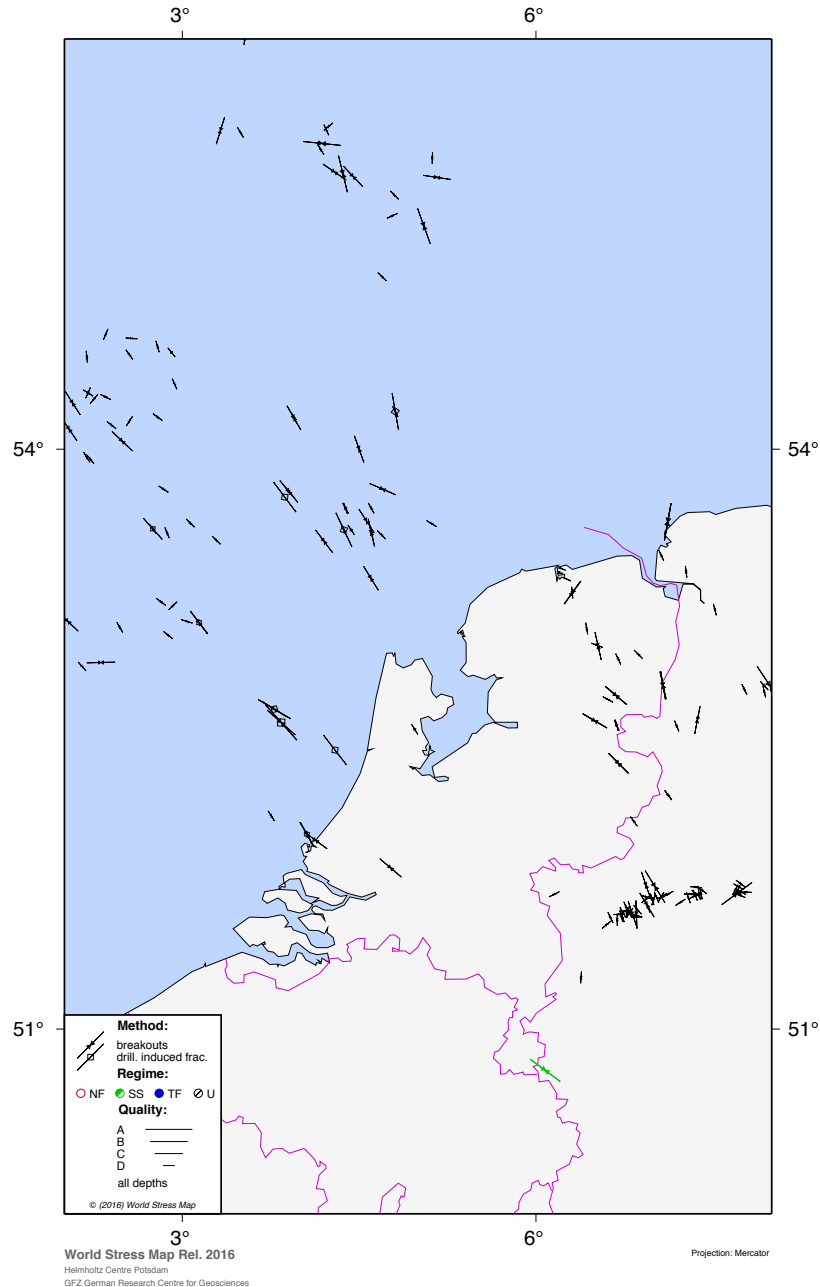


Figure 1: Directions of the maximum horizontal stress as displayed by the orientation of the symbols. All data points are either based on break-outs or drilling-induced fractures. The colour of each symbol represents the stress regime at a specific depth, whereas the length of the symbol indicates the data quality as defined by the WSM (Heidbach et al., 2016b).

3. Identification of stress-induced borehole features

Stress-induced borehole features are an important source for the determination of horizontal stress directions, especially in the upper five km of the Earth's crust (Heidbach et al., 2016a). Therefore, the theory of stress concentration around a vertical well will first be briefly presented, such that it can be understood how compressive and tensile borehole failure characterize the direction of S_H . Subsequently, this theory will be used in combination with the technology of various wireline tools to identify these two types of borehole failure on logs.

3.1 Compressive and tensile borehole failure

The excavation of rock material inside boreholes causes stresses to concentrate around the wellbore, as the rock cannot longer support the far-field stresses (Zoback, 2010). The in-situ stress field surrounding wells has been extensively described by e.g. Kirsch (1898) for isotropic and elastic media. In a vertical well that aligns with the axis of a principal stress, a high compressive stress is experienced at the azimuth of the minimum horizontal stress (S_h), whereas a low compressive stress or even a tensile stress is experienced in the direction of S_H (Zoback, 2010). These stress concentrations around vertical wells will result in two types of stress-induced borehole failure: break-outs and drilling-induced fractures (Brudy & Kjørholt, 2001). Compressive borehole failure will lead to the formation of break-outs at the azimuth of S_h when the stress exceeds the internal rock strength (Bell & Gough, 1979; Zoback et al., 1985). On the other hand, tensile stresses at the azimuth of S_H can result in drilling-induced fractures as rocks are characterized by a low tensile strength (Zoback, 2010). In contrast to natural fractures, drilling-induced fractures are oriented (sub)-parallel to the axis of the wellbore. These fractures do not result in the same amount of wellbore enlargement as break-outs, as the increase in hoop stress with radial distance prevents the fractures to propagate more than a cm into the formation (Heidbach et al., 2016a; Zoback, 2010; Zoback et al., 2003).

Break-outs and drilling-induced fractures are the two main stress indicators used in this research to determine the orientation of the minimum and maximum horizontal stress. However, the relations described above, solely apply to (sub)-vertical wells because in deviated wells, with deviation angles of more than 10° , the vertical stress is no longer (sub)-parallel to the wellbore axis. As a consequence, the straightforward relation between the orientation of the principal stresses and the location of compressive and tensile borehole failure is no longer valid (Zoback et al., 2003). In deviated wells, the horizontal stress directions can be determined with an analytical elastic solution derived by Fairhurst (1968). This analytical equation enables one to determine the horizontal stress directions in wells that are drilled at any orientation with respect to the three principal stresses.

3.2 Image logging tools

Image logging tools have the ability to generate images of the borehole wall by utilizing the measured contrasts in physical properties (Heidbach et al., 2016a). However, they are not standard tools in the industry due to the slow logging speed required and thus high costs (Brudy & Kjørholt, 2001). In this

section, electrical and acoustic imaging tools will be briefly described as they are frequently used for the identification of stress-induced borehole features (Prensky, 1999).

3.2.1 Electrical imaging tools

First of all, electrical imaging tools are mainly run in water-based muds in which the pads are pressed against the borehole wall to measure the strength of the electric current (Van Eijs & Dalftsen, 2004). A major benefit is that these tools have a resolution in millimetres, which implies that they have the ability to characterize even very small stress-induced features. However, when full contact between the tool pads and the borehole wall cannot be established or the borehole wall is too rough, it can result in a degradation of the data quality (Brudy & Zoback, 1998). Electrical image logging tools that are frequently used in this research, are the Formation MicroScanner (FMS), Formation MicroImager (FMI), Oil-Based MicroImager (OBMI), Simultaneous Acoustic and Resistivity tool (STAR) and Earth Imager (EI).

With the use of electrical image logging tools, break-outs will be displayed as broad features of high conductivity, which are often poorly resolved as the pads cannot make full contact with the borehole wall in zones of wellbore enlargement. As a consequence, the tool will measure the resistivity of the borehole fluid rather than the properties of the formation (Heidbach et al., 2016a). In Figure 2 an example is shown of a resistivity image from the E18-A field in the Dutch offshore sector, in which the break-outs are highlighted as white patches on both sides of the wellbore.

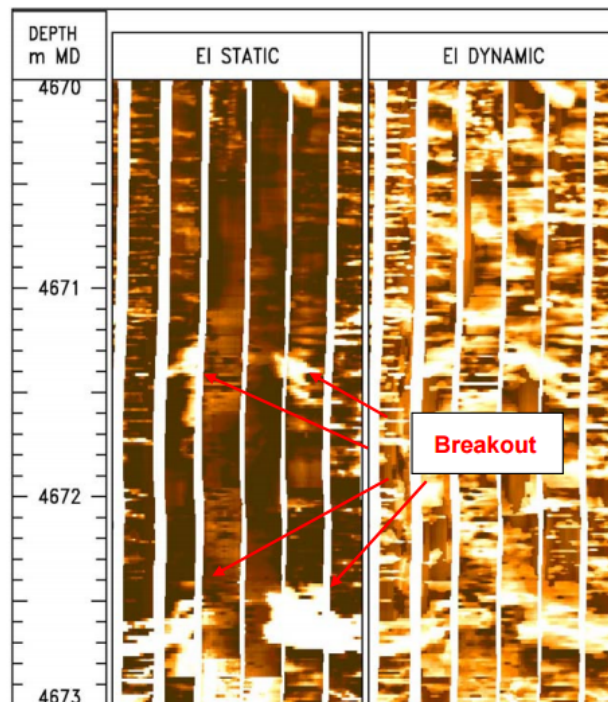


Figure 2: Example of break-outs on an electrical image log in the E18-A field (source: Appendix H).

In the case of drilling-induced fractures, water-based mud will infiltrate into these fractures, which results on the image log in a pair of highly conductive features, separated 180 degrees from each other (Heidbach

et al., 2016a). Although it has been mentioned that drilling-induced fractures form parallel to the axis of a vertical well, they are often not completely straight on image logs but instead consist of minor kinks (Brudy & Zoback, 1998). A clear example is displayed in Figure 3, where a number of drilling-induced fractures have been interpreted by Heidbach et al. (2016a) on FMI logs. Important to note is that when an electrical imager is used in an oil-based mud (e.g. OBMI tool), borehole break-outs and drilling-induced fractures will be shown as resistive and no longer as conductive features on the image logs (Heidbach et al., 2016a).

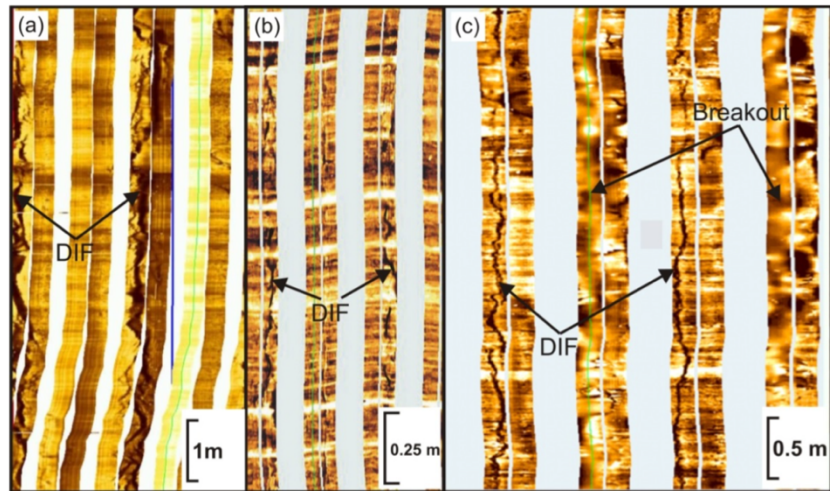


Figure 3: Example of drilling-induced fractures on the logs of a FMI tool (Heidbach et al., 2016a).

3.2.2 Acoustic imaging tools

The second category of imaging tools are the acoustic imagers with which stress-induced features are interpreted by generating borehole radius and reflection amplitude images. The acoustic tools that belong to this category and which are predominantly used in this research, are the Ultrasonic Borehole Imager (UBI), Circumferential Borehole Imaging Log (CBIL) and STAR. The latter collects simultaneously resistivity and acoustic data in the borehole and therefore is both an electrical and acoustic imaging tool (Heidbach et al., 2016a).

By running acoustic imaging logs, break-outs can be interpreted using both the borehole radius and reflection amplitude images. On radius images, break-outs are well exhibited as they often result in a clear increase of the borehole radius. In case of amplitude images, break-outs manifest themselves as features with low reflection amplitudes as they are characterized by a high degree of surface roughness and variability (Heidbach et al., 2016a). In Figure 4 such a reflection amplitude image is shown for the E17-FA field in the Dutch offshore sector. Four distinct pairs of break-outs have been identified, which are highlighted by the blue boxes.

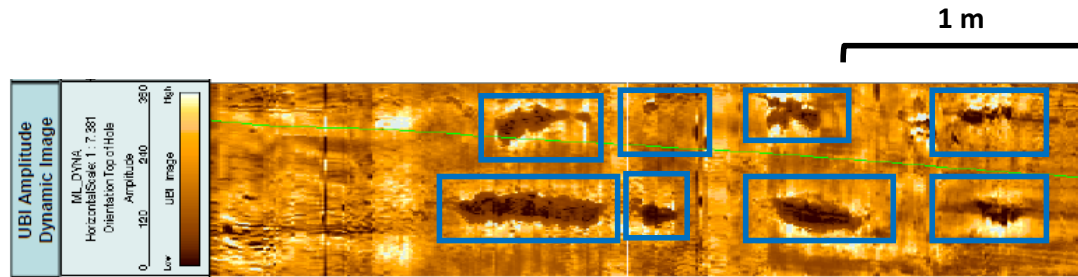


Figure 4: Section of an acoustic image log (UBI) in the Dutch E17-FA field. The four pairs of break-outs are highlighted by the blue boxes (source: Appendix H).

In contrast to break-outs, drilling-induced fractures are not observable on borehole radius images as these stress-induced features do not result in a considerable enlargement of the wellbore. Therefore, they are mainly observed on reflection amplitude images in which they are seen as narrow and low reflectivity zones due to their inability to reflect all the acoustic energy (Heidbach et al., 2016a).

Besides the above-mentioned differences between electrical and acoustic image logs, it must also be highlighted that acoustic tools have a reduced vertical resolution compared to electrical tools. However, acoustic tools are more sensible to the state of the borehole wall and are able to make a 360° image of the wall. This is in contrast to the electrical imagers which usually cover less than 75% of the borehole wall (Kingdon et al., 2016).

3.3 Four-arm caliper tools

In comparison to the image logging tools, four-arm calipers have been more commonly used in the past to trace stress-induced borehole features. Examples of four-arm caliper tools are the High Resolution Dipmeter (HDT), Stratigraphic High Resolution Dipmeter (SHDT) and Oil-Based Dipmeter (OBDT) (Heidbach et al., 2016a). These tools continuously rotate when pulled up, but cease rotation when a break-out is encountered. Simultaneously, one caliper pair will read a larger borehole diameter compared to the other pair and as such break-outs can be identified from caliper logs (Williams et al., 2015).

A major limitation of these caliper tools is that they can only characterize break-outs and not drilling-induced fractures. Drilling-induced fractures do not result in borehole enlargements and therefore they cannot be identified with four-arm caliper tools (Heidbach et al., 2016a). Another important difference with respect to borehole images, is that with four-arm caliper tools it is not straightforward to distinguish break-outs from other types of borehole enlargements, which are not stress field indicators (washouts and key seats). Also, Kingdon et al. (2016) mention that caliper tools lack the required resolution compared to image logs. The latter have a millimetre scale resolution, whereas caliper tools can only characterize clear break-outs that are formed over several metres in the borehole.

Finally, image logging tools are able to determine the azimuth of break-outs in the centre of the zone with a higher degree of accuracy compared to four-arm caliper tools. This is due to the fact that the shape and size of the break-out but also torsion of the tool can prevent perfect alignment of the caliper pair with the centre of the break-out zone (Van Eijs & Dalhsen, 2004).

As a result, when comparing the image and caliper log techniques, there are a number of clear reasons why image logging tools are more reliable to interpret stress-induced features and hence characterize the orientation of S_H (Zoback et al., 2003).

3.4 Sonic logging tools

The final and less frequently used method to characterize horizontal stress directions around a borehole, is with sonic logging tools. The sonic waves emitted by this tool type are influenced by formation characteristics which can vary with direction around the wellbore. As a consequence, sonic logging tools provide a technology that can identify stress-induced acoustic anisotropy and hence the direction of S_H without the use of compressive and tensile borehole features (Haldorsen et al., 2006).

In an anisotropic formation, flexural waves emitted by sonic logging tools will be split into two differently polarized waves: a fast and slow flexural wave. To be more precise, the fast flexural wave will be polarized in the direction of S_H when the formation anisotropy is stress-induced. Therefore, by performing such an acoustic analysis it is possible to define the horizontal stress directions when bedding is sub-horizontal and natural fracture networks do not affect the polarization process (Zoback, 2010). Important to note is that these polarized flexural waves can only be identified by tools which have a combination of dipole transmitters and receivers, as shown in Figure 5 (Haldorsen et al., 2006). Examples of these kinds of tools are the XMAC-F1 of Baker Hughes and the Sonic Scanner of Schlumberger.

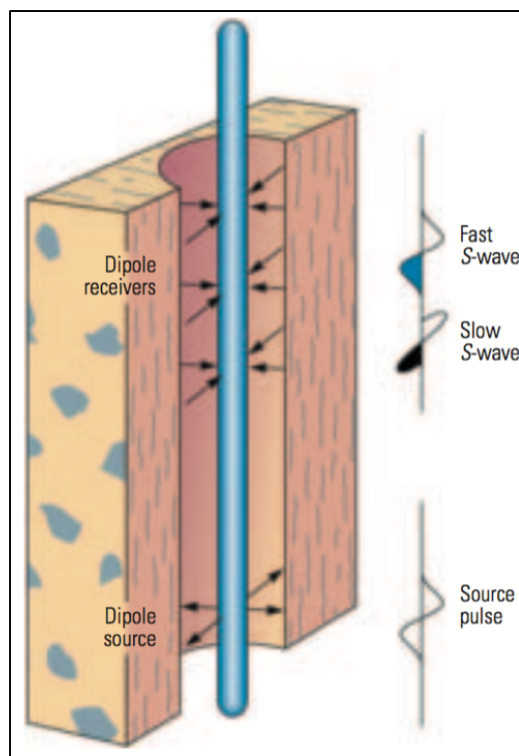


Figure 5: Sketch of the sonic logging tool set-up to determine stress-induced acoustic anisotropy in a formation (Haldorsen et al., 2006).

4. Datasets

The World Stress Map serves as an important reference in this research as it is the main source of regional present-day stress data in Western Europe and the Netherlands. In this research, data pertinent to the present-day stresses in the Dutch subsurface has been collected from four different sources: the WSM, The Netherlands Organisation for Applied Scientific Research (TNO), Rondel and Everaars (1993) and Van Eijs (2015). TNO provided a dataset of image and caliper log data for 852 wells, concerning the Dutch on- and offshore areas, whereas Rondel and Everaars (1993) collected horizontal stress directions in the north-eastern part of the Netherlands. In the recent study by Van Eijs (2015), present-day stress data has been collected in the Permian Slochteren Formation of the Groningen field. A quality ranking system is applied to the collected data to enable data comparison and to obtain an indication of its reliability.

4.1 Data collection

4.1.1 World Stress Map dataset

In the WSM, present-day horizontal stress directions are derived from four different categories of stress indicators: Earthquake focal mechanisms, wellbore break-outs and drilling-induced fractures, in-situ stress measurements and young geologic data. However, the dataset visualizes not only the direction of the maximum horizontal stress, but also the type of stress indicator, the tectonic regime and a quality ranking. Each stress indicator in a borehole is quality ranked according to a quality ranking system developed by the WSM. In Appendix A, a closer look is taken at this quality ranking system as well as at the different stress indicators that serve as a basis for this dataset.

Throughout the Dutch on- and offshore areas, the WSM dataset contains information for 115 unique wells. In the majority of these wells (109), the direction of S_H is based on break-outs and/or drilling-induced fractures, whereas in the remaining six wells the orientation is based on earthquake focal mechanisms. Data from these six wells has not been taken into consideration, as focal mechanisms derive the direction of S_H from significantly deeper depths (> 6 kilometres) and are influenced by seismic activity (Zoback, 2010). Of the 109 wells, only 45 wells indicate a S_H orientation, as they have been ranked as A- to D-quality data. The horizontal stress directions in these 45 wells have been used without further processing and an overview of this data is given in Appendix A. The remaining 64 wells are E-quality data, which implies that the data is not reliable enough (Heidbach et al., 2016a) and therefore the WSM has not stated the S_H orientations.

4.1.2 TNO dataset

In contrast to the WSM dataset, data in the TNO dataset requires processing to derive S_H orientations from reports and image logs given for each well. More details about the workflow for processing this dataset can be found in Appendix B. Data processing reduced the analysis of horizontal stress directions to 84 wells as for the remaining 768 wells no stress data reports or high quality image logs have been found. For these remaining wells, the interpretation of four-arm caliper and low quality image logs would have been very time consuming and requires specialized software for a successful analysis.

Of the 84 unique wells, 56 wells actually contain useful horizontal stress direction data. In the remaining 28 wells, no break-outs or drilling-induced fractures have been identified and no acoustic analysis has been performed according to the reports and image logs. Twenty of the 56 wells have deviation angles of more than ten degrees, implying that break-outs and/or drilling-induced fractures will no longer give a correct representation of the S_H direction around the borehole (Heidbach et al., 2016a). All stress records per well, in combination with the tool type and stratigraphy, are shown in Appendix C.

4.1.3 Rondel and Everaars dataset

In the research performed by Rondel and Everaars (1993), 42 boreholes of the Nederlandse Aardolie Maatschappij (NAM) have been analysed in the northeast of the Netherlands. With the use of four-arm caliper tools (HDT and SHDT), S_H directions have been determined in 23 (sub)-vertical and deviated wells, which means that no further data processing has been required. The remaining 19 wells have not encountered stress-induced borehole features or the S_H orientation is based on the deviation azimuth of the well. The latter type of data has been excluded as this research solely focusses on stress-induced borehole features or acoustic anisotropy. In Tables 24 and 25 (Appendix C), a detailed overview is given of this third dataset.

4.1.4 Van Eijs dataset

The fourth dataset is based on the research of Van Eijs (2015) who conducted a study on the present-day stresses in the Permian Slochteren Formation of the Groningen field. On the basis of break-outs, drilling-induced fractures and acoustic anisotropy, S_H orientations have been determined in seven boreholes such that no additional processing has been required. In Appendix C, the dataset shows for each well the tool type used, the depth of the stress measurement, the corresponding stratigraphy and the direction of S_H .

4.2 Comparison of datasets

In Table 1 an overview is given per dataset of the number of wells in which S_H directions have been determined. In terms of (sub)-vertical and deviated boreholes, horizontal stress data has been found in 86 new wells, resulting in a DSM database with 131 wells. Figure 6 shows that 44 of these 86 wells (51%) are (sub)-vertical, whereas 25 wells (29%) have deviation angles of more than ten degrees. For a number of wells (20%) the deviation angle cannot be determined due to confidentiality or the lack of data.

Table 1: An overview of the number of wells with S_H directions per dataset. A distinction is made between all wells (including deviated wells) and only (sub)-vertical wells.

Source	All boreholes	(Sub)-vertical boreholes
TNO	56	36
Rondel & Everaars	23	18
Van Eijs	7	7
<i>Subtotal</i>	86	61
WSM	45	45
<i>Total</i>	131	106

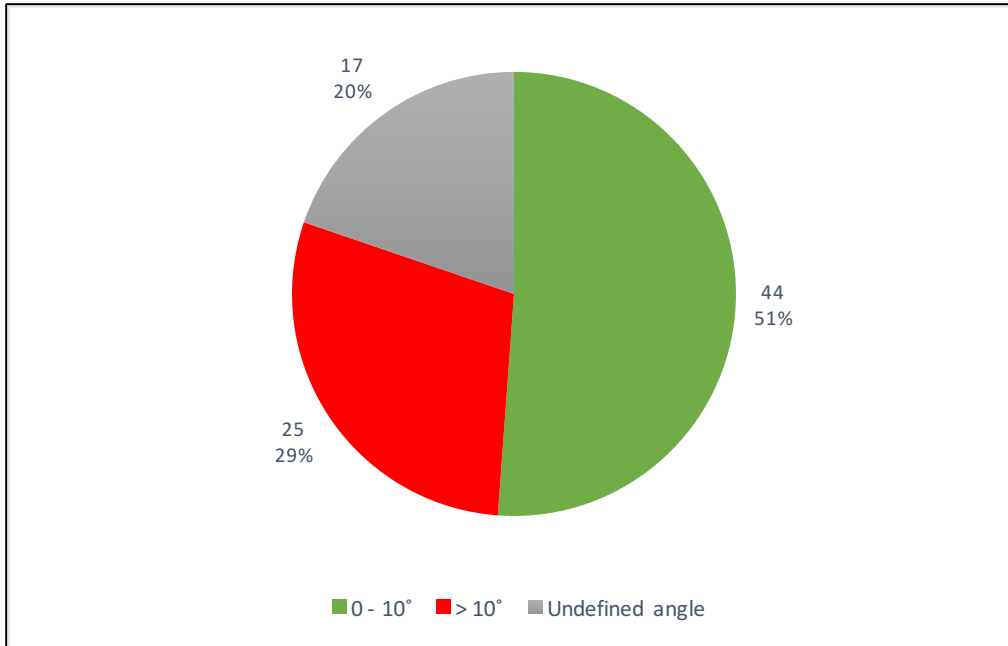


Figure 6: Horizontal stress data has been found in 86 new boreholes. More than 50% of these wells are drilled (sub)-vertical ($< 10^\circ$), 29% are deviated wells, whereas for 20% of the wells the deviation angle could not be determined.

The significant increase in the number of wells (+86) with horizontal stress data has a clear impact on the data coverage in the Netherlands. Figure 7a and b show that in the Dutch offshore, the collection of data has mainly resulted in new boreholes between 59° and 60°N . This region (blocks E, F, K and L) consists of dozens of producing gas fields, explaining the cluster of well data already shown in the WSM dataset. On the other hand, in the relatively less active regions south of 59°N and north of 60°N , the collection of new stress data has led to a marginal increase in new wells. In these two regions, Figure 7b depicts that only four new wells have been added north of 60°N , whereas stress data for nine new wells has been identified south of 59°N . For the Dutch onshore, a considerable increase in well data is depicted in the Groningen and Drenthe province, but also in Northern Overijssel. Similar to the Dutch offshore, these provinces are already characterized for decades by intense hydrocarbon production, showing that the data density in the Netherlands is clearly dependent on the extent of hydrocarbon production activities.

The addition of 86 new boreholes also affects the data distribution with depth as the WSM only indicates one or two S_H orientations per well. This is clearly seen in Figure 8, which displays the number of horizontal stress directions per stratigraphy for both the WSM dataset and the DSM database. In all stratigraphic groups, the DSM database shows an increase in the number of data points, especially in the Rotliegend and Limburg Group. The majority of the data (67%) in the DSM database is located in the pre-salt stratigraphies (Limburg Group and Rotliegend), whereas only 22% of the data is found in post-salt stratigraphies (Upper and Lower Germanic Trias Groups, Schieland Group, Scruff Group, Rijnland Group and Chalk Group). The Chalk Group has been the shallowest formation in which S_H orientations have been found. For a small number of data points (3%), the stratigraphy could not be defined due to the lack of a composite log or confidentiality reasons.

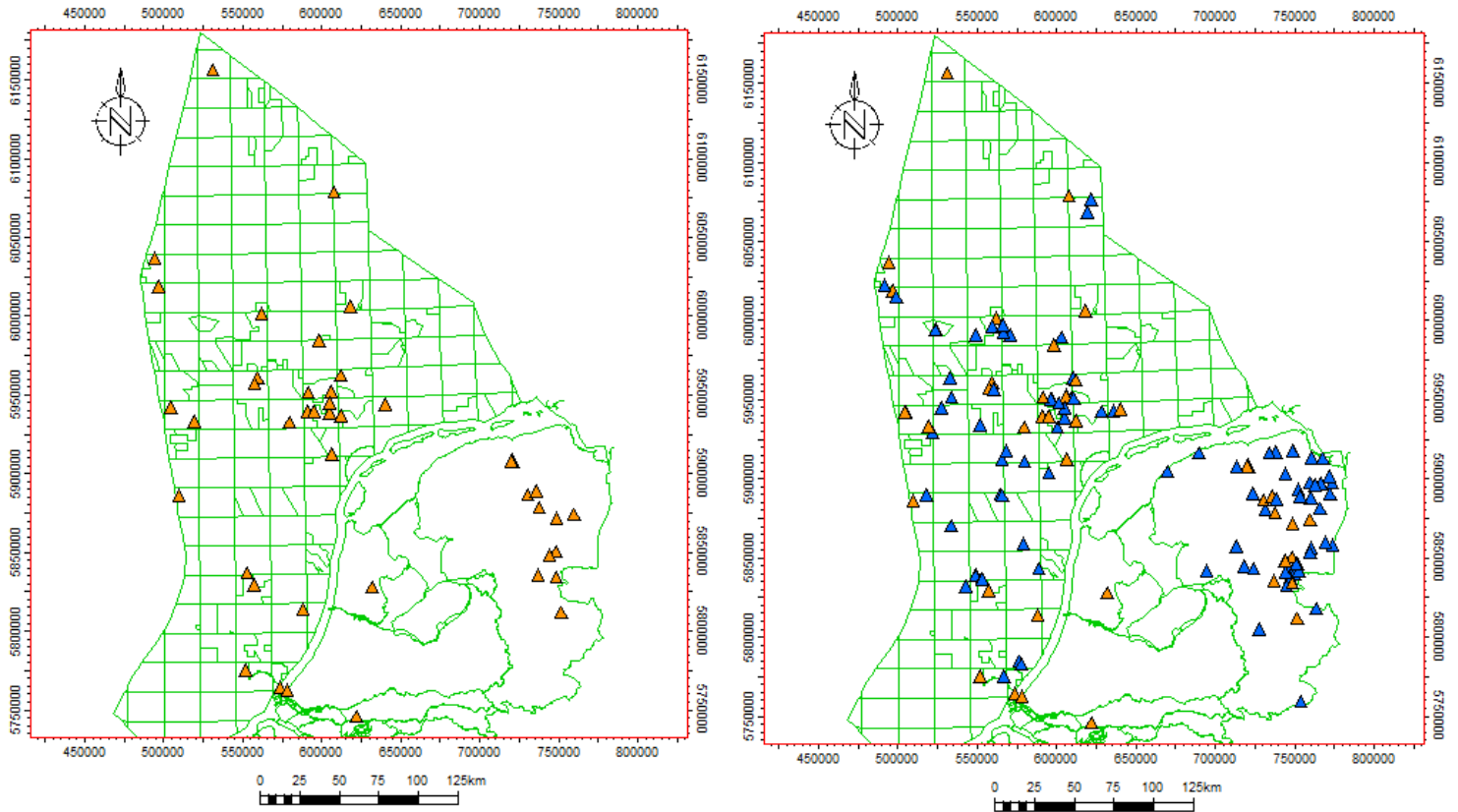


Figure 7: (a) Map of the Dutch on- and offshore areas indicating the 45 boreholes of the WSM dataset. (b) Map showing the WSM dataset and the 86 boreholes that have been added to the DSM database. The blue-filled triangles indicate the 86 new boreholes.

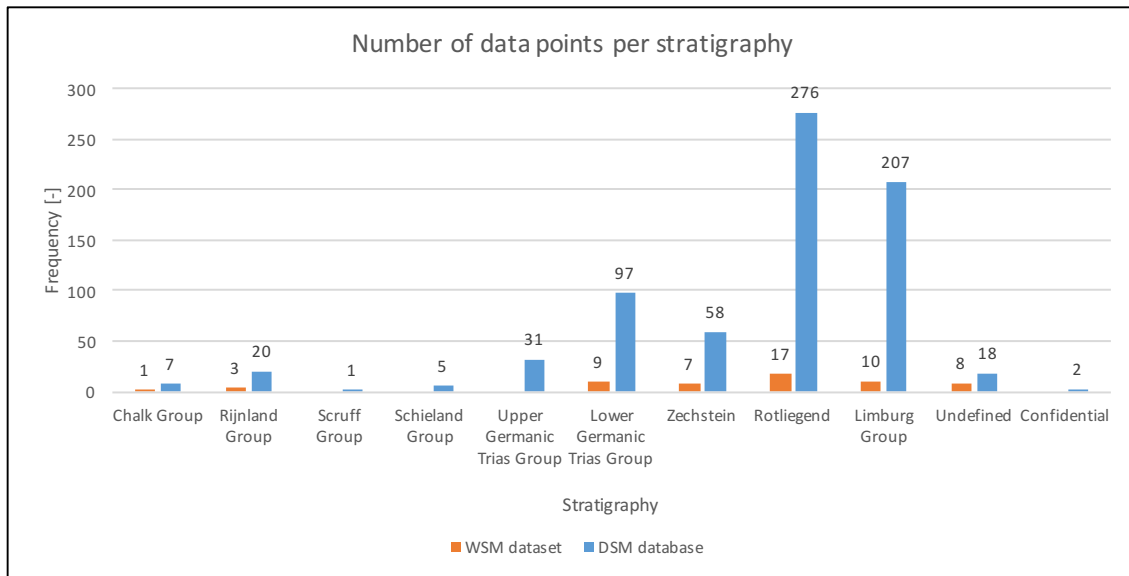


Figure 8: Frequency distribution indicating the number of stress data points per stratigraphic group for the WSM dataset and the DSM database.

4.3 Quality ranking system

A quality ranking system has been developed for the data derived from the TNO, Rondel and Everaars (1993) and Van Eijs (2015) datasets (Table 2). The quality label depends only on the combined number of break-outs and drilling-induced fractures (DIF's) observed in a borehole. As such, the system is less restrictive than those of the WSM where the quality ranking depends on the quantity of break-outs or drilling-induced fractures in each well, the total length of these features and the standard deviation (Sperner et al., 2003). Important to note is that Table 2 only applies to (sub)-vertical wells, as all deviated wells ($> 10^\circ$) have been excluded. A more detailed explanation of the quality ranking system in Table 2 is given in Appendix D.

Table 2: Quality ranking system for break-outs and drilling-induced fractures in a well. For the B- to D-quality labels, multiple conditions are stated but a well needs to satisfy only one of these conditions.

A - Quality	B-Quality	C-Quality	D-Quality	E-Quality
More than 10 break-outs and more than 10 DIF's	More than 10 break-outs and less than 10 DIF's	More than 10 break-outs and no DIF's	Less than 10 break-outs and no DIF's	No break-outs and DIF's
	Less than 10 break-outs and more than 10 DIF's	No break-outs and more than 10 DIF's	No break-outs and less than 10 DIF's	
	Less than 10 break-outs and less than 10 DIF's			

By applying this less restrictive ranking system, Figure 9 shows that the TNO data is spread over all five quality labels. In contrast, all boreholes would receive an E-quality label when the WSM quality criteria would have been applied. Although the system displayed in Table 2 might reduce the overall quality of the dataset, the additional information that has been obtained from a larger dataset outweighs the possible reduction in data quality (Rondel & Everaars, 1993). Moreover, the WSM quality ranking system is specifically made for visualizing regional stress data and is too strict for data of higher order resolution (Williams et al., 2015).

In contrast to the TNO dataset, all boreholes from Rondel and Everaars (1993) have been ranked with a D-quality label as in none of the wells more than ten individual break-out zones have been observed. Due to the limited amount of data per well in the research of Van Eijs (2015), most wells are labelled as D- or E-quality, except for ZRP-03-S1. A B-quality label has been assigned to this well as both break-outs and drilling-induced fractures are observed.

In map view, Figure 10 shows that onshore, the majority of the wells have been ranked as D-quality. On the other hand, in the Dutch offshore, the quality distribution is clearly more scattered, as not only D- and E-quality wells can be found but also a small number of wells with A- and B-quality labels.

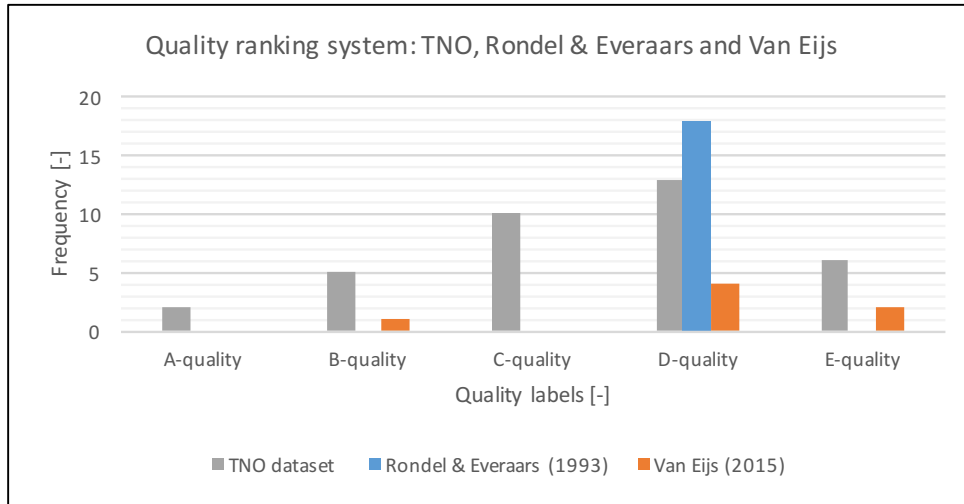


Figure 9: Quality distribution of the (sub)-vertical wells in the TNO, Rondel and Everaars (1993) and Van Eijs (2015) datasets. A-quality wells have the highest quality of stress data, whereas E-quality wells need to be treated with more caution (Heidbach et al., 2016a).

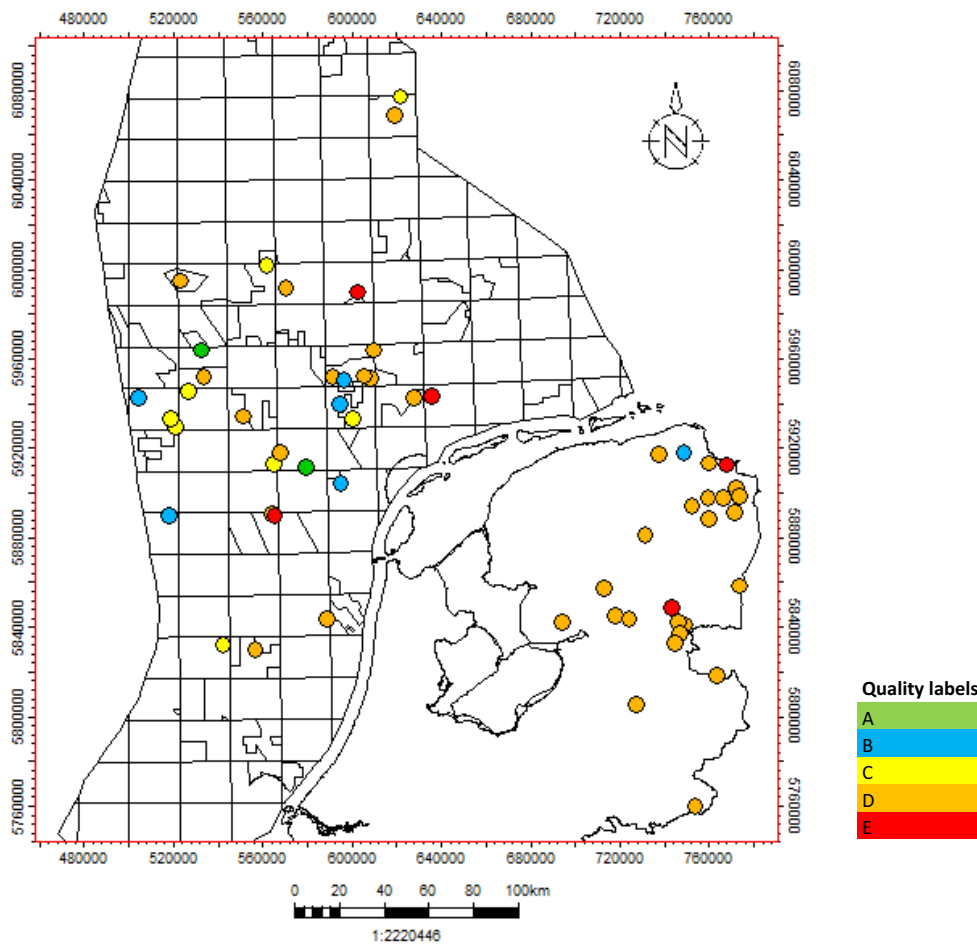


Figure 10: Map indicating the quality labels of the 61 (sub)-vertical wells found in the datasets of TNO, Rondel and Everaars (1993) and Van Eijs (2015).

5. Dutch Stress Map analysis

In this section, all horizontal stress data in the (sub)-vertical boreholes of the DSM database will first be examined. Subsequently, a closer look is taken at the S_H orientations in these (sub)-vertical wells per formation and by comparing the data in the pre- and post-salt stratigraphies. Finally, the horizontal stress directions in the deviated boreholes of the DSM database will be analysed.

5.1 Overall horizontal stress orientations

On the basis of the 106 (sub)-vertical boreholes in the DSM database, Figure 11 shows that a dominant NW-SE S_H trend can be observed when displaying all data points in a rose diagram. The database has a mean S_H direction of 323.4° , which is in close agreement with the regional NW-SE S_H direction observed in Western Europe. Moreover, the degree of variation in the S_H orientations is relatively limited as indicated by a circular standard deviation of 21.7° .

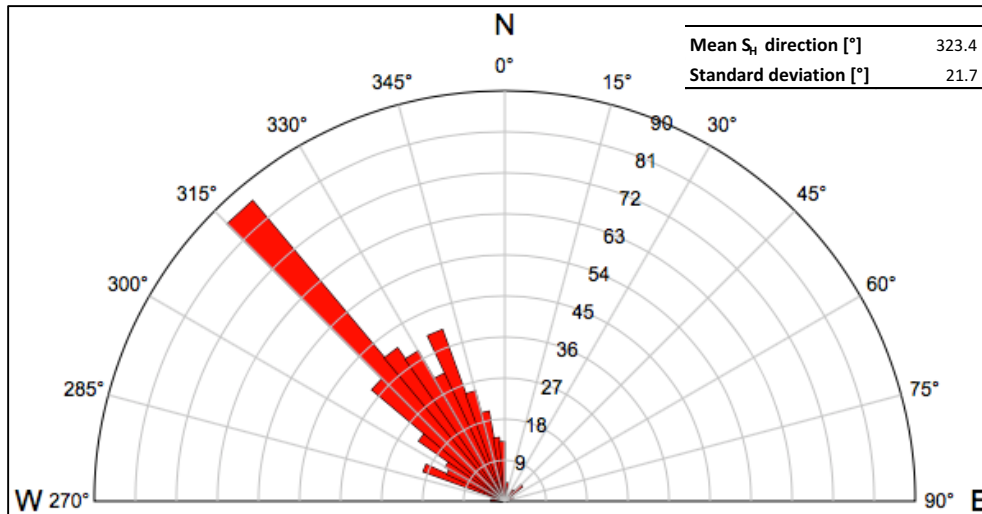


Figure 11: Half rose diagram of the S_H directions based on all stress data in the DSM database.

In map view, Figure 12 shows the resulting Dutch Stress Map in which the strike symbol indicates for each well the average S_H orientation per stratigraphic group. More detailed stress maps per stratigraphy can be found in Appendix E. Clearly, in all maps (Figure 12 and Appendix E) it is seen that the vast majority of the S_H directions support the present-day NW-SE trend. Nevertheless, a number of wells display E-W, N-S or NE-SW S_H orientations, which deviate significantly from the general NW-SE direction. These anomalies can be found both onshore (Groningen province) and offshore, and are not restricted to a specific stratigraphy as they are present in almost all stratigraphic groups. To obtain a better understanding of these anomalies, two wells with horizontal stress directions that deviate from the regional NW-SE S_H trend will be analysed in Section 6.

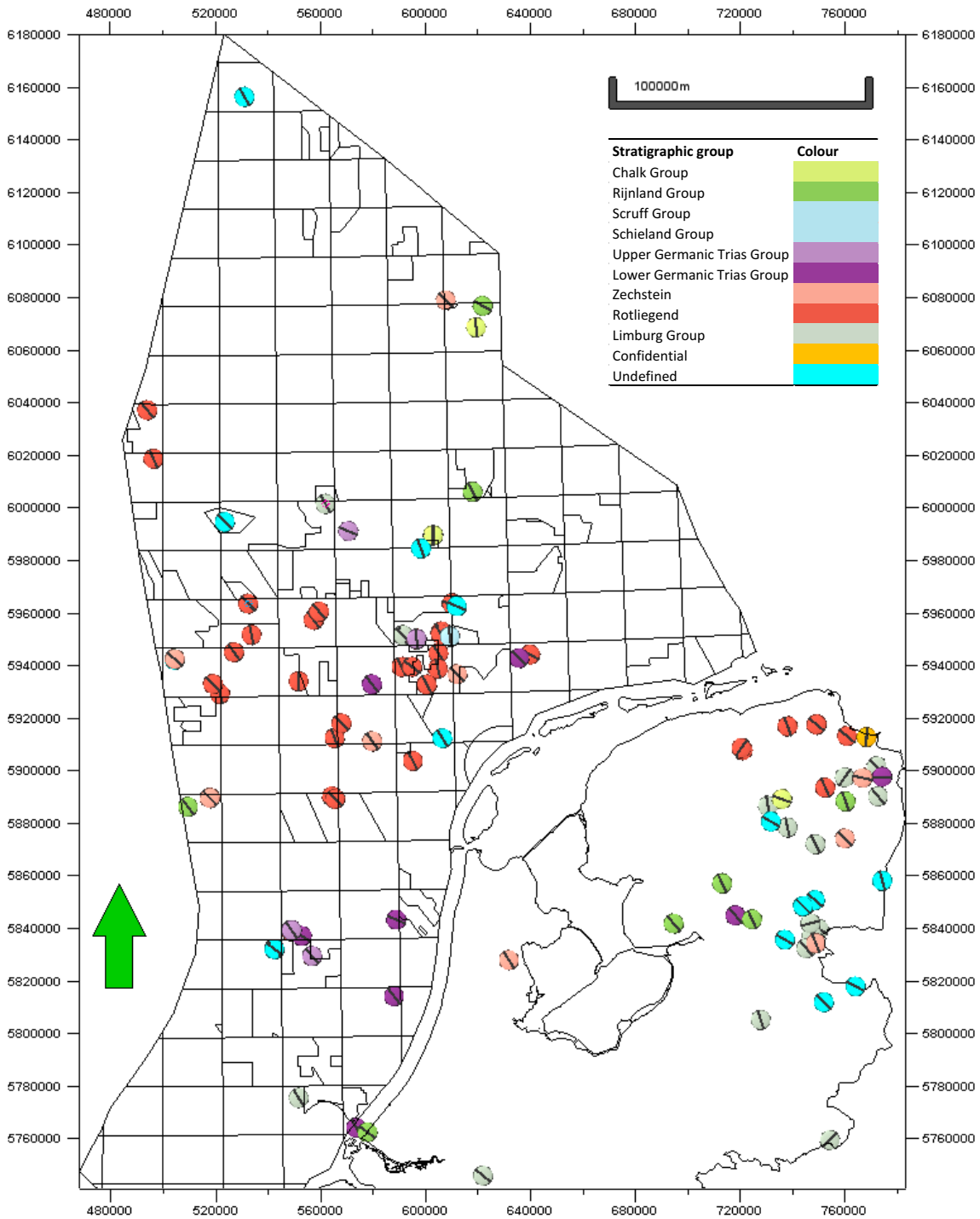


Figure 12: The Dutch Stress Map in which the symbols indicate the orientation of S_H . For each well, this map shows the average S_H direction per stratigraphy. If stress-induced features have been found in multiple formations, this map only shows the S_H orientation in the shallowest formation.

5.2 Formation specific stress analysis

The present-day NW-SE S_H trend is not only dominant spatially but also with depth as shown in the rose diagrams of the different stratigraphic groups (Figures 13 and 14). In general, most stratigraphies display a S_H orientation in the range of $315^\circ \pm 22.5^\circ$, except for the Chalk and Scruff Group. Table 3 shows that in these two groups, the mean S_H orientation is 351.8° and 352.5° , which implies an almost N-S orientation of S_H . Besides that, the rose diagrams illustrate that the degree of S_H variation (standard deviation) can differ considerably per stratigraphy. This variability is pronounced in the Rijnland, Lower Germanic Trias and Rotliegend Groups where the circular standard deviations are 20.2° , 23.6° and 20.4° , respectively. However, Table 3 also indicates relatively high standard deviations in the other groups, which can be related to the anomalous stress directions, which have not been filtered out.

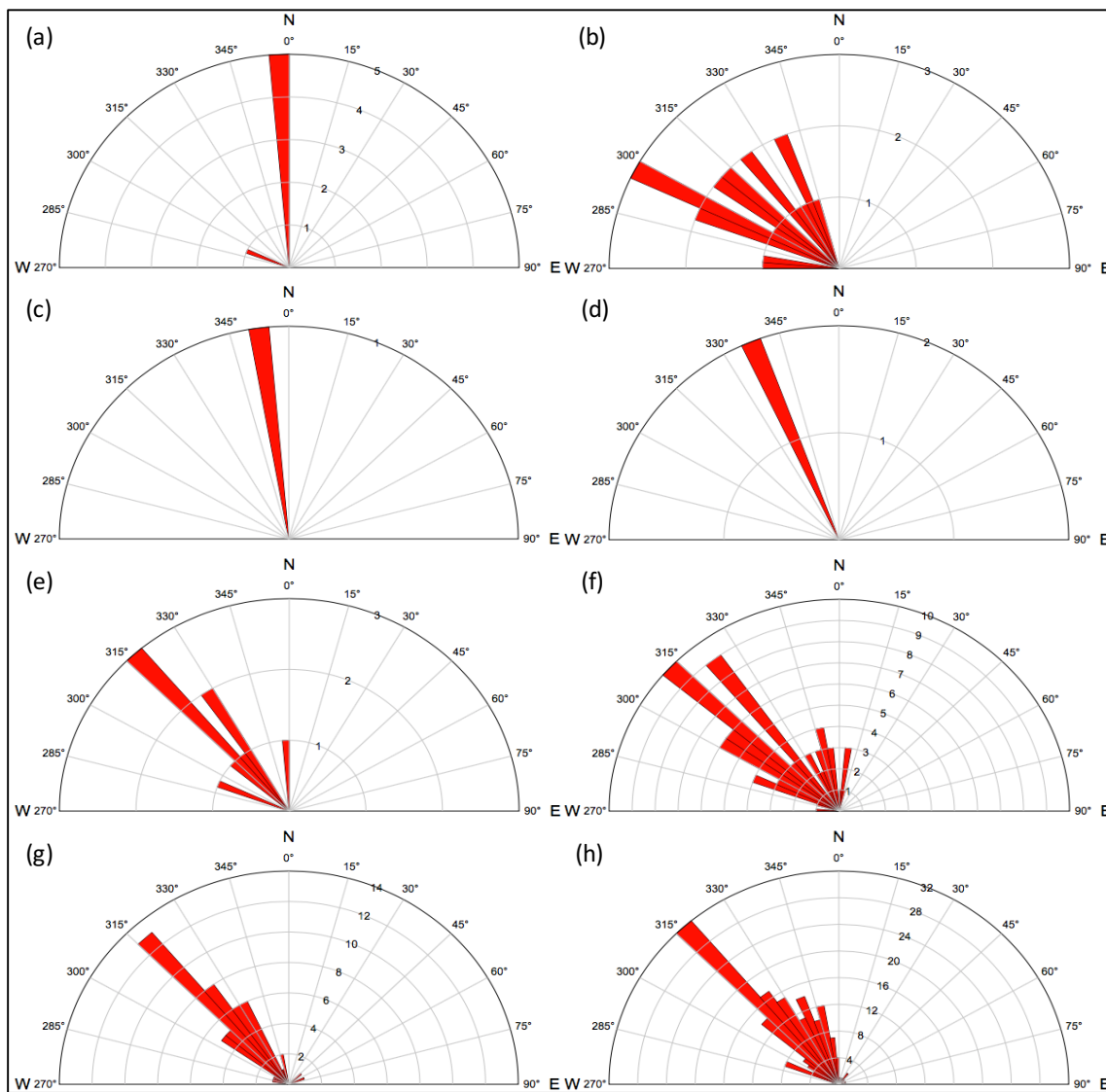


Figure 13: Half rose diagrams of the S_H directions based on stress data in the (a) Chalk Group, (b) Rijnland Group, (c) Scruff Group, (d) Schieland Group, (e) Upper Germanic Trias Group, (f) Lower Germanic Trias Group, (g) Zechstein and (h) Rotliegend.

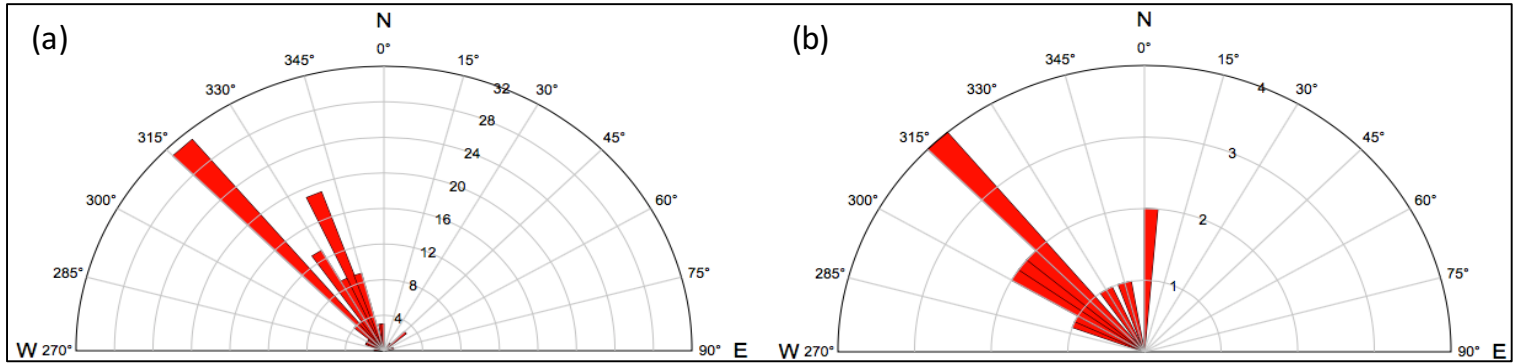


Figure 14: Half rose diagrams of the S_H directions based on stress data in the (a) Limburg Group and (b) undefined stratigraphies.

Table 3: Mean S_H direction and standard deviation per stratigraphy by applying circular statistics (Mardia, 1972).

Stratigraphic group	Mean S_H direction [°]	Standard deviation [°]
Chalk Group	351.8	20.8
Rijnland Group	308.1	20.2
Scruff Group	352.5	0.0
Schieland Group	336.3	1.3
Upper Germanic Trias Group	318.5	15.4
Lower Germanic Trias Group	319.3	23.6
Zechstein	318.2	17.0
Rotliegend	324.0	20.4
Limburg Group	325.5	19.9
Undefined	317.9	20.3

5.3 Pre- and post-salt stratigraphy stress analysis

In terms of the horizontal stress directions in the pre- and post-salt stratigraphic groups, Table 4 shows that the mean S_H orientation in the post-salt stratigraphies (319.7°) is slightly more oriented towards the NW-SE S_H trend compared to the mean S_H in the pre-salt stratigraphies (324.7°). However, it can be seen that the standard deviation of the post-salt data is larger compared to that of the pre-salt, implying that the S_H directions display a larger degree of variation in the post-salt stratigraphic groups.

Table 4: Mean S_H direction and standard deviation of the pre- and post-salt stratigraphies.

Data type	Mean S_H direction [°]	Standard deviation [°]
Pre-salt stratigraphy	324.7	20.6
Post-salt stratigraphy	319.7	24.2

This difference in the degree of spread is also depicted in Figure 15 where all data points in the pre-salt and post-salt stratigraphies have been collected in rose diagrams. The S_H data in the pre-salt stratigraphies (Figure 15a), shows indeed a narrower distribution compared to the post-salt dataset in which the S_H directions are clearly more scattered. Nevertheless, the latter dataset is distributed more symmetrical around 315° (NW) compared to the pre-salt data.

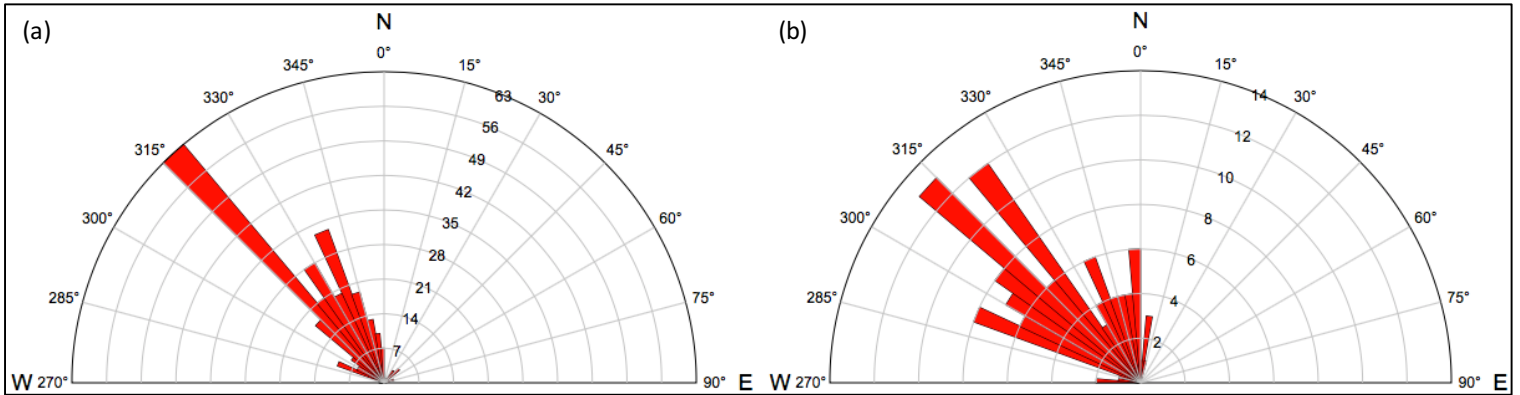


Figure 15: Half rose diagrams of the S_H directions based on stress data in (a) the pre-salt stratigraphies and (b) the post-salt stratigraphies. The pre-salt stratigraphy includes the Limburg Group and Rotliegend, whereas the post-salt stratigraphy includes the Lower and Upper Germanic Trias Groups, Schieland Group, Scruff Group, Rijnland Group and Chalk Group.

5.4 Deviated wells stress analysis

Figure 6 has shown that horizontal stress data in 25 out of the 86 new wells should not be used due to deviation angles of more than ten degrees. In these wells, there is no longer a straightforward relation between the orientation of the principal stresses and the location of stress-induced borehole features. However, Figure 16 illustrates that even the S_H orientations in these deviated wells roughly match the NW-SE S_H trend as the dataset has an average S_H direction of 324.1° with a standard deviation of 19.3° . The marginal number of S_H orientations that are observed between 30° and 75° all originate from the same well, suggesting that in this specific case the deviation angle has severely affected the orientation of the stress-induced borehole features.

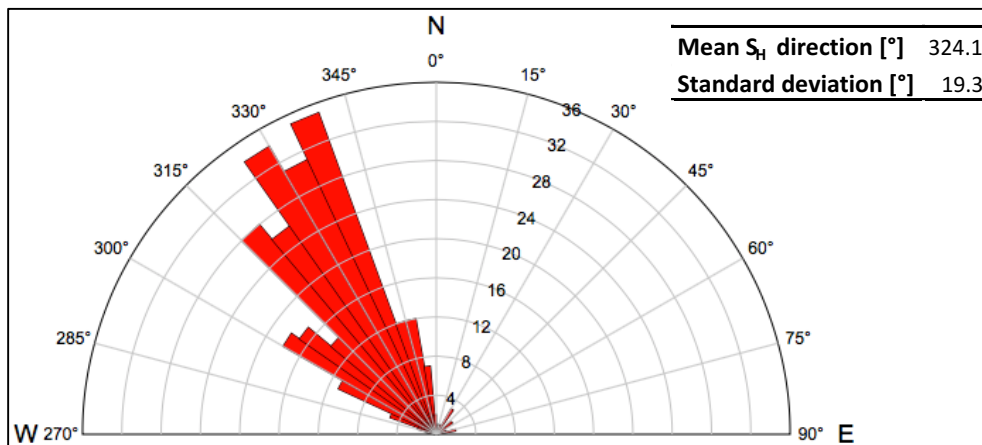


Figure 16: Half rose diagram of the S_H directions based on stress data in the deviated wells ($> 10^\circ$) of the DSM database.

6. Local stress deviations in the Dutch Stress Map

During the analysis of stress-induced borehole features, S_H directions are often only explained by the dominant tectonic boundary forces in a specific region (Aleksandrowski et al., 1992). However, numerous studies (e.g. Bell, 1996; King et al., 2012; Mariucci et al., 2002; Rajabi et al., 2017) have observed stress orientations that deviate significantly from the regional trend and which cannot be explained by these large-scale tectonic processes. Aleksandrowski et al. (1992) and Ask (1997) have shown that these S_H deviations can be related to the presence of local geological structures such as salt domes and faults.

To obtain a better understanding of the anomalies shown in the Dutch Stress Map and the potential relation with local geological structures, three case studies have been conducted. First, a base case scenario is discussed in which a well is analysed that has been drilled away from one of the above-mentioned structures. Subsequently, a well drilled through the centre of a salt structure will be studied to see whether the anomalous S_H orientations can be related to the presence of this local feature. In the third case, a similar analysis is performed on a well, which has been drilled next to a major normal fault and also displays S_H orientations that deflect away from the regional NW-SE trend.

6.1 Base case scenario

In offshore well K05-12, stress-induced borehole features have been identified on an UBI image log. The map of the area (Figure 17) shows that the Zechstein formation is of minimum thickness, indicating that K05-12 neither has been drilled through a salt structure nor is located in close vicinity of such a structure. The east-west crossline through K05-12 (Figure 18) confirms these observations, only a minor salt structure is observed in the west. In terms of faults, Figure 17 indicates that the major faults, which have been mapped in the area, do not intersect the borehole. This is confirmed by the composite log of K05-12 and the east-west crossline. Only two faults with small offsets have been identified on the eastern side of the well, however, these features are unlikely to have an influence on the stress field near the borehole.

The break-outs and drilling-induced fractures observed in this well, indicate a uniform NW-SE S_H direction, which does not vary between the different stratigraphic units (Figure 19). With a mean S_H direction of 315° and a very limited degree of variation in the orientation (circular standard deviation of 1.5°), it can be seen that the majority of the data perfectly aligns with the regional NW-SE trend observed in Western Europe.

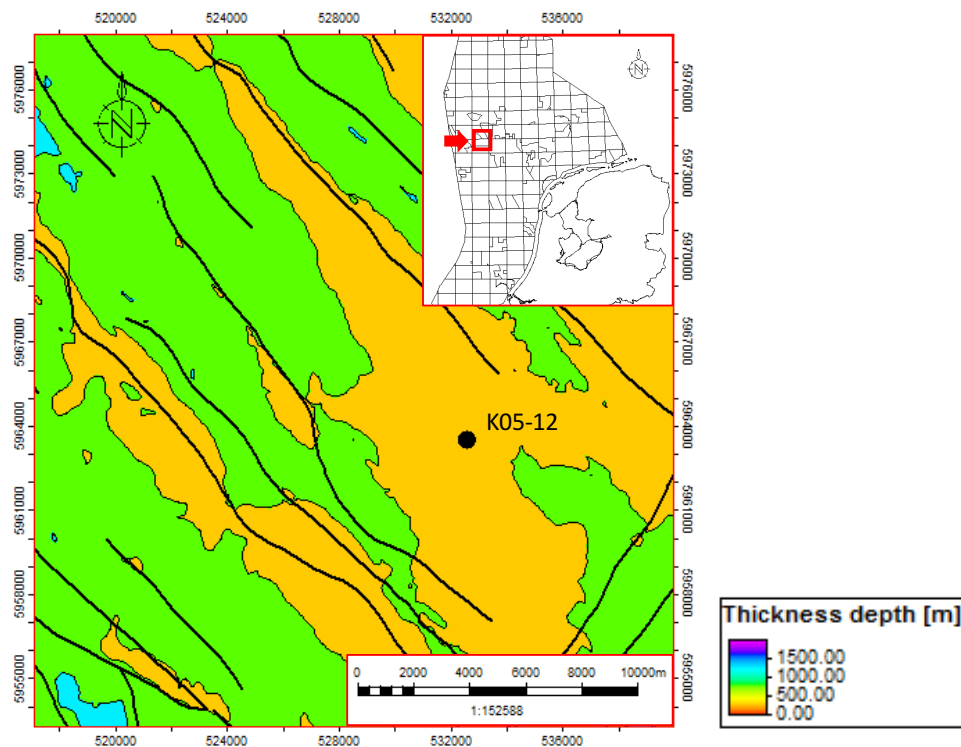


Figure 17: Zechstein thickness map including the major faults (in black) in the area of well K05-12. Faults have been mapped by NLOG (2015) and the location of the study area is displayed in the inset.

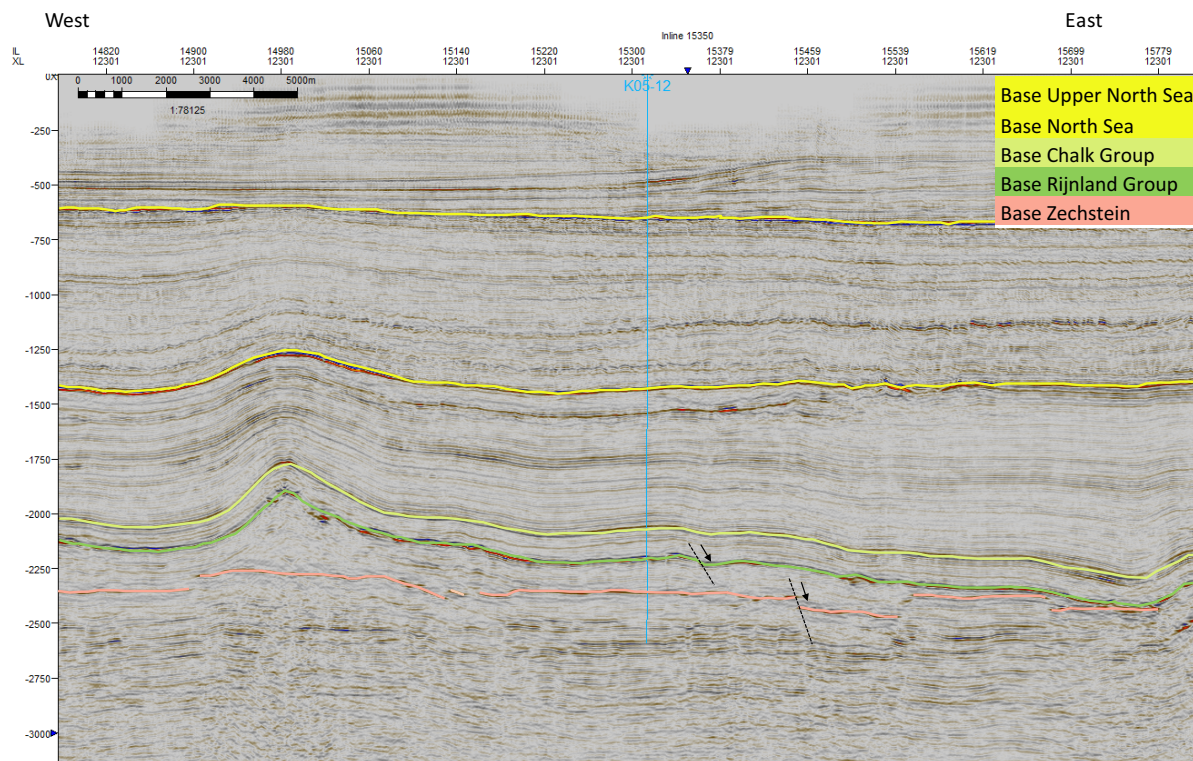


Figure 18: Cross line through well K05-12 in which the bases of the main stratigraphic groups are highlighted in two-way travel time. In the vicinity of the well, two normal faults and their displacement are indicated in black.

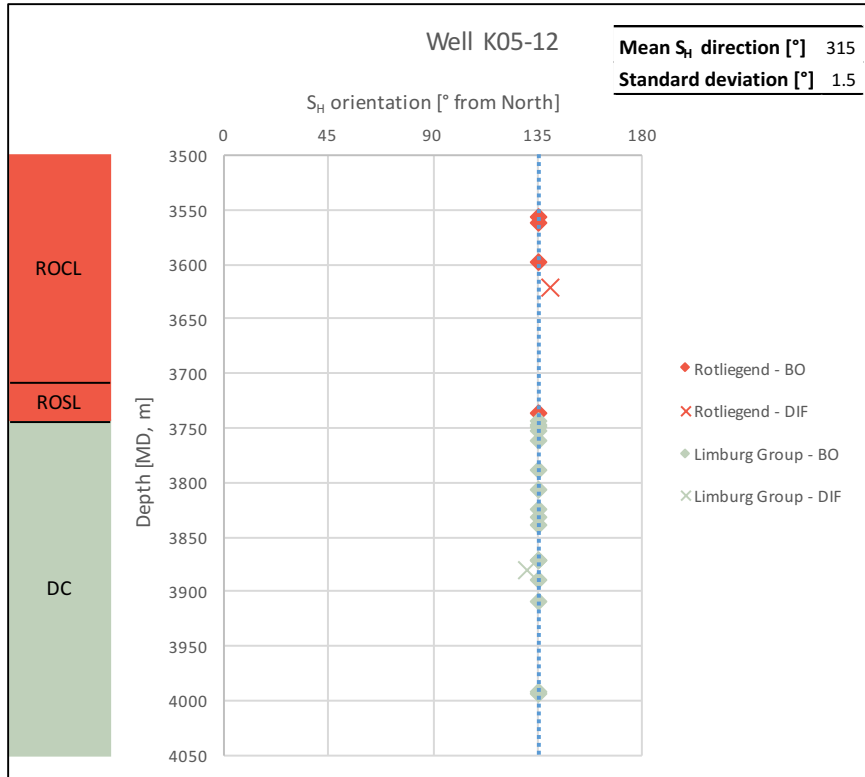


Figure 19: Distribution of break-outs and drilling-induced fractures with depth in well K05-12. Over an interval of 450 m, the variation in the horizontal stress directions is very limited. The blue dashed line indicates the regional NW-SE S_H trend. ROCL = Silverpit Formation; ROSL = Slochteren Formation; DC = Limburg Group.

The consistent S_H directions with depth are not in agreement with studies done by Ask (1997) and Cowgill et al. (1994) in the UK and Danish parts of the North Sea. Significant variations in the S_H orientation have been observed between different stratigraphic units, which is partly attributed to the influence of paleostress fields at the time of deposition (Cowgill et al., 1994). However, uniform S_H orientations with depth have been identified by Brudy & Kjørholt (2001) in several wells on the Norwegian continental shelf. This base case shows that in the Dutch North Sea, the NW-SE S_H trend is not only visible spatially but also with depth, suggesting that, for example, paleostress fields do not play a role when analysing wells away from geological discontinuities such as salt structures and faults.

6.2 Salt structures

Anomalous stress directions have been observed in offshore well X, in which the data has been derived from an acoustic anisotropy analysis. The map view in Figure 20 clearly shows that the well has been drilled through a massive salt structure, which might explain the S_H deviations from the regional NW-SE trend. At the crest of the salt structure, the map view and the east-west crossline (Figure 21) do not indicate any major faults that intersect the borehole and this is also confirmed by the composite log of X.

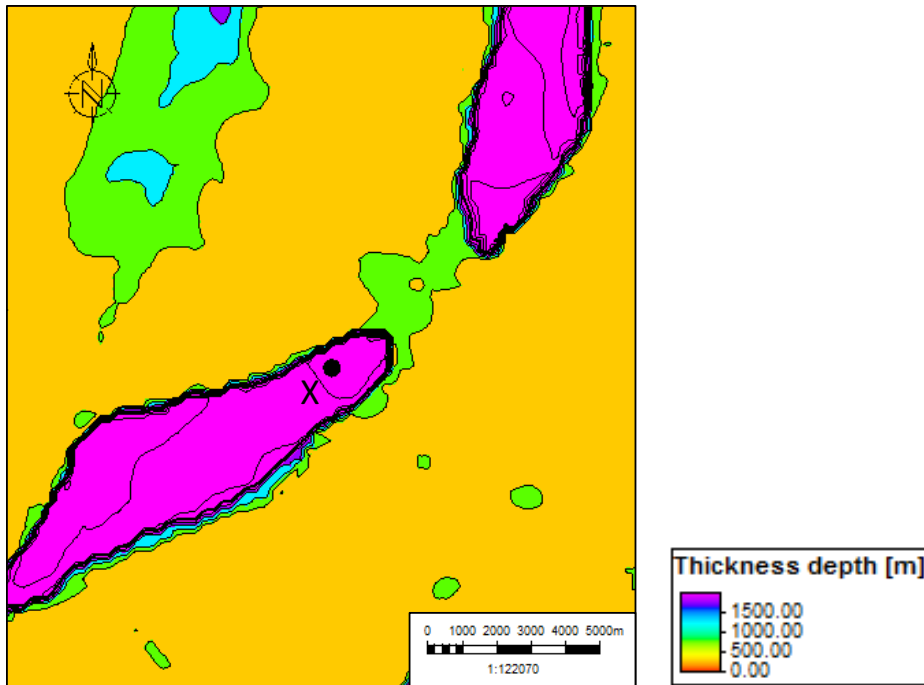


Figure 20: Zechstein thickness map of the area surrounding well X.

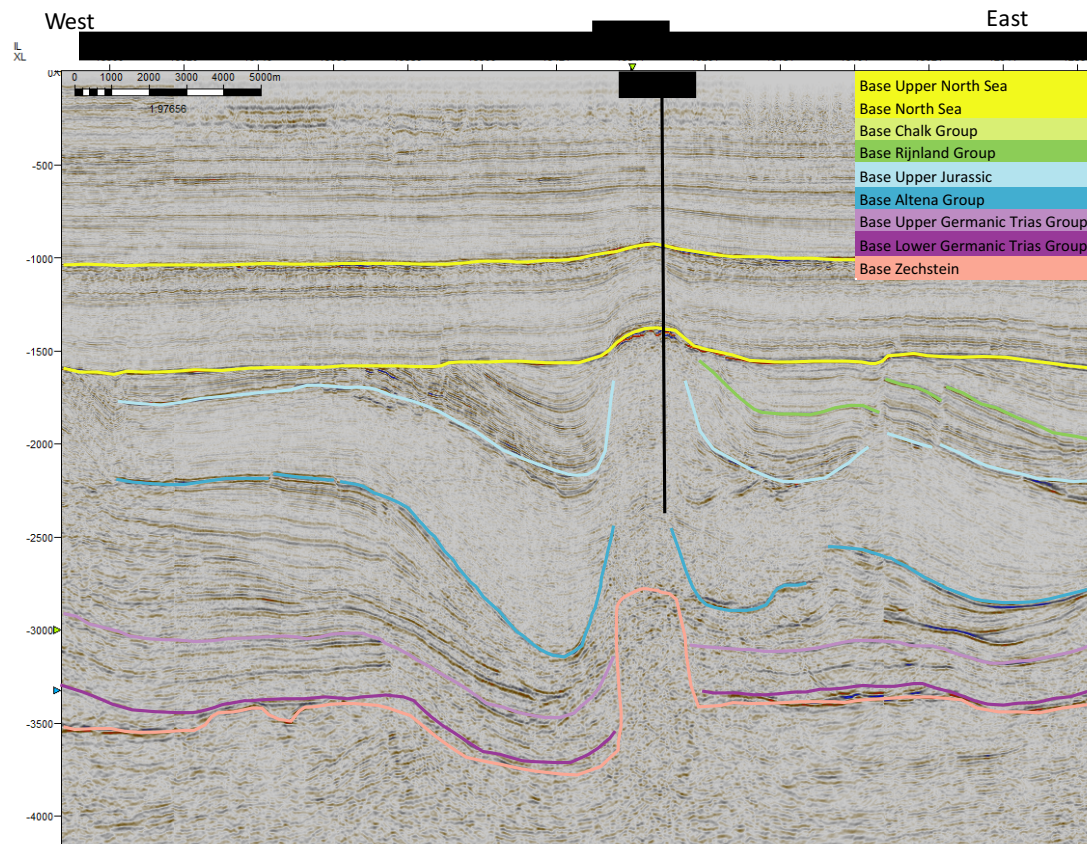


Figure 21: Cross line through well X in which the bases of the main stratigraphic groups are highlighted in two-way travel time. At the crest of the salt structure, the Chalk and Rijland Group are located directly below the base of the North Sea Group, which is not visualized at this scale

The depth distribution of the data points (Figure 22) shows that a trend can be observed in the S_H orientations. With respect to the regional NW-SE S_H trend (blue dashed line), it is seen that the difference between the data points and the regional trend decreases when moving upward. In the Zechstein, the S_H orientations deviate more from the NW-SE trend than the data in the Rijnland and Chalk Group, suggesting that the influence of the salt structure on the in-situ stress field becomes less towards the crest of the structure. Due to this wide range in horizontal stress orientations, the dataset has a relatively high circular standard deviation of 35.6° .

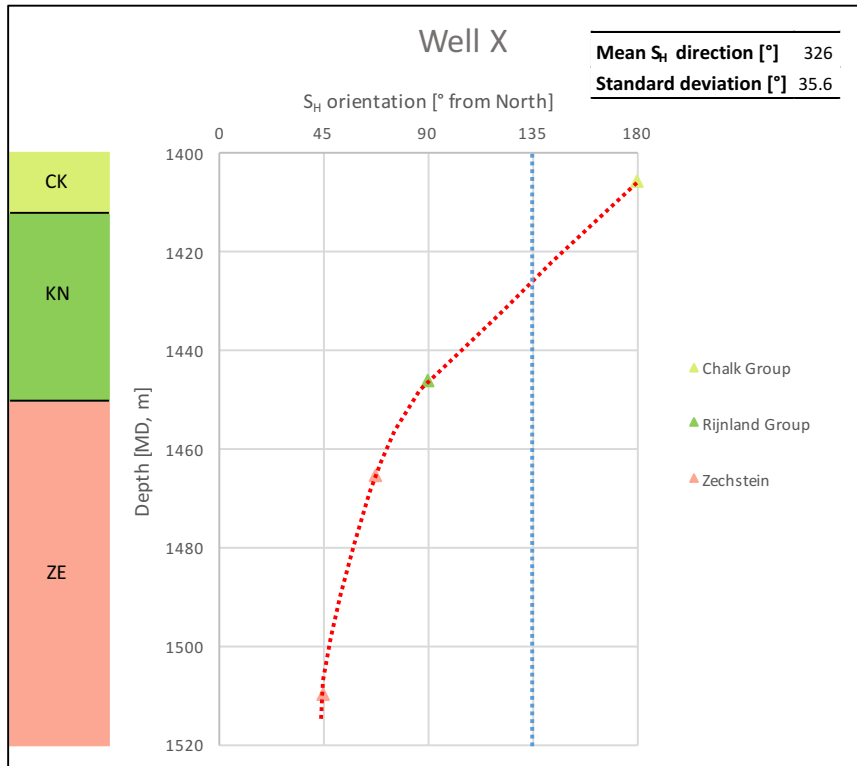


Figure 22: Distribution of acoustic analysis data in well X. The red dashed line indicates the observed trend, whereas the blue dashed line indicates the regional NW-SE S_H trend. CK = Chalk Group; KN = Rijnland Group; ZE = Zechstein.

The horizontal depth slices in Figures 23-26 indicate the position of the stress measurements relative to the location of the salt structure. In the Chalk and Rijnland Group (Figures 23-24), the data points are located on the flank of the salt structure, whereas in the underlying Zechstein, the data points are clearly situated in the centre of the structure (Figures 25-26). It is important to note that these seismic amplitude images only give a rough indication of the location of the salt structure as accurate salt imaging is not straightforward.

In the Chalk Group (Figure 23), the observed N-S S_H direction is not in agreement with the stress patterns described in numerous studies on salt structures (Davis & Engelder, 1985; Davis et al., 2000; Schutjens et al., 2012; Teufel & Farell, 1990). They note that at the flanks of a salt structure, the maximum horizontal stress should be oriented perpendicular to the salt-sediment interface, as indicated with black dashed arrow.

At the depth of the second data point (Figure 24), the S_H orientation in the Rijnland Group follows more closely the expected black dashed arrow, however, the measurement is still not completely perpendicular to the boundary of the salt structure.

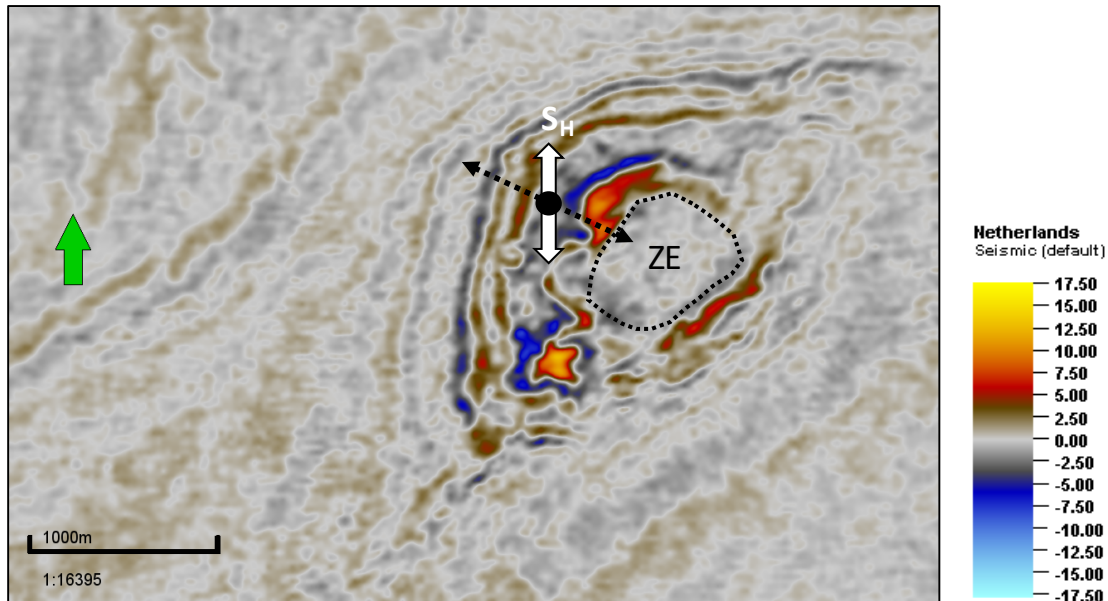


Figure 23: Horizontal depth slice at the Chalk Group data point (-1404 m). The white arrow indicates the observed N-S S_H orientation, whereas the black dashed arrow displays the expected S_H direction normal to the boundary of the salt structure. The boundary between the surrounding sediment and the salt structure (ZE) is highlighted with the black dashed circle.

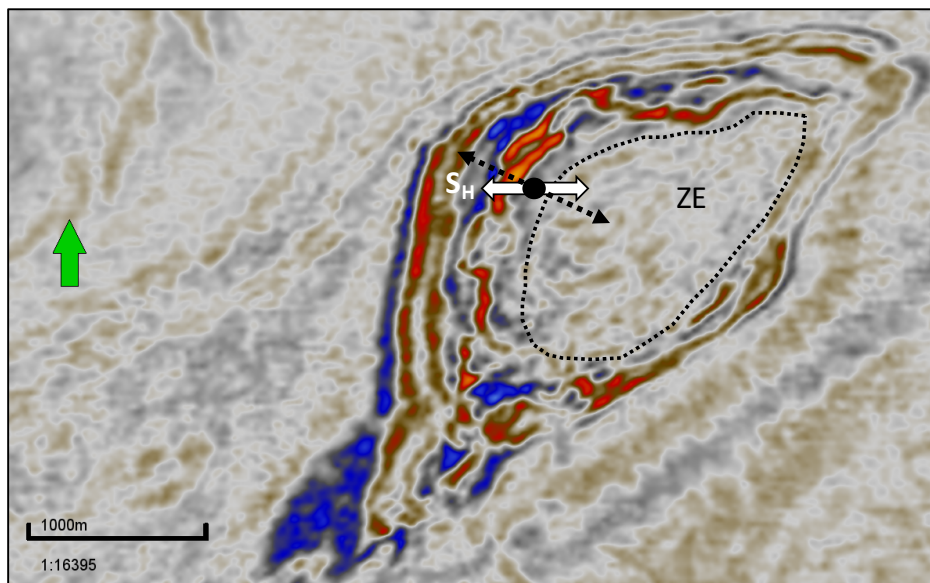


Figure 24: Depth slice at the Rijnland Group data point (-1444 m) in which the white arrow indicates the observed E-W S_H orientation.

In contrast to the previous two stress measurements, the third data point is located in the salt structure (Figure 25). The ENE-WSW S_H direction is not oriented at right angles to the salt-sediment interface but

seems to follow the elongated shape of the structure. This is even more pronounced at a depth of 1510 m (Figure 26) where the NE-SW S_H direction in the Zechstein can be related to the ridge shape of the salt structure. The horizontal stress measurement closely follows the NE-SW axis of the elongated structure and therefore it is suggested that the measured S_H orientation is a direct consequence of the shape of this structure.

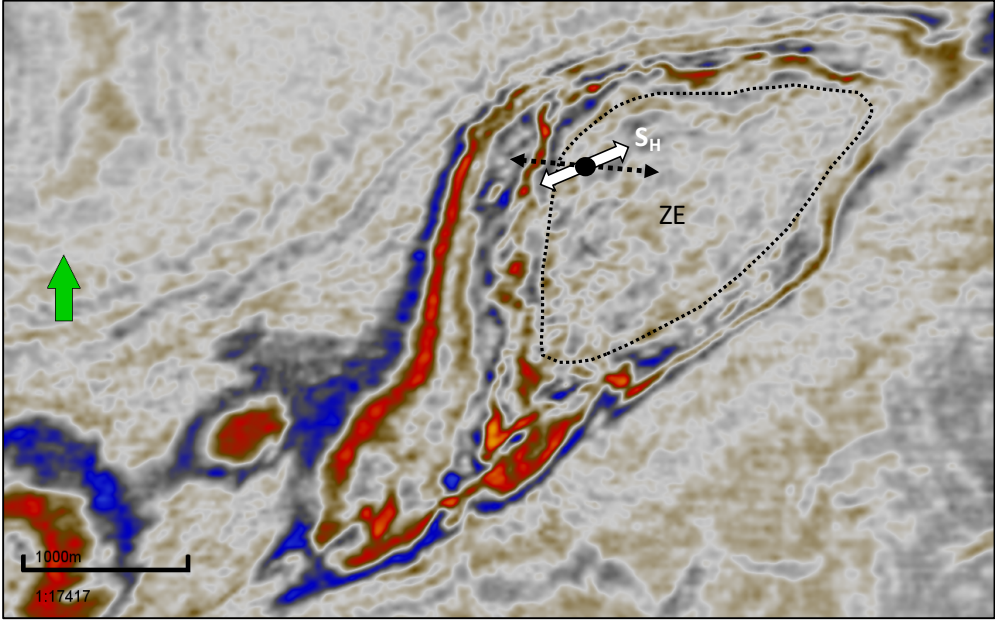


Figure 25: Depth slice at the Zechstein data point (-1464 m). The white arrow indicates the observed ENE-WSW S_H orientation.

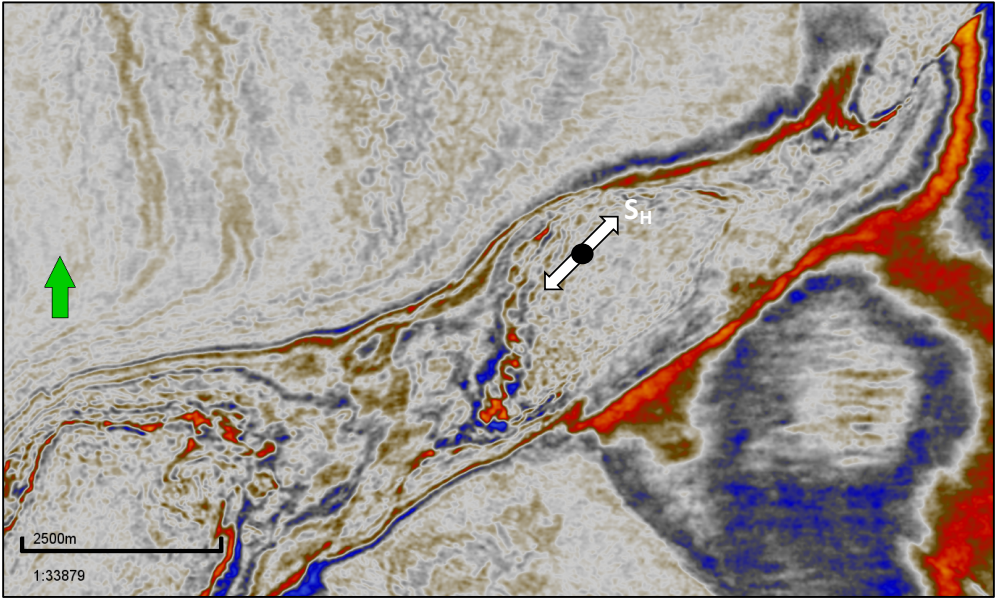


Figure 26: Depth slice at the Zechstein data point (-1510 m) in which the white arrow indicates the observed NW-SE S_H orientation.

6.3 Normal faulting

In the offshore well L09-12, break-outs detected with an acoustic CBIL imager display horizontal stress directions that deviate considerably from the regional NW-SE S_H trend. Figure 27 shows that L09-12 has been drilled in an area where the Zechstein formation is of minimum thickness. However, it is located in close proximity of an east-west trending fault, which is bounded on both sides by NW-SE trending faults. In the north-south crossline through L09-12 (Figure 28), it is seen that this east-west trending fault can be characterized as a normal fault. The combination of a significant fault offset (~346 m) and a relatively small distance to the borehole (< 550 m) can have a considerable effect on the orientation of stress-induced borehole features.

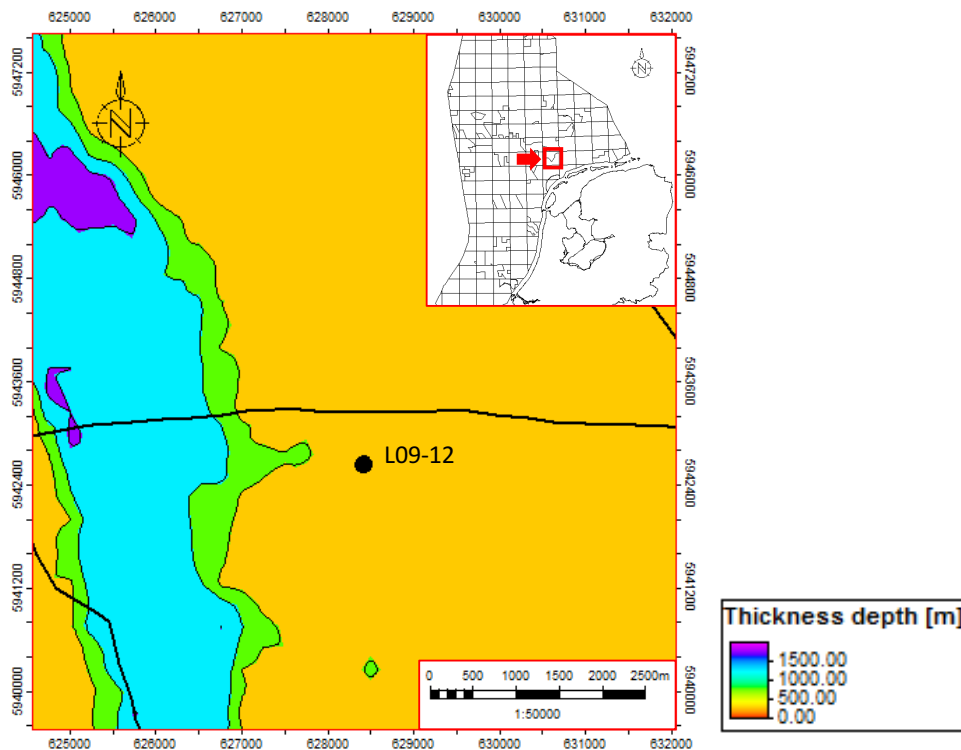


Figure 27: Zechstein thickness map including the major faults (in black) in the area of well L09-12. Faults have been mapped by NLOG (2015).

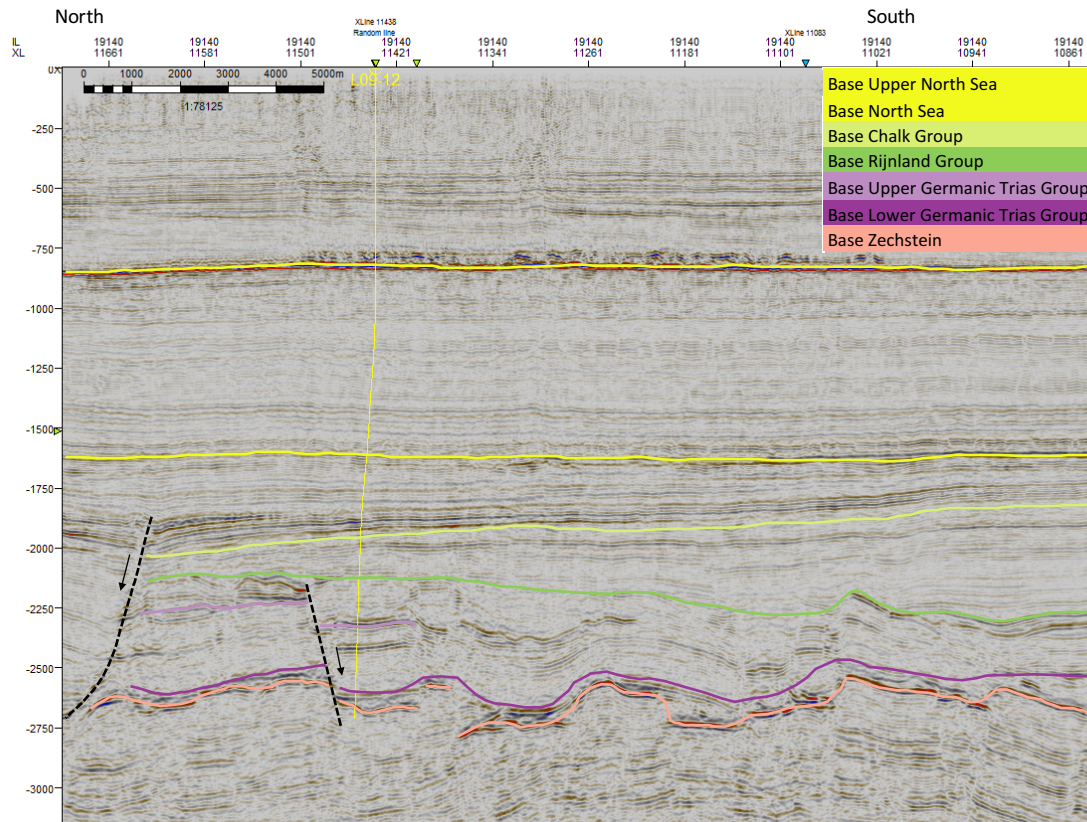


Figure 28: Cross line through well L09-12 in which the bases of the main stratigraphic groups are highlighted in two-way travel time. The normal fault and its major offset (± 346 m) on the northern side of the well has clearly affected the Lower and Upper Germanic Trias Groups.

Figure 29a shows that the majority of the break-outs in the Upper and Lower Germanic Trias Groups display an approximate N-S S_H direction, resulting in a mean S_H orientation of 348.9° . Two of the break-outs in the Upper Germanic Trias Group indicate a NW-SE S_H direction and thus have not rotated with respect to the regional NW-SE trend (blue dashed line). In map view, Figure 29b illustrates that the mean S_H direction has rotated approximately 34° with respect to the regional trend, which results in a S_H trajectory roughly perpendicular to the strike of the east-west trending normal fault.

This S_H orientation is not in accordance with the models of Anderson (1951) for active and semi-active (prone to reactivation) normal faults. For these two types of faults, break-outs should form perpendicular to the fault plane, resulting in S_H orientations parallel to the fault strike. This suggests that the normal fault near L09-12 is inactive and that the S_H directions have been deflected from the regional NW-SE S_H trend due to a contrast in mechanical properties between the fault and the surrounding host rock. The maximum horizontal stress trajectories will deflect from the NW-SE orientation and orient normal to the fault strike when the fault is mechanically stiffer than the host rock (Figure 30).

The fact that the two break-outs in the Upper Germanic Trias Group have not been deflected from the NW-SE S_H trend, suggests that at these shallower depths the distance between the fault and borehole is too large to have an impact on the stress-induced borehole features. However, it could also be explained by the incorrect usage and interpretation of image logs (Brudy & Kj rholt, 2001).

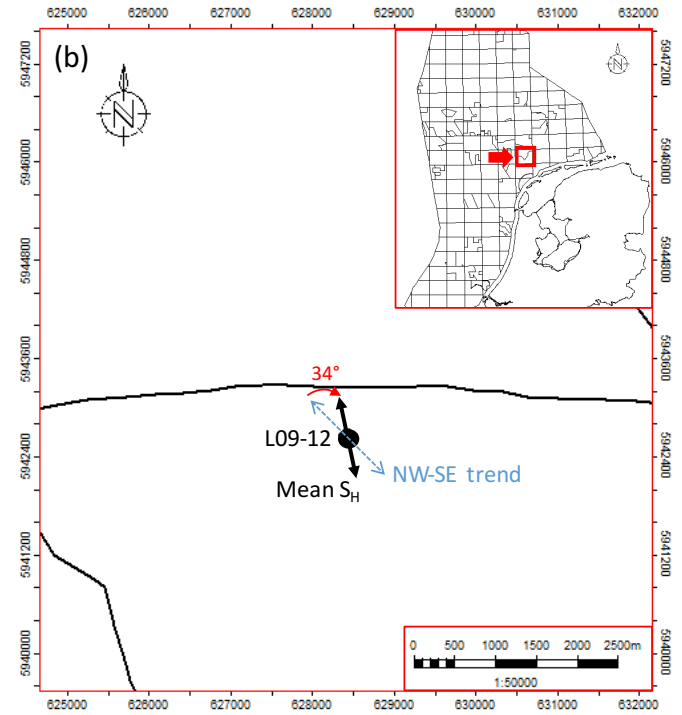
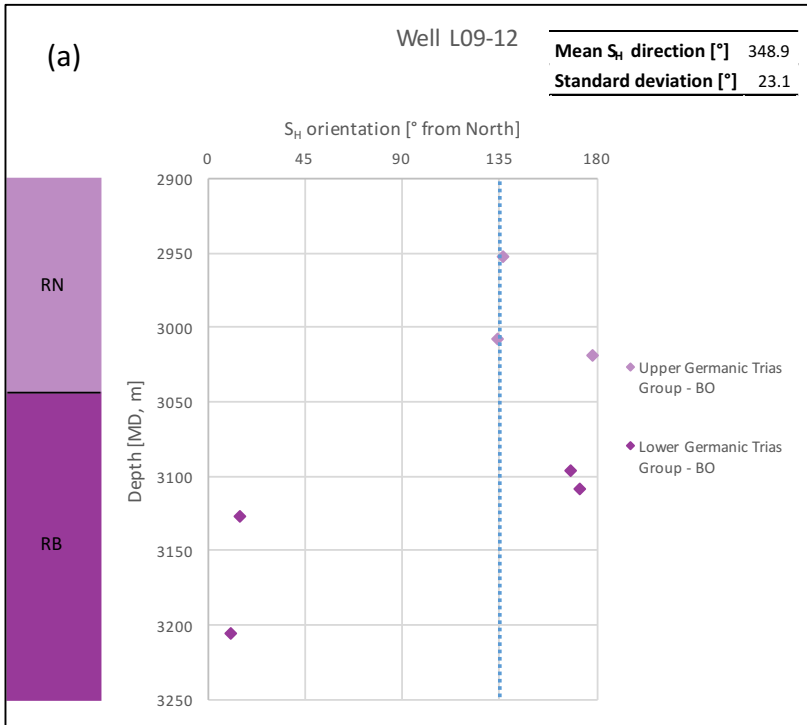


Figure 29: (a) Distribution of break-outs with depth in well L09-12. The blue dashed line indicates the regional NW-SE S_H trend. RN = Upper Germanic Trias Group; RB = Lower Germanic Trias Group. (b) Map view of L09-12 with respect to the east-west trending normal fault in black. The mean S_H direction is given in black, whereas the blue dashed line shows the regional NW-SE S_H trend.

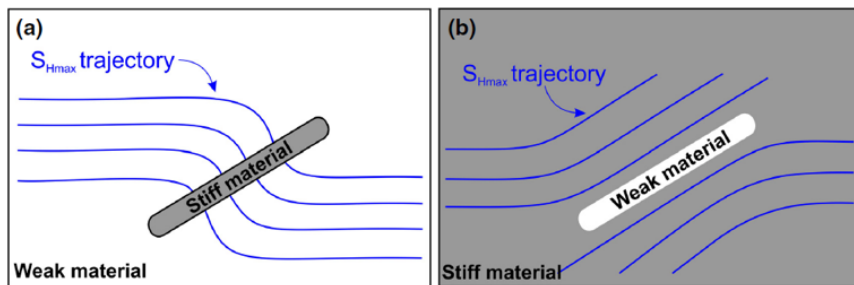


Figure 30: (a) Map view: In the vicinity of faults, which are mechanically stiffer than the host rock, S_H trajectories orient normal to the fault plane. (b) In case of mechanically weak faults, S_H trajectories align parallel to the fault plane.

7. In-situ stress regimes in the northeast of the Netherlands

In the northeast of the Netherlands, the area of the Groningen field is characterized by a normal faulting stress regime at reservoir depth (Rotliegend) (Vandycke, 2002; Van Gent et al., 2009). However, it is unclear whether this in-situ stress regime also applies to the over- and underlying formations. A difficulty in determining the stress regime in these formations, is the accurate characterization of the maximum horizontal stress, which is not straightforward. In contrast to the vertical and minimum horizontal stress, S_H cannot be measured in-situ (Zoback, 2010). Besides that, it is much more difficult to assess the stress regime(s) in the near-surface region as non-tectonic processes affect the in-situ stresses (Engelder & Sbar, 1984).

To characterize the stress regime(s) at a specific location in the Groningen field, five one-dimensional in-situ stress models will be discussed, which are based on different boundary conditions and additional assumptions. As such, the sensitivity of the in-situ stress regime to different boundary conditions can be studied, especially near Earth's surface.

7.1 Overview of models

The 1D in-situ stress models are based on the stratigraphic column of well ZRP-01, which is located in the northern part of the Groningen field (Figure 31). Therefore, the in-situ stress profiles shown in Section 7.2 are only valid at the location of ZRP-01 because lateral variations in lithology, thickness, porosity and fluid type can have an important impact on the vertical stress profile (Verweij et al., 2016).

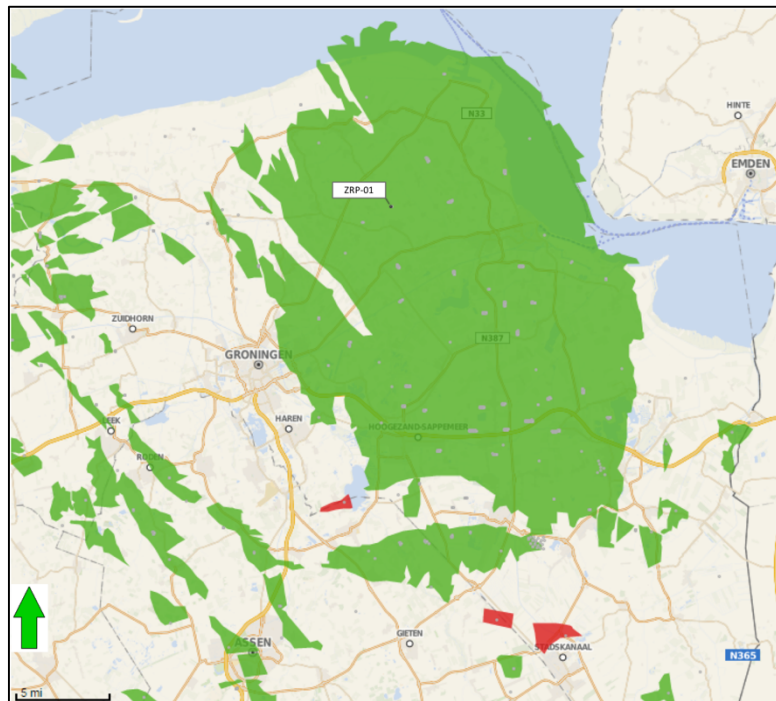


Figure 31: Map of the northeast of the Netherlands in which gas and oil fields are coloured green and red, respectively. Well ZRP-01 is indicated with the black solid circle.

In all 1D models, it is assumed that the vertical stress (S_v) is controlled by the overburden. At each specific depth, the vertical stress is calculated with the following equation (Zoback, 2010):

$$S_v = \int_0^z \rho_b(z) \cdot g \cdot dz \quad (1)$$

where z is the specific depth, ρ_b the formation bulk density which is a function of depth and g the gravitational acceleration.

The formation bulk densities used for computing this integration, as well as the fluid density and elastic properties of each stratigraphic unit, are given in Table 5. In all models, a hydrostatic fluid density of 1030 kg/m³ has been taken. The values of the different parameters are based on studies performed on the various formations in the Groningen field. More details about the sources of the given input data can be found in Appendix F.

Table 5: Stratigraphic column of ZRP-01, as well as the corresponding bulk and fluid densities, and elastic properties.

Stratigraphy	TVD Base [m]	Bulk density [kg/m ³]	Fluid density [kg/m ³]	Young's Modulus [GPa]	Poisson's ratio [-]
Upper North Sea Group	444	2050	1030	2	0.30
Lower North Sea Group	824	1950	1030	2	0.30
Chalk Group	1759	2350	1030	10	0.25
Rijnland Group	1833	2350	1030	16	0.25
Lower Germanic Trias Group	2037	2350	1030	16	0.25
Zechstein	2824	2500	1030	50	0.30
Rotliegend	3111	2350	1030	27.5	0.18
Limburg Group	5000	2700	1030	40	0.20

7.1.1 Gravity-only models

Model 1

Models 1 to 3 are based on the assumption that the overburden is the only source of horizontal stress. If an overburden stress is applied to a unit volume, the horizontal stress increases in all directions due to the Poisson effect. To what extent the horizontal stress increases, depends on the Poisson's ratio of the rock body (Zoback, 2010). On the basis of this gravity-only assumption, Eaton (1969) proposed the following equation for the determination of the minimum horizontal stress:

$$S_h = \frac{\nu}{1-\nu} (S_v - P_p) + P_p \quad (2)$$

where ν is the Poisson's ratio and P_p the pore pressure.

In Model 1, the base case, the minimum and maximum horizontal stress are equal in magnitude as the overburden is the only source of stress. To determine the stress magnitudes at all depths, it has been assumed that the Poisson's ratio varies per stratigraphic group, as indicated in Table 5.

Model 2

Also in the second model, equation (2) serves as basis for the profiles of S_h and S_H . However, it differs from Model 1 in the way that Model 2 is based on the in-situ stress data and assumptions of Y (XXXX). In contrast

to Model 1, a constant effective stress ratio ($ESR = \frac{\nu}{1-\nu}$) with depth has been assumed to determine the minimum and maximum horizontal stress at all depths. This implies that the Poisson's ratio has not been varied per stratigraphy, which results in a constant stress gradient with depth.

Y (XXXX) selected an ESR of 0.4 as the S_h profile then closely matches the S_h magnitudes which have been derived from leak-off test data in the Groningen field. This leak-off data has been collected at different locations and in different formations (Rotliegend up to Chalk Group).

$$S_h = 0.4(S_v - P_p) + P_p \quad (3)$$

Break-outs encountered in the Groningen field were used to determine the magnitude of S_H at the depth of these break-outs. Subsequently, an ESR of 0.55 was selected by Y (XXXX) to obtain a S_H profile, which fits the S_H magnitudes derived from these break-outs. By assuming a constant ESR with depth, the magnitude of S_H can also be determined in the over- and underlying formations:

$$S_H = 0.55(S_v - P_p) + P_p \quad (4)$$

Model 3

Model 3 is the third gravity-only model, which is based on the methods and assumptions of Van Eijs (2015). As in Model 2, the magnitude of S_h is based on the assumption of a constant Poisson's ratio with depth and thus a constant stress gradient. For the Groningen field, Van Eijs (2015) assumed a stress gradient of 1.6 bar/10 m.

$$S_h = 1.6 \frac{\text{bar}}{10 \text{ m}} \quad (5)$$

In contrast to Model 2, the magnitude of the maximum horizontal has been determined by performing a differential strain analysis on five plugs from a core in the Groningen field. It allows one to determine the in-situ stress magnitudes from strain measurements by assuming that the deformation characteristics of a rock are influenced by the present-day stress state in the subsurface (De Bree, 1988). Moreover, it is assumed that all anisotropy in the plug is stress-induced and not the result of compositional differences. Based on these assumptions, the maximum horizontal stress can be determined using equation (6):

$$S_H = 1.32(S_h - P_p) + P_p = 1.32 \cdot S_h - 0.32 \cdot P_p \quad (6)$$

7.1.2 Gravity-tectonic models

Model 4a and b

In the fourth model, a (sub)-horizontal tectonic stress has been assumed, in addition to gravity. This tectonic stress component can originate from e.g. plate driven stresses and lithospheric flexure, which are ultimately the result of lateral changes in the density and thickness of the lithosphere (Zoback, 2010). If one assumes a constant tectonic stress with depth and that the Earth's surface can be described as a free surface, the equations for the minimum and maximum horizontal stress are written in the following way (Bertotti et al., 2017):

$$S_h = \frac{\nu}{1-\nu} (S_v - P_p) + \frac{\nu}{1-\nu} S_{tect} + P_p \quad (7)$$

$$S_H = \frac{\nu}{1-\nu} (S_v - P_p) + S_{tect} + P_p \quad (8)$$

where S_{tect} is the tectonic stress component.

In Model 4a, a tectonic stress component of 5 MPa has been assumed, which is increased to 10 MPa in Model 4b. In both models, the Poisson's ratio varies per stratigraphic group.

7.1.3 Tectonic strain model

Model 5

The fifth model assumes that a (sub)-horizontal tectonically induced strain is applied to a unit volume under plane strain conditions. The tectonically induced strain is constant with depth and only applied in the direction of the maximum horizontal stress (Fjaer et al., 2008). In addition, it is assumed that the magnitude of S_h can be determined as in Model 1. Based on these assumptions, S_h and S_H are determined in the following way:

$$S_h = \frac{\nu}{1-\nu} (S_v - P_p) + P_p \quad (9)$$

$$S_H = \frac{E}{1+\nu} \varepsilon_H + S_h \quad (10)$$

where E is the Young's modulus and ε_H the tectonic strain in the direction of S_H .

In this model, a constant tectonic strain of $2 \cdot 10^{-4}$ has been assumed, whereas the Young's modulus and Poisson's ratio vary per stratigraphic group.

An overview of all models, including the underlying assumptions and the equations for S_h and S_H , is given in Table 6.

Table 6: Overview of the assumptions and corresponding equations for the five different in-situ stress models.

	Model 1	Model 2	Model 3	Model 4a and b	Model 5
Assumptions	<ul style="list-style-type: none"> - Gravity is the only source of stress - S_h and S_H result from the Poisson effect caused by the overburden - Poisson's ratio differs per stratigraphic group 	<ul style="list-style-type: none"> - Gravity is the only source of stress - S_h and S_H result from the Poisson effect caused by the overburden - Constant Poisson's ratio with depth 	<ul style="list-style-type: none"> - Gravity is the only source of stress - S_h results from the Poisson effect caused by the overburden - S_H results from a differential strain analysis - Constant Poisson's ratio with depth 	<ul style="list-style-type: none"> - Constant (sub)-horizontal tectonic stress with depth in the direction of S_H - S_h results from the Poisson effect caused by the overburden and tectonic stress - S_H results from the tectonic stress and the Poisson effect caused by the overburden - Poisson's ratio differs per stratigraphic group 	<ul style="list-style-type: none"> - Constant (sub)-horizontal tectonic strain with depth in the direction of S_H - S_h results from the Poisson effect caused by the overburden - S_H results from the tectonic strain and the Poisson effect caused by the overburden - Poisson's ratio and Young's modulus differ per stratigraphic group
Equations	$S_h = \frac{\nu}{1-\nu} (S_v - P_p) + P_p$ $S_H = \frac{\nu}{1-\nu} (S_v - P_p) + P_p$	$S_h = 0.4(S_v - P_p) + P_p$ $S_H = 0.55(S_v - P_p) + P_p$	$S_h = 1.6 \frac{\text{bar}}{10 \text{ m}}$ $S_H = 1.32 \cdot S_h - 0.32 \cdot P_p$	$S_h = \frac{\nu}{1-\nu} (S_v - P_p) + \frac{\nu}{1-\nu} S_{tect} + P_p$ $S_H = \frac{\nu}{1-\nu} (S_v - P_p) + S_{tect} + P_p$	$S_h = \frac{\nu}{1-\nu} (S_v - P_p) + P_p$ $S_H = \frac{E}{1+\nu} \varepsilon_H + S_h$

7.2 Results

7.2.1 Gravity-only models

The in-situ stress profiles for the three gravity-only models (1 to 3) are shown in Figures 32 to 34. In the base case (Model 1, Figure 32), the effect of a Poisson's ratio that varies per stratigraphy is clearly seen in the horizontal stress profiles. The large difference in Poisson's ratio between the Zechstein and Rotliegend causes a significant drop in the magnitudes of S_h and S_H .

In Model 2 (Figure 33), the minimum and maximum horizontal stress increase linear with depth because of a constant ESR. Due to a different ESR in the equations of S_h and S_H , the two horizontal stresses increase at different rates. A jump in magnitude occurs in the Zechstein, where both horizontal stresses become equal to the overburden stress. An ESR of one has been assumed by Y (XXXX) for the Zechstein as the salt behaves as an incompressible material.

Model 3 displays the same linear behaviour for both horizontal stresses, however, the different geomechanical properties of, for example, the Zechstein have not been taken into consideration. In all three models, the vertical stress is the largest principal stress, implying that a normal faulting stress regime would exist over the entire depth interval.

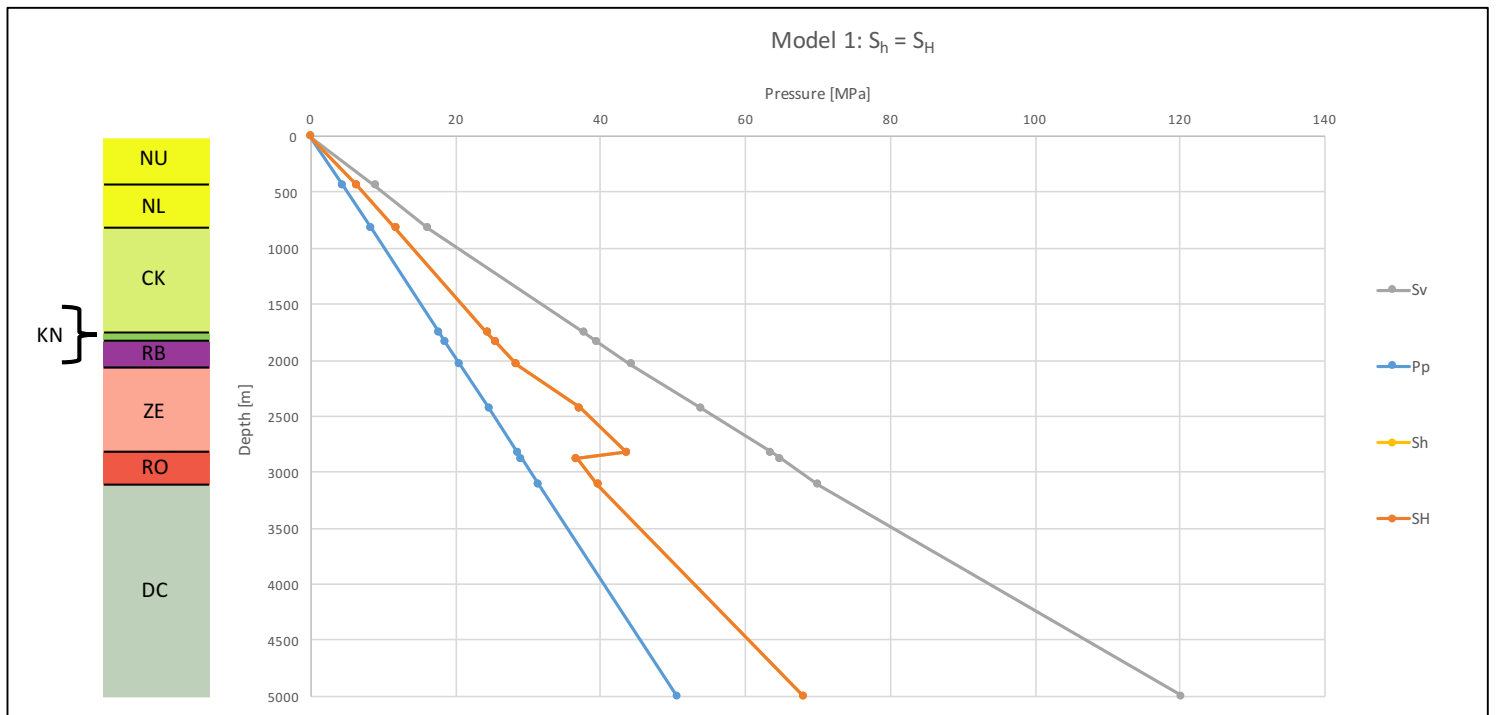


Figure 32: Model 1 - Stress profiles and pore pressure as function of depth, based on the stratigraphy of well ZRP-01. NU: Upper North Sea Group; NL = Lower North Sea Group; CK = Chalk Group; KN = Rijnland Group; RB = Lower Germanic Trias Group; ZE = Zechstein; RO = Rotliegend; DC = Limburg Group.

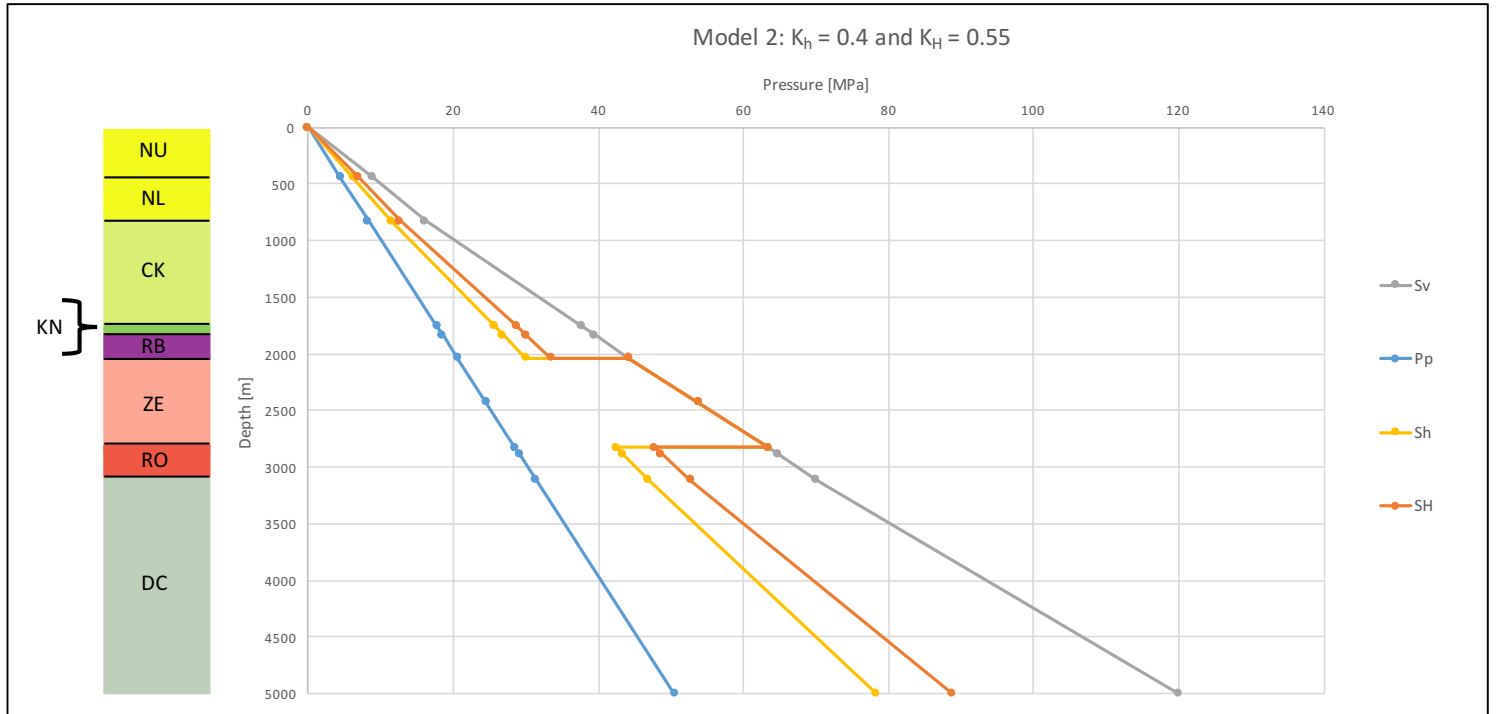


Figure 33: Model 2 – Stress profiles and pore pressure as function of depth. An ESR of one has been assumed for the horizontal stresses in the Zechstein formation (Y, XXXX).

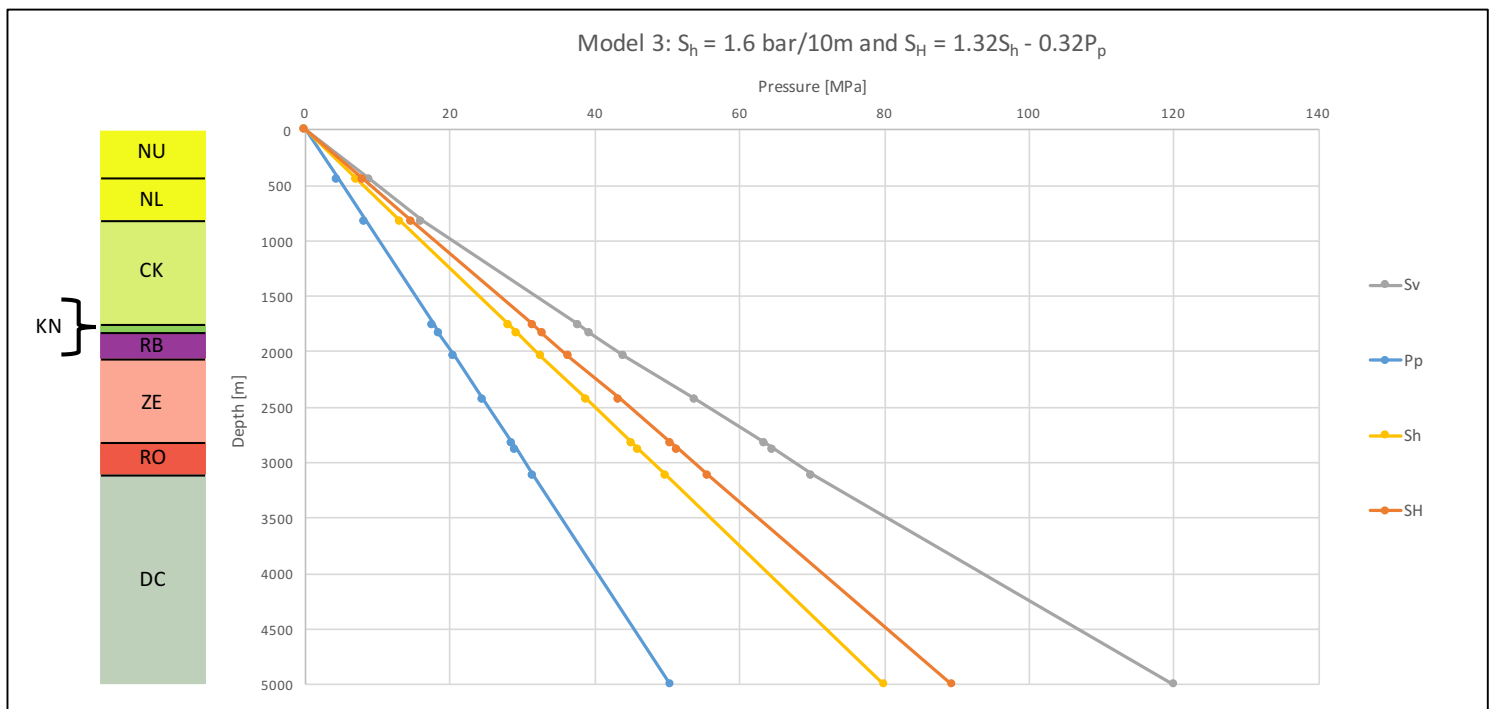


Figure 34: Model 3 – Stress profiles and pore pressure as function of depth.

7.2.2 Gravity-tectonic models

Figures 35 and 36 display the in-situ stress profiles of Models 4a and b, which include a constant tectonic stress component, in addition to gravity.

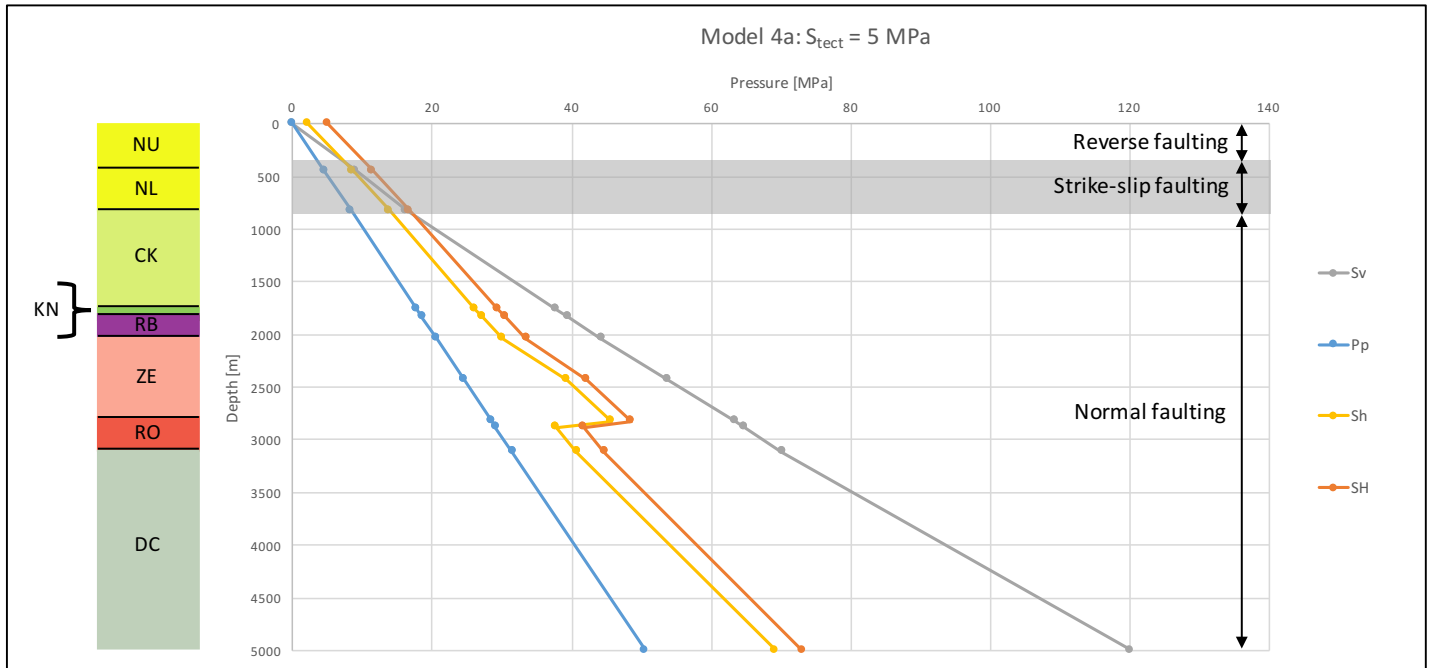


Figure 35: Model 4a - Stress profiles and pore pressure as function of depth for a tectonic stress component of 5 MPa. The arrows indicate the three different in-situ stress regimes.

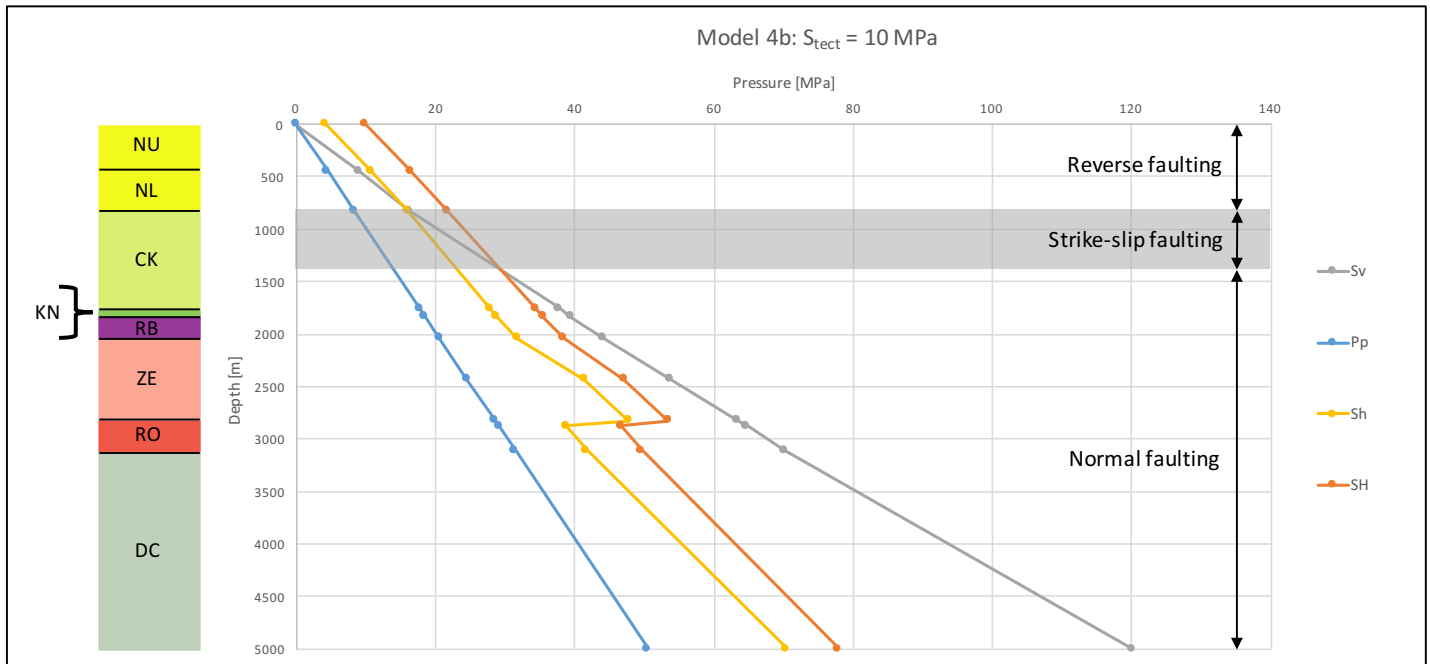


Figure 36: Model 4b - Stress profiles and pore pressure as function of depth for a tectonic stress component of 10 MPa.

The addition of a tectonic stress component has a clear effect on the in-situ stress regimes. In both models, three depth intervals can be recognized in which the relative magnitudes of the in-situ stresses differ. Figure 35 and Table 7 show that a reverse and strike-slip faulting regime exist in the upper 920 m of the subsurface in case of 5 MPa tectonic stress. A normal faulting stress regime is observed in the remaining interval up to 5 km depth. The same distribution of stress regimes is observed in Figure 36 (Model 4b), however, due to the larger tectonic stress component (10 MPa), the vertical stress becomes the maximum principal stress at a larger depth.

Table 7: Depth intervals, relative stress magnitudes and the corresponding in-situ stress regime for (left) Model 4a with a tectonic stress component of 5 MPa, and (right) Model 4b with a tectonic stress component of 10 MPa.

Depth interval [m]	σ_1	σ_2	σ_3	In-situ stress regime
0 - 390	S_H	S_h	S_v	Reverse faulting
390 - 920	S_H	S_v	S_h	Strike-slip faulting
920 - 5000	S_v	S_H	S_h	Normal faulting

Depth interval [m]	σ_1	σ_2	σ_3	In-situ stress regime
0 - 800	S_H	S_h	S_v	Reverse faulting
800 - 1380	S_H	S_v	S_h	Strike-slip faulting
1380 - 5000	S_v	S_H	S_h	Normal faulting

7.2.3 Tectonic strain model

Figure 37 shows the stress profiles of Model 5, which includes a tectonically induced strain of $2E^{-4}$. The addition of a strain in the direction of S_H has an effect on the in-situ stress regime in the upper 50 m of the subsurface (see inset). In this depth interval, the maximum horizontal stress is the largest principal stress, whereas the vertical stress is the intermediate principal stress. Consequently, a strike-slip faulting regime exists in this depth interval, after which it changes to normal faulting.

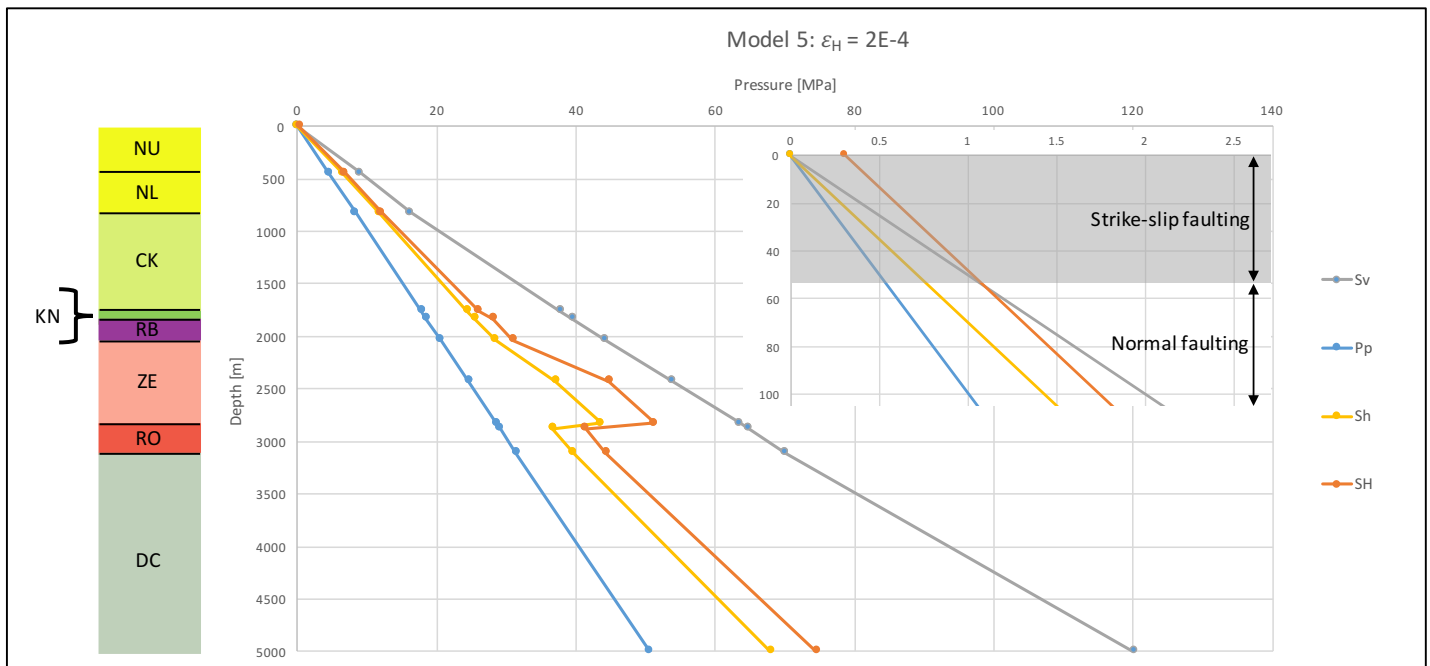


Figure 37: Model 5 - Stress profiles and pore pressure as function of depth for a tectonically induced strain of $2E^{-4}$.

7.2.4 Comparison of models

The boundary conditions and assumptions used to quantify the in-situ stresses, have a significant impact on the in-situ stress regimes in well ZRP-01. Although all models indicate a normal faulting stress regime in the Rotliegend and in the underlying formations, different stress regimes can be observed at shallow and intermediate depths (0 to 1400 m). At these depths, the gravity-only models indicate a normal faulting stress regime, whereas the models with a tectonic stress component show reverse and strike-slip faulting. In case of a tectonically induced strain, a strike-slip faulting regime can be observed in the upper 50 m of the subsurface.

In terms of the anisotropy between S_h and S_H , Figure 38 shows that Models 2 and 3, which are based on the assumptions of Y (XXXX) and Van Eijs (2015), only differ from each other in the Zechstein. At most depths, both models indicate a S_H/S_h ratio between 1.10 and 1.12, with a value of 1.12 at reservoir depth. The effect of a tectonic stress component in Models 4a and b is clearly seen in the interval between Earth's surface and the reservoir, where the horizontal stress anisotropy is significantly larger compared to the other models. However, at reservoir depth, the difference between the S_H/S_h ratio of Model 4 and Models 2/3 is already considerably smaller. In Model 5, the S_H/S_h ratio is almost one in the Lower North Sea Group and Chalk Group, whereas in the Zechstein, the anisotropy is significantly larger compared to Model 2. In the Rotliegend, the average horizontal stress anisotropy of 1.12 is similar to the S_H/S_h ratios of Models 2 and 3.

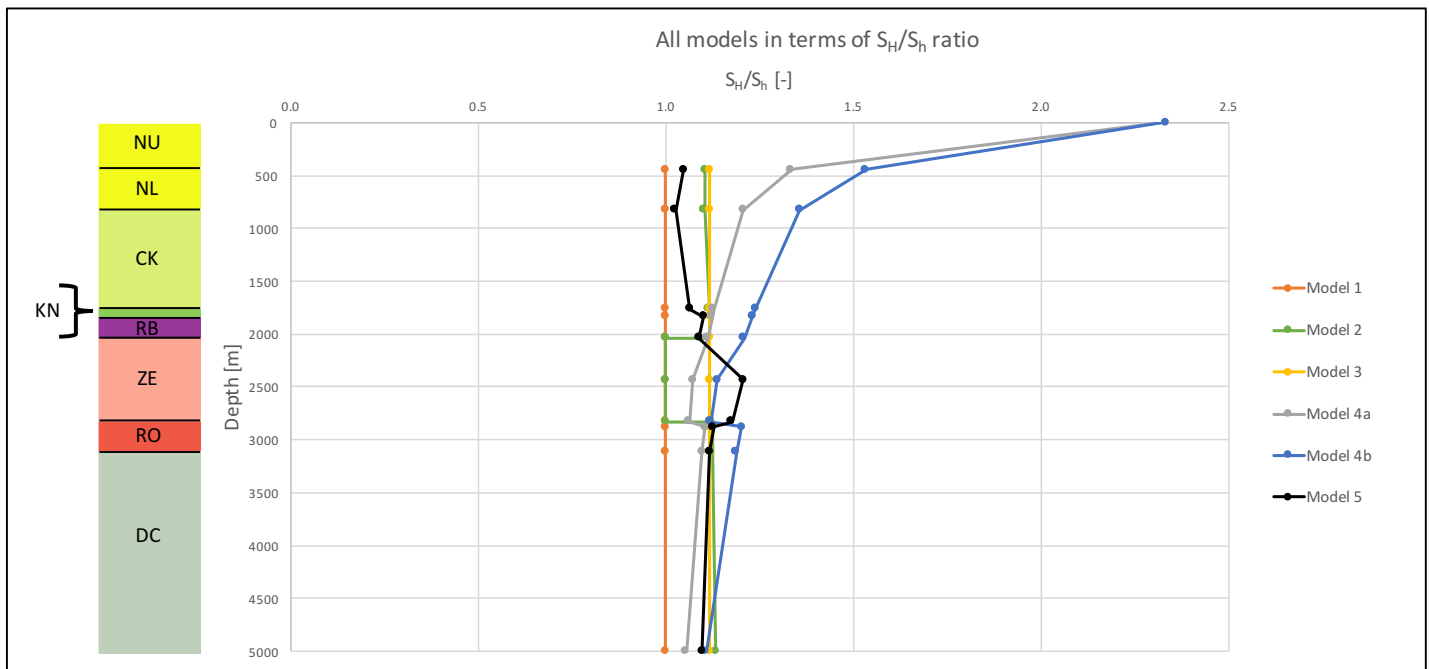


Figure 38: S_H/S_h ratio as function of depth for the five different in-situ stress models.

8. 3D Geomechanical modelling

In the exploration and production industry, 3D geomechanical models are a valuable tool to make predictions of e.g. wellbore stability issues and in-situ stress distributions near geological structures, such as salt domes (Heidari et al., 2015). In this section, the workflow for performing a 3D geomechanical simulation will be described by running a simulation case for a part of the subsurface in the northeast of the Netherlands. As part of the workflow, the simulation results will be discussed as well as the accuracy and uncertainties related to this model.

8.1 Methodology

8.1.1 Model set-up

A 3D geomechanical model of the northeast of the Netherlands has been constructed with the JewelSuite Subsurface Modelling software of Baker Hughes. The objective is to describe the workflow for developing and using a 3D geomechanical model, which can serve as basis for future studies. This will be done by performing a basic gravity-only simulation for an area, which is characterized by significant lateral thickness variations due to the presence of smaller and larger salt structures.

In Figure 39, the grey box illustrates the location of the 3D geomechanical model, which covers an area of 44 by 24 km and has a maximum depth of 9.7 km below Earth's surface. The area of interest is characterized by one major salt diapir, which has a diameter of 5 km and a Zechstein thickness up to 3 km. In addition, multiple smaller salt ridges are observed in the centre of the model, where the Zechstein has a thickness of approximately 2 km. Although faults have not been included in this geomechanical model (Figure 40), the area is characterized by four major NW-SE striking faults in the western half of the model. In Appendix G, additional information is given about the various steps to construct this 3D model in JewelSuite.

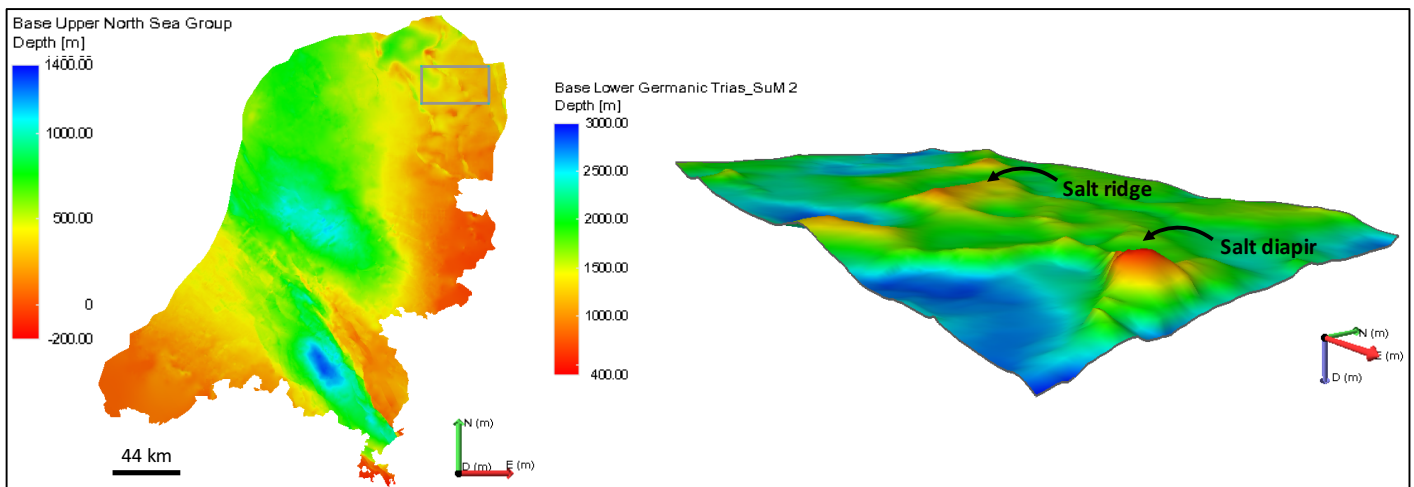


Figure 39: (Left) Top view of the base of the Upper North Sea Group. The grey rectangle indicates the area of which a 3D geomechanical model has been made. All maps show elevation with negative values, whereas depths below surface are displayed by positive values. (Right) Within the model, the base Lower Germanic Trias Group (= top Zechstein) clearly illustrates the presence of a salt diapir and smaller salt structures.

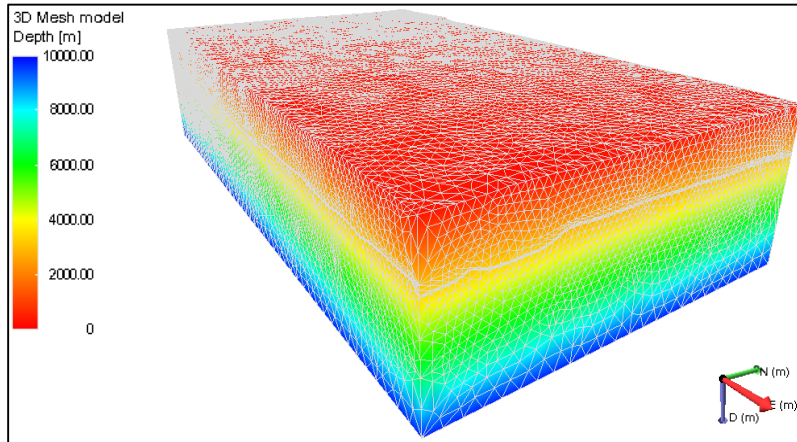


Figure 40: The resulting 3D model in which no faults have been incorporated.

The main input for the geomechanical model are the depth surfaces interpreted from 3D seismics by NLOG (2015). Four stratigraphic units have been included in this model: The Limburg Group, Rotliegend, Zechstein, and the overburden up to base Upper North Sea Group (top surface of model). The material properties of these units originate from studies in the Groningen field, as the field partly overlaps with the modelled area (Table 8).

Table 8: Rock and elastic properties for the four different units in the 3D geomechanical model (source: Appendix F).

Stratigraphy units	Bulk density [kg/m^3]	Young's Modulus [GPa]	Poisson's ratio [-]
Overburden	2210	9.2	0.27
Zechstein	2500	50	0.30
Rotliegend	2350	27.5	0.18
Limburg Group	2700	40	0.20

The use of only the Young's modulus and Poisson's ratio illustrates that all four zones have been modelled as purely elastic. In addition, pore pressure has not been incorporated in this model. Figure 41 illustrates that during the simulation the bottom and sides of the model have been fixed, whereas free movement is allowed at the top of the model.

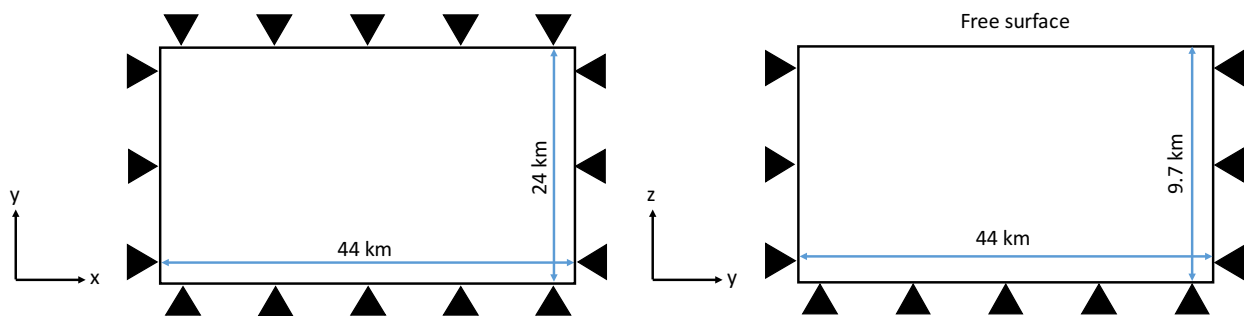


Figure 41: (Left) Top view of the 3D model which indicates that the boundaries do not allow displacement in the x- and y-direction. (Right) Cross-section in the YZ plane shows that the base of the model is also fixed.

8.1.2 Modelling strategy

Prior to running the simulation case, a 1D initial stress state is assigned to the 3D model. In this initial stress state, the minimum and maximum horizontal stress ratios (S_H/S_V and S_H/S_V) are defined with depth. Subsequently, the simulation case is run in which JewelSuite uses the fixed boundaries (Figure 41) to obtain an elastic equilibrium between the gravity, density and initial stress state (Baker Hughes, 2016).

For the workflow, one basic simulation case has been run. In simulation case A, a gravity-only scenario is modelled in which the assumptions and equations of Model 1 (Section 7.1.1) are used to calculate the 1D initial stress state (Figure 42). As gravity is the only source of horizontal stress in simulation case A, it is hypothesized that due to the Poisson effect, the simulation output should show an increase in the horizontal stress magnitudes compared to the initial stress state (the input). Moreover, lateral variations in the thickness of the Zechstein formation should have an effect on the vertical stress distribution.

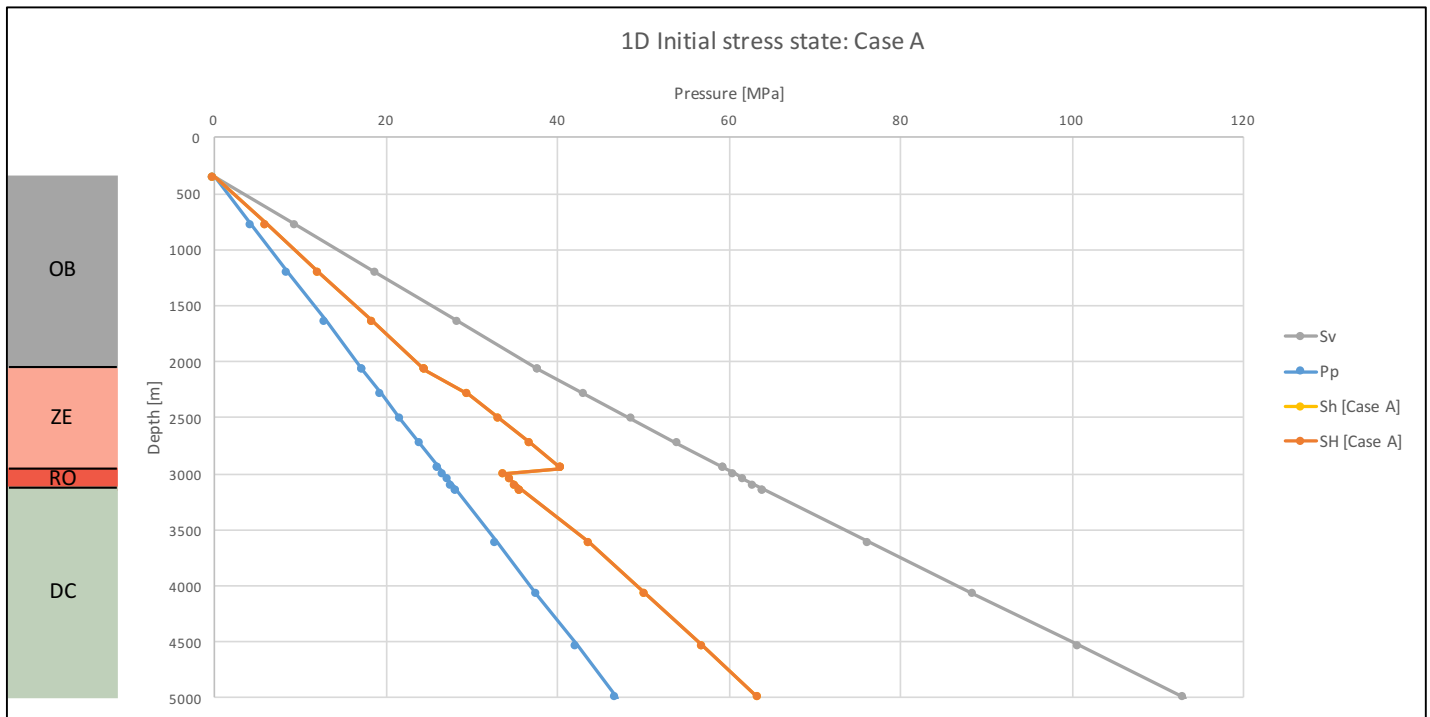


Figure 42: 1D Initial stress state for Case A based on the assumptions and equations of Model 1 (Section 7.1.1). OB = Overburden.

8.2 Results

After running the simulation for Case A, the resulting dataset has been cropped to construct one-dimensional and two-dimensional plots. To obtain 1D graphs of the in-situ stresses with depth, the 3D dataset has been cropped in the horizontal direction to three areas of five by five km. On the other hand, the dataset has been cropped in the vertical direction to obtain 2D plots of the in-situ stress distributions in the XY plane. Figure 43 indicates the locations of these three areas, which are labelled 1, 2 and 3, respectively. It is important to note that the three areas are characterized by different Zechstein thicknesses. Location 1 is situated in an area in which the Zechstein formation has an average thickness

of 500-1000 m, whereas the thickness at location 2 is already much larger: 2000-2500 m. Finally, the third location includes a major salt diapir, resulting in salt thicknesses up to 3000 m. It is expected that these thickness variations will have an impact on the local distribution of the in-situ stresses with depth.

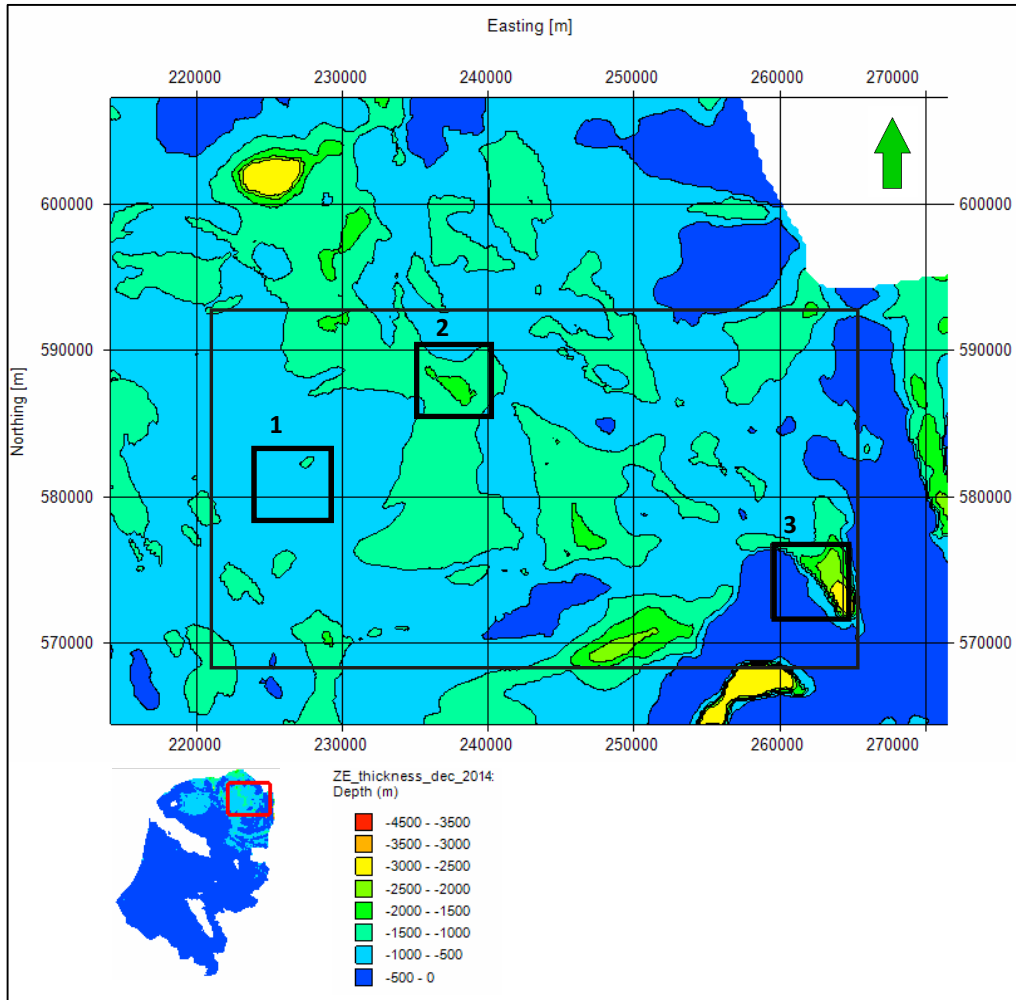


Figure 43: Zechstein thickness map of the modelled area. The model boundary is indicated with the black box, whereas the three analysed regions of 5 x 5 km are highlighted by the smaller black squares.

Figure 44 depicts the pressure-depth plots at the three locations when running simulation case A. If one compares the overburden stress profiles in the different areas at a depth of 5 km, it can be seen that the vertical stress increases from area 1 to 3. This increase is related to the Zechstein thickness variations, which have been highlighted in Figure 43. The Zechstein formation has a bulk density which is larger than those of the over- and underlying stratigraphies, implying that the vertical stress will be larger at locations where the Zechstein is relatively thick. In turn, this increase in S_v between area 1 and 3 explains the simultaneous increase in the minimum and maximum horizontal stress, as S_h and S_H are directly dependent on S_v (Table 9).

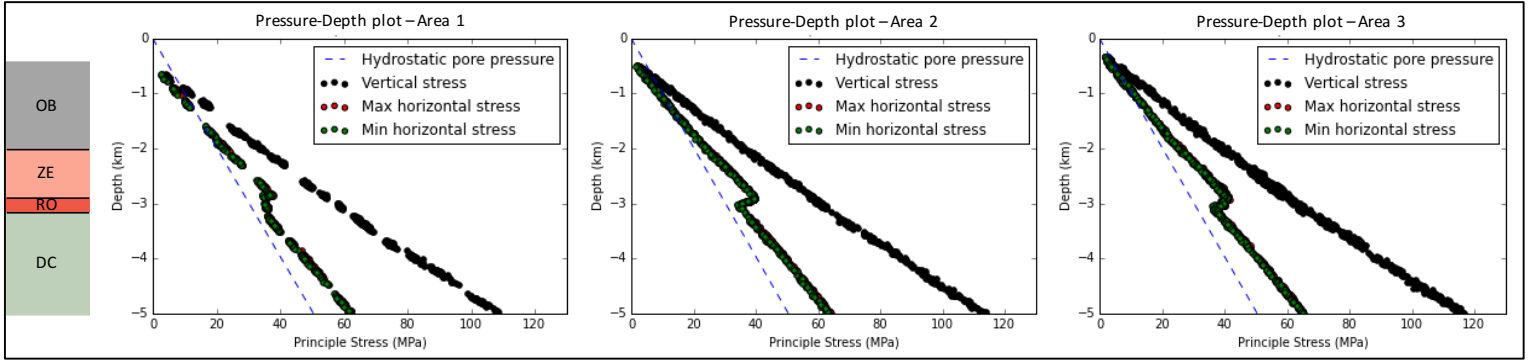


Figure 44: Pressure-depth plots at the three different locations when running case A. The hydrostatic pore pressure curve has been added manually and is not an output of the actual simulation.

Table 9: Case A: In-situ stress values at a depth of 5 km in the three different areas.

Area	S_v [MPa]	S_H [MPa]	S_h [MPa]
1	108.8	62.7	61.9
2	114.2	64.3	63.5
3	116.8	65.6	65.1
<i>Average</i>	<i>113.3</i>	<i>64.2</i>	<i>63.5</i>

If one compares the average in-situ stresses (Table 9) with the initial stress state at a depth of 5 km (Table 10), it is seen that the simulation output hardly differs from the input in this basic simulation case. Lateral variations in the formation thickness seem to have a limited effect on the vertical stress distribution. In area 3, the magnitude of S_v is only 3.3% higher compared to the initial stress state, despite the presence of a salt diapir with a thickness up to 3000 m. Moreover, the Poisson effect has not resulted in a significant increase in the horizontal stress magnitudes. The average value of S_H is only 1.1% higher compared to the initial stress state, whereas the simulation in- and output values of S_h are exactly the same (63.5 MPa).

Table 10: Initial stress values at a depth of 5 km, as shown in Figure 42.

Case	S_v [MPa]	S_H [MPa]	S_h [MPa]
A	113.1	63.5	63.5

In the horizontal plane, Figure 45 shows the distribution of the in-situ stresses over the entire field (44 x 24 km), based on data between 4 and 4.5 km depth. The base of the Zechstein is situated at an average depth of 2952 m, indicating that the stress fields in Figure 45 are located sufficiently below the Zechstein formation. As in the 1D profiles of Figure 44, the colour distribution illustrates that the overburden stress increases when moving from west to east in the model. The 2D images of S_h and S_H indicate a similar distribution of the horizontal stress magnitudes, however, slight differences can still be observed. These differences in contour geometries can be related to the relatively coarse mesh size of the 3D model.

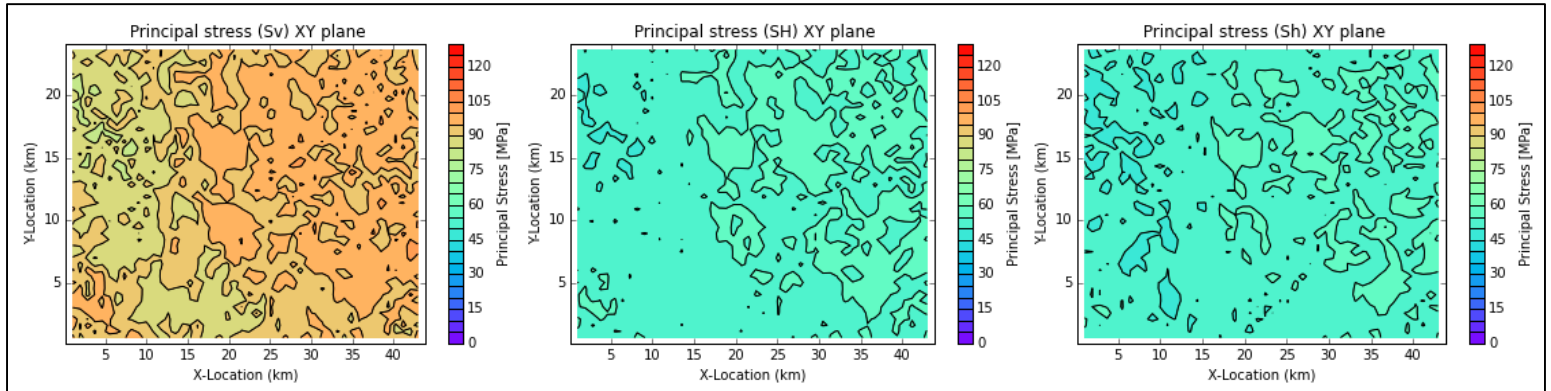


Figure 45: Simulation case A: Distribution of the vertical, minimum and maximum horizontal stress in the XY plane when displaying the data of the entire field (44 x 24 km) between 4 and 4.5 km depth.

In simulation case A, no comparison can be made between the horizontal stress orientations in the 3D model and the collected in-situ stress directions of the Dutch Stress Map. This is due to the fact that no rotations in the horizontal stress directions can be observed (Figure 46), as shear stresses have not been applied to the boundaries of the model and time dependent behaviour of the Zechstein formation has not been modelled.

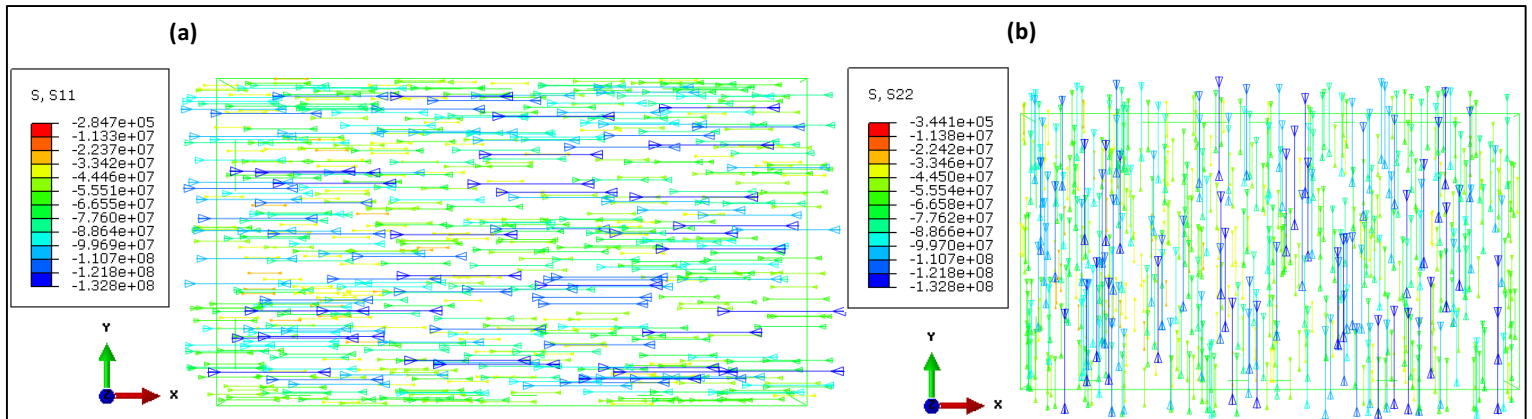


Figure 46: Vector field of (a) the maximum horizontal stress and (b) the minimum horizontal stress at a depth of 3051 m. The same stress orientations are observed at all other depths.

8.3 Model accuracy and uncertainties

An important aspect during the development of a 3D geomechanical model is its uncertainties and accuracy. The first source of uncertainty comes from the input data, which, in this case, are the four depth surfaces mapped by TNO. The model from which the surfaces are extracted has a resolution of 250 m, indicating that this model is of sufficient quality to give a regional-scale overview of the Dutch subsurface (NLOG, 2015). Uncertainties in this model have been quantified by constructing so-called uncertainty depth maps in which the uncertainty is displayed by the standard deviation. For the modelled area, Table 11 depicts the standard deviation for four available surfaces of which two (Base Chalk and Rijnland Group) are not included in the actual 3D model. Nevertheless, it clearly shows that with depth the uncertainty in the base of a stratigraphic unit increases. This is a source of uncertainty which will affect the final

simulation result as thickness uncertainties have an impact on the vertical and horizontal stress distribution via the bulk density and Poisson's ratio.

Table 11: Available data on depth uncertainties in the modelled area of Section 8.2 (NLOG, 2015).

Base surface	Standard deviation [m]
Upper North Sea Group	± 10.06
Base Chalk Group	± 43.50
Base Rijnland Group	± 43.65
Base Lower Germanic Trias Group	± 60.90

Another source of uncertainty results from the way in which the 3D geomechanical model is developed. In Section 8.1, it has been shown that the stratigraphic units between the base Upper North Sea and top Zechstein have been merged to reduce model complexity and computation time. However, simplifying the overlying stratigraphy and using average rock and elastic properties for the overburden has consequences for the vertical and horizontal stresses in the underlying formations.

Finally, the mesh size plays an important role in the accuracy and thus overall quality of the 3D geomechanical model. The density of the mesh is specified by defining the number of nodes on each edge of a surface. In this model, 25 nodes have been assigned to each edge of a surface but this results in an irregular mesh along certain parts of the edges if the node spacing is not entirely constant. This can be resolved by increasing the number of nodes on an edge, however, for this model, 25 nodes are the maximum as more nodes will result in a simulation case with a too large number of elements. In turn, this leads to a significant increase in the computation time due to the lack of sufficient CPU capacity. A solution would be the availability of a remote server as it provides considerably more capacity and thus offers opportunities for densely meshed models in advanced geomechanical simulations.

9. Discussion

9.1 Overall horizontal stress orientations

The 86 new boreholes that have been added to the DSM database is a relatively small amount compared to the total number of boreholes analysed. However, it must be taken into account that in each well multiple S_H orientations with depth have been gathered. As such, the stratigraphic extent of the horizontal stress field has been explored for the first time in the Netherlands.

In terms of the S_H orientations per stratigraphic unit, the more N-S orientations in the Chalk and Scruff Group do not follow the rather consistent S_H direction of $315^\circ \pm 22.5^\circ$ in the other stratigraphies. However, in these two units, only one (Chalk Group) and seven (Scruff Group) data points have been obtained, which are influenced by local structural features and therefore do not give a reliable indication of the regional S_H orientation. When comparing the DSM database with break-out studies in adjacent areas, a similar consistent dataset with depth has been collected by Williams et al. (2015) in the UK southern North Sea. As in the Dutch Stress Map, the majority of the data displays a NW-SE S_H orientation with some deviations in the Cenozoic and Zechstein units. In contrast, the Danish Central Graben is characterized by S_H orientations that differ considerably between the various stratigraphic groups (Ask, 1997).

The S_H orientations in the post-salt stratigraphies indicate a larger degree of variation compared to the pre-salt stratigraphies. It is suggested that this scatter is related to the Zechstein formation, which partly acts as a stress detachment as it can be described as mechanically weak (Ask, 1997; Bell, 1996). The stress field prevailing in the post-salt units will therefore be no longer completely influenced by the stresses in the pre-salt stratigraphic groups. Consequently, local stresses can dominate in the post-salt stratigraphies (Ask, 1997). However, as noted by Williams et al. (2015), it remains questionable to what extent the Zechstein unit exactly influences the overlying stress field, also because it does not cover the entire Dutch on- and offshore.

Studies have shown that in deviated wells, the relation between stress-induced borehole features and the S_H orientation is no longer straightforward. However, the majority of the stress data in the deviated wells of the DSM database still indicate a NW-SE S_H orientation. Mastin (1988) studied the relation between wellbore deviation angles and break-out orientation by using an elastic analytical solution in the three stress regimes. In a normal faulting regime, the deviation angle required to rotate break-outs more than 10° from S_h becomes zero when the ratio between S_H and S_h approaches one. This theory therefore suggests that in the Netherlands the S_H/S_h ratio is clearly larger than one, as deviated wells with angles between 10° and 40° are still able to indicate a NW-SE S_H orientation.

9.2 Local stress deviations in the Dutch Stress Map

The case studies show that significant deflections from the regional NW-SE S_H trend can be observed near the salt structure and normal fault. It is most likely that the S_H deflections are caused by these local features, however, when comparing the S_H orientations with the expected S_H trajectories described in literature, they do not fully match.

In the salt structure case, most maximum horizontal stress directions are not oriented perpendicular to the interface between the salt structure and the surrounding sediment. This mismatch is probably caused by the fact that it is not straightforward to accurately indicate the salt-sediment interface on the horizontal depth slices. As such, it is difficult to state whether the S_H measurement is actually oriented perpendicular to the salt structure.

With respect to the case of the normal fault, it is proposed that the S_H trajectories have rotated perpendicular to the fault plane due to a difference in mechanical properties between the fault and the host rock. However, this remains highly questionable as no information is available about the mechanical properties of the fault. In addition, it does not explain the observation that the shallowest two break-outs have not been deflected from the regional NW-SE S_H trend. These two break-outs are not situated at a much larger distance to the fault than the underlying break-outs, which indicate a N-S S_H direction.

These case studies only give a limited insight in the effect of local discontinuities on the stress field, as the lack of additional stress data in the immediate surroundings of the structural features, hinders a detailed analysis (Reynolds & Hillis, 2000). In the base case, the consistent S_H orientation with depth has only been shown in the pre-salt stratigraphies, and therefore, it is uncertain whether this uniform S_H direction is also present in the post-salt groups. On the other hand, it remains unclear how the stress field behaves at other positions around the salt structure and normal fault, as these areas could not be investigated.

9.3 In-situ stress regimes in the northeast of the Netherlands

Even though the models are only applicable for the stratigraphy of well ZRP-01 and a hydrostatic pore pressure gradient, they give a good indication of the sensitivity of the in-situ stress regime to different boundary conditions. The models all indicate a normal faulting regime at reservoir depth and deeper, however, in the overlying formations up to Earth's surface, no unambiguous stress regime can be identified when comparing the models.

In these overlying formations, it is thought that the stress profiles of gravity-only Model 2 give an accurate indication of the in-situ stress conditions. The constant ESR in the equations of S_h and S_H has been selected based on in-stress magnitudes derived from direct and indirect stress measurements. Moreover, the resulting stress profiles identify a normal faulting stress regime in the overlying formations, which, in turn, corresponds with the experiences gathered from drilling in the Groningen field (Y, XXXX). However, the fact that a different ESR is selected for the equations of S_h and S_H , means that in the horizontal plane an anisotropy exists in the Poisson's ratio, which cannot be explained.

Although Model 3 rarely differs from Model 2 and thus also identifies a normal faulting regime at all depths, it is thought to be relatively less accurate in terms of the stress magnitudes. The different geomechanical properties of the Zechstein have not been taken into account and also, it is unknown what data the S_h gradient of 1.6 bar/10m is based on. Besides that, the amount of data used for the derivation of the maximum horizontal stress is limited.

On the other hand, the gravity-tectonic and tectonic strain models (4 and 5) are based on a constant tectonic stress and strain magnitude with depth, which has not been derived from in-situ stress data. As

such, it is difficult to validate these models, also because in-situ stresses are rarely quantified in the shallow subsurface. Therefore, it cannot be verified whether one of the horizontal stresses (or both) is indeed larger than the vertical stress in the interval between the reservoir and Earth's surface.

9.4 3D Geomechanical modelling

Although the gravity-only case is a useful example to describe the workflow for developing a 3D geomechanical model, the added value of the simulation output is limited. The presence of smaller and larger salt structures has only a marginal influence on the in-situ stress distributions. Moreover, no comparison can be made between the horizontal stress orientations of the simulation output and the in-situ stress data collected in the area. These observations suggest that additional features, such as faults, salt creep and shear stresses need to be incorporated to increase the model complexity and the added value of the simulation output.

10. Conclusions

The Dutch Stress Map database has been expanded with horizontal stress data for 86 new boreholes in addition to the 45 wells that are currently included in the WSM dataset. These new boreholes are mainly collected in the central area of the Dutch North Sea and the Groningen and Drenthe province. For the first time in the Netherlands, it is possible to analyse the horizontal stress directions with depth due to the significant increase in the amount of data.

The Dutch Stress Map demonstrates that the majority of the break-outs, drilling-induced fractures and acoustic anisotropy data clearly indicate a NW-SE S_H orientation. This NW-SE trend is not only dominant spatially but also with depth, as most stratigraphies indicate a S_H orientation in the range of $315^\circ \pm 22.5^\circ$. An exception are the data points in the Chalk and Scruff Group, as they indicate more N-S S_H orientations. When comparing the horizontal stress directions in the pre- and post-salt stratigraphies, no significant change in S_H orientation is observed. However, the stress data in the post-salt stratigraphies does show a larger degree of variation, which could be related to the presence of a stress detachment. The S_H directions in the deviated wells of the DSM database have not been deflected considerably from the regional NW-SE trend. This indicates that the deviation angle has had a limited effect on the orientation of the stress-induced boreholes features.

In an area without major structural complexity, the base case scenario indicates a consistent NW-SE S_H direction with depth, implying that the regional stress trend is dominant and that paleostresses at the time of deposition do not have an influence on the present-day stress field. On the other hand, the case with the salt structure shows S_H orientations, which deviate significantly from the regional NW-SE S_H trend. However, the influence of the salt structure on the in-situ stress field becomes less towards the crest of the structure. In the horizontal plane, most of the stress directions do not fully correspond with the S_H trajectories around salt structures described in literature. Finally, the third case study illustrates that the N-S S_H directions are oriented perpendicular to the strike of a normal fault. This suggests that the break-outs have been influenced by an inactive normal fault, which is mechanically stiffer than the surrounding host rock.

The 1D in-situ stress models based on the stratigraphy of well ZRP-01, all indicate a normal faulting stress regime at reservoir depth and deeper. In contrast, in the overlying formations up to Earth's surface, gravity-only models 2 and 3 identify a normal faulting regime, whereas the tectonic stress and strain models identify reverse and strike-slip faulting. Model 2 seems to give the most accurate indication of the stress conditions in these overlying formations, as it is based on an extensive in-situ stress dataset and the model aligns with local drilling experience. However, to fully confirm the predicted normal faulting regime and to understand the horizontal anisotropy in the Poisson's ratio, shallow in-situ stress data is needed and this is currently lacking.

A workflow is presented for developing a 3D geomechanical model and for performing a basic gravity-only simulation. The simulation output shows that the salt structures have a limited influence on the in-situ stress distributions and that no rotations in the horizontal stress field are observed. Besides that, the uncertainties and accuracy related to this model have been quantified and discussed.

11. Recommendations

During the processing of the different datasets, stress-induced borehole features could not be identified in a significant number of wells due to poor image and caliper log quality. In order to maximize the data coverage of the DSM database, it is advised to use specialized software (e.g. GMI Geomechanics) to interpret these logs, such that an additional number of wells can be added to the database. Besides that, the software can be used to accurately determine the orientation of S_H in the deviated wells of the DSM database.

The horizontal stress orientations in the post-salt stratigraphies show a larger degree of variation compared to the data in the pre-salt stratigraphies. To better understand whether this can be related to the presence of the Zechstein, the data should be subdivided into different areas as the formation is not present across the entire Dutch on- and offshore regions. In combination with the thickness of the Zechstein in these areas, it can then be studied to what extent the formation acts a stress detachment.

For future work, an extensive study should be performed on the use of break-out widths to determine the magnitude of S_H . The maximum horizontal stress is the most challenging stress component to quantify and so far, only Y (XXXX) used break-outs in the Netherlands to determine the magnitude of S_H in the Groningen field.

In turn, this break-out study can assist in confirming the presence of a normal faulting stress regime in the interval between Earth's surface and the reservoir. To answer this final question, a closer look should be taken at the availability of e.g. leak-off test data and break-outs in this interval, such that the horizontal stress magnitudes can be determined.

References

- Aleksandrowski, P., Inderhaug, O.H., & Knapstad, B. (1992). Tectonic structures and wellbore breakout orientation. In: Proceedings of the 33th U.S. Symposium on Rock Mechanics. Santa Fe, New Mexico, USA, 2-5 June 1992. Alexandria: American Rock Mechanics Association (ARMA).
- Anderson, E.M. (1951). The dynamics of faulting and dyke formation with applications to Britain. (2nd rev. ed.). Edinburgh: Oliver and Boyd.
- Ask, M.V.S. (1997). In situ stress from breakouts in the Danish Sector of the North Sea. Marine and Petroleum Geology (14) (3), 231-243.
- Baker Hughes (2016). User Manual: JewelSuite 6.2 Subsurface Modelling. Delft: Baker Hughes.
- Becker, A., & Davenport, C.A. (2001). Contemporary in situ stress determination at three sites in Scotland and northern England. Journal of Structural Geology 23 (2-3), 407-419.
- Bell, J.S. (1996). Petro Geoscience 2: In situ stresses in sedimentary rocks (Part 2): Applications of stress measurements. Geoscience Canada 23 (3), 135-153.
- Bell, J.S., & Gough, D.I. (1979). Northeast-southwest compressive stress in Alberta: Evidence from oil wells. Earth and Planetary Science Letters 45 (2), 475-482.
- Bertotti, G., De Graaf, S., Bisdorf, K., Oskam, B., Vonhof, H.B., Bezerra, F.H.R., Reijmer, J.J.G., & Cazarin, C. (2017). Fracturing and fluid-flow during post-rift subsidence in carbonates of the Jandaíra Formation, Potiguar Basin, NE Brazil. Basin Research, 1-18.
- Brudy, M., & Kjørholt, H. (2001). Stress orientation on the Norwegian continental shelf derived from borehole failures observed in high resolution borehole imaging logs. Tectonophysics 337 (1-2), 65-84.
- Brudy, M., & Zoback, M.D. (1998). Drilling-induced tensile wall-fractures: implications for determination of in-situ stress orientation and magnitude. International Journal of Rock Mechanics and Mining Sciences 36 (2), 191-215.
- Cowgill, S.M., Meredith, P.G., & Murrell, A.F. (1994). Heterogeneous stress orientations in the North Sea Basin. In: Proceedings of Rock Mechanics in Petroleum Engineering Conference. Delft, The Netherlands, 29-31 August 1994, pp. 963-970. Richardson: Society of Petroleum Engineers (SPE).
- De Bree, P. (1988). Status of the differential strain analysis technique for the prediction of in-situ stress and hydraulic fracture orientation. RKGR.87.158.
- Davis, D.M., & Engelder, T. (1985). The role of salt in fold-and-thrust belts. Tectonophysics 119 (1-4), 67-88.

Davis, T., Warner, M., Elders, C., & Davison, I. (2000). Tertiary faulting patterns and growth history of Central Graben salt diapirs. In: Proceedings of the Canadian Society of Exploration Geophysicists Annual Conference. Calgary: Canadian Society of Exploration Geophysicists (CSEG).

Eaton, B.A. (1969). Fracture gradient prediction and its application in oilfield operations. Journal of Petroleum Technology 21 (10), 1353-1360.

Engelder, T., & Sbar, M.L. (1984). Near-surface in situ stress: introduction. Journal of Geophysical Research 89 (B11), 9321-9322.

Fairhurst, C. (1968). Methods of determining in situ rock stresses at great depths. Technical Report (TRI-68). Omaha, Nebraska: The Division.

Fjaer, E., Holt, R.M., Raaen, A.M., Risnes, R., & Horsrud, P. (2008). Petroleum related rock mechanics. (2nd ed.). Oxford: Elsevier.

Fuchs, K., & Müller, B. (2001). World Stress Map of the Earth: a key to tectonic processes and technological applications. Naturwissenschaften 2001 (88), 357-371.

Gradstein, F.M., Ogg, J.G., Schmitz, M.D., & Ogg, G.M. (2012). The geologic time scale 2012. (1st ed.). Oxford: Elsevier.

Haldorsen, J.B.U., Johnson, D.L., Plona, T., Sinha, B., Valero, H.P., & Winkler K. (2006). Borehole acoustic waves. Oilfield Review 18 (1), 34-43.

Heidari, M., Nikolinakou, M., Flemings, P., & Hudec, M. (2015). A simplified analysis of stresses in rising salt domes and adjacent sediments. In: Proceedings of the 49th U.S. Rock Mechanics/Geomechanics Symposium. San Francisco, California, USA, 28 June – 1 July 2015. Alexandria: American Rock Mechanics Association (ARMA).

Heidbach, O., Barth, A., Müller, B., Reinecker, J., Stephansson, O., Tingay, M., & Zang, A. (Last update 2016a, December). *Scientific Technical Report 16-01* [online: web]. Retrieved February 4, 2017, from http://www.world-stress-map.org/fileadmin/wsm/pdfs/WSM_STR_16_01.pdf

Heidbach, O., Fuchs, K., Müller, B., Wenzel, F., Reinecker, J., Tingay, M., & Sperner, B. (2007). The World Stress Map. Episodes Journal of International Geoscience 30 (3), 197-199.

Heidbach, O., Rajabi, M., Reiter, K., Ziegler, M., & WSM Team. (2016b). World Stress Map Database Release 2016. GFZ Data Services [online: web]. Retrieved December 22, 2017, from <http://dataservices.gfz-potsdam.de/wsm/showshort.php?id=escidoc:1680890>

Heidbach, O., Tingay, M., Barth, A., Reinecker, J., Kurfeß, D., & Müller, B. (2009). Global crustal stress pattern based on the World Stress Map database release 2008. Tectonophysics 482 (1), 3-15.

King, R., Backé, G., Tingay, M., Hillis, R., & Mildren, S. (2012). Stress deflections around salt diapirs in the Gulf of Mexico. Geological Society, London, Special Publications 367 (1), 141-153.

Kingdon, A., Fellgett, M.W., & Williams, J.D.O. (2016). Use of borehole imaging to improve understanding of the in-situ stress orientation of Central and Northern England and its implications for unconventional hydrocarbon resources. Marine and Petroleum Geology 73 (1), 1-20.

Kirsch, G. (1898). Die Theorie der Elastizität und die Bedürfnisse der Festigkeitslehre. Verlin Deutscher Ingenieure 42 (28), 797-807.

Klein, R.J., & Barr, M.V. (1986). Regional state of stress in Western Europe. In: Proceedings of the International Symposium on Rock Stress and Rock Stress Measurements. Stockholm, Sweden, 1-3 September 1986, pp. 33-44. Lisbon: International Society for Rock Mechanics (ISRM).

Mardia, K.V. (1972). Statistics of directional data. In Probability and Mathematical Statistics (p. 357). London: Academic Press.

Mariucci, M.T., Amato, A., Gambini, R., Giorgioni, M., & Montone, P. (2002). Along-depth stress rotations and active faults: An example in a 5-km deep well of southern Italy. Tectonics 21 (4), 3-1 - 3-9.

Mastin, L. (1988). Effect of borehole deviation on breakout orientations. Journal of Geophysical Research 93 (B8), 9187-9195.

Müller, B., Zoback, M.L., Fuchs, K., Mastin, L., Gregersen, S., Pavoni, N., Stephansson, O., & Ljunggren, C. (1992). Regional patterns of tectonic stress in Europe. Journal of Geophysical Research 97 (B8), 11783-11803.

Nederlandse Aardolie Maatschappij B.V. (2013). Technical addendum to the winningsplan Groningen 2013: Subsidence, induced earthquakes and seismic hazard analysis in the Groningen Field. Assen: Nederlandse Aardolie Maatschappij B.V.

NLOG. [online: web] [last updated 2015, March 4]. Retrieved June 17, 2017, from <http://nlog.nl/en/geological-maps>

Prensky, S.E. (1999). Advances in borehole imaging technology and applications. In M.A. Lovell, G. Williamson & P.K. Harvey (Eds), Borehole imaging: applications and case histories. (p. 1-43). London: Geological Society, Special Publications.

Rajabi, M., Tingay, M., King, R., & Heidbach, O. (2017). Present-day stress orientation in the Clarence-Moreton Basin of New South Wales, Australia: a new high density dataset reveals local stress rotations. Basin Research 29 (S1), 622-640.

Reynolds, S.D., & Hillis, R.R. (2000). The in situ stress field of the Perth Basin, Australia. Geophysical Research Letters 27 (20), 3421-3424.

Rijksoverheid. [online: web] [last updated 2017, June 19]. Retrieved July 15, 2017, from <https://www.rijksoverheid.nl/actueel/nieuws/2017/06/19/mogelijk-30-van-industriële-warmtevraag-door-ultradiepe-geothermie>

Rondel, H.E., & Everaars, J.S.L. (1993). Spanning in noordoost Nederland: een breakoutanalyse.

Schutjens, P.M.T.M., Snippe, J.R., Mahani, H., Turner, J., & Ita, J. (2012). Production-induced stress change in and above a reservoir pierced by two salt domes: A geomechanical model and its applications. SPE Journal **17** (1), 80-97.

Sperner, B., Müller, B., Heidbach, O., Delvaux, J., Reinecker, J., & Fuchs, K. (2003). Tectonic stress in the Earth's crust: advances in the World Stress Map project. Geological Society, London, Special Publications **212** (1), 101-116.

Teufel, L.W., & Farrell, H. (1990). In situ stress and natural fracture distribution in the Ekofisk Field, North Sea. In: Proceedings of the Third North Sea Chalk Symposium. Copenhagen, Denmark, 11-12 June 1990.

Van Eijs, R. (2015). Neotectonic stresses in the Permian Slochteren Formation of the Groningen Field.

Van Eijs, R., & Dalfts, W. (2004). Borehole observations of maximum horizontal stress orientations in the Dutch upper crust. TNO-NITG – Information 2004 (December), 11-14.

Van Gent, H.W., Back, S., Urai, J.L., Kukla, P.A., & Reicherter, K. (2009). Paleostresses of the Groningen area, the Netherlands – Results of a seismic based structural reconstruction. Tectonophysics **470** (1-2), 147-161.

Vandycke, S. (2002). Palaeostress records in Cretaceous formations in NW Europe: extensional and strike-slip events in relationships with Cretaceous-Tertiary inversion tectonics. Tectonophysics **357** (1-4), 119-136.

Verweij, J.M., Boxem, T.A.P., & Nelskamp, S. (2016). 3D spatial variation in vertical stress in on- and offshore Netherlands; integration of density log measurements and basin modelling results. Marine and Petroleum Geology **78** (1), 870-882.

Williams, J.D.O., Fellgett, M.W., Kingdon, A., & Williamson, J.P. (2015). In-situ stress orientations in the UK Southern North Sea: Regional trends, deviations and detachment of the post-Zechstein stress field. Marine and Petroleum Geology **67** (1), 769-784.

World Stress Map. [online: web] [last updated 2017, January 9]. Retrieved February 18, 2017, from <http://www.world-stress-map.org>

Zoback, M.D. (2010). Reservoir Geomechanics. (Paperback ed.). Cambridge, United Kingdom: Cambridge University Press.

Zoback, M.D., Barton, C.A., Brudy, M., Castillo, D.A., Finkbeiner, T., Grollmund, B.R., Moos, D.B., Peska, P., Ward, C.D., & Wiprut, D.J. (2003). Determination of stress orientation and magnitude in deep wells. International Journal of Rock Mechanics & Mining Sciences 40 (7-8), 1049-1076.

Zoback, M.D., & Gorelick, S.M. (2012). Earthquake triggering and large-scale geologic storage of carbon dioxide. Proceedings of the National Academy of Sciences of the United States of America 109 (26), 10164-10168.

Zoback, M.D., Moos, D., & Mastin, L. (1985). Well bore breakouts and in situ stress. Journal of Geophysical Research 90 (B7), 5523-5530.

Appendix A: World Stress Map project

The WSM is an open-access public database, maintained by the GFZ German Research Centre for Geosciences, and is the result of a collaboration between the industry and academia (World Stress Map, 2017). The industry is not only the main supplier of data for the WSM, it also frequently uses the data during its projects. For example, during the exploration phase of a hydrocarbon project, for borehole stability problems but also for reservoir characterization and management (Fuchs & Müller, 2001). The WSM project is data driven, which implies that it processes all the stress data that meets the requirements of its quality ranking system (Heidbach et al., 2009). As mentioned in Section 4.1.1, this data is subdivided into four categories of stress indicators and a more detailed description of these categories is given below (World Stress Map, 2017):

1. *Earthquake focal mechanisms*

Earthquake focal mechanisms are responsible for most of the horizontal stress data that is available in the WSM dataset. These focal mechanisms are constructed by the analysis of earthquakes from which information about the horizontal stresses in the crust can be derived (Kingdon et al., 2016). Within the WSM dataset a distinction is made between three types of data that can be obtained from earthquake focal mechanisms: Single (FMS), formal inversions (FMF) and average (FMA) focal mechanisms. These three data types differ from each other in terms of their reliability to characterize the regional present-day stresses in the Earth's crust (Heidbach et al., 2016a). In the WSM dataset, most of the stress information is obtained from single focal mechanisms (Heidbach et al., 2009).

Important to note is that this category of stress indicators is the only source of stress data at depths below six kilometres. This is due to the fact that only a limited number of wells in the world are drilled deeper than six kilometres (Heidbach et al., 2007).

2. *Wellbore break-outs and drilling-induced fractures*

In the WSM dataset, break-outs and drilling-induced fractures are responsible for approximately 19% of the stress information worldwide (Heidbach et al., 2016a). More information about the characteristics of these two stress indicators can be found in Section 3.1.

3. *In-situ stress measurements*

Hydraulic fracturing and overcoring are two techniques that can be utilized to determine the in-situ stresses around a borehole. In contrast to the drilling-induced fractures, hydraulic fractures are the result of exerting a pressure on a section of the borehole wall such that it breaks down and a fracture is formed. These fractures always form perpendicular to the least principal stress, which implies that the direction of S_H can be deduced and even the full stress tensor if ideal conditions are present (Heidbach et al., 2007).

The overcoring technique is a method in which a rock specimen with a strain gauge is cored downhole. By removing the core sample from the surrounding rock, deformation of the core will take place, and this will be measured by the strain gauge. The subsurface stresses can then be derived if the elastic rock properties are known (Becker & Davenport, 2001). However, this technique is associated with a number of problems. First of all, topography, excavation and weathering have an impact on the in-situ stress measurements as overcoring is mostly conducted in the vicinity of a free surface. Moreover, this method

is often used to determine the local stress field around the borehole, rather than characterizing the regional present-day stresses (Heidbach et al., 2016a). As a consequence, this stress indicator is not frequently used within the WSM dataset.

4. Young geologic data

In this fourth category, there are two important stress indicators: fault slip analysis and volcanic vent alignments. Within the WSM dataset these two types of geological data can only be used for deriving the direction of S_H when the indicators are of Quaternary age. In the fault slip analysis, slickensides and striae on fault planes are used to determine the orientation of S_H , whereas volcanic vent alignments are similar to hydraulic fractures as they form perpendicular to the least principal stress (Sperner et al., 2003).

In addition to the horizontal stress data, the WSM has also developed quality ranking schemes to enable straightforward comparison between the four categories of stress indicators. Separate ranking systems have been made for break-outs and drilling-induced fractures, implying that a well will receive two quality labels if both break-outs and drilling-induced fractures are encountered (Heidbach et al., 2016). Tables 12 and 13 show that the data will obtain an A- to E-quality label depending on the number of break-outs/drilling-induced fractures, the total length of the features and the standard deviation.

Table 12: WSM quality ranking system for break-outs where s.d. is the standard deviation of the dataset (Heidbach et al., 2016a).

A - Quality	B-Quality	C-Quality	D-Quality	E-Quality
≥ 10 distinct break-out zones and combined length ≥ 100 m in a single well with s.d. ≤ 12°	≥ 6 distinct break-out zones and combined length ≥ 40 m in a single well with s.d. ≤ 20°	≥ 4 distinct break-out zones and combined length ≥ 20 m in a single well with s.d. ≤ 25°	< 4 distinct break-out zones or < 20 m combined length with s.d. ≤ 40°	Wells without reliable break-outs or with s.d. > 40°

Table 13: WSM quality ranking system for drilling-induced fractures (DIFs) (Heidbach et al., 2016a).

A - Quality	B-Quality	C-Quality	D-Quality	E-Quality
≥ 10 distinct DIF zones and combined length ≥ 100 m in a single	≥ 6 distinct DIF zones and combined length ≥ 40 m in a single	≥ 4 distinct DIF zones and combined length ≥ 20 m in a single	< 4 distinct DIF zones or < 20 m combined length with s.d. ≤ 40°	Wells without reliable DIFs or with s.d. > 40°

In Table 14 the horizontal stress data is displayed based on the second category of stress indicators: break-outs and drilling-induced fractures. It comprises data of 45 wells that have been ranked by the WSM with an A- to D-quality label.

Table 14: Dataset of the World Stress Map (Heidbach et al., 2016b).

Well	Measured depth [m]	Stratigraphy	S_H [degrees from North]		Quality ranking
			Break-outs	Drilling-induced fractures	
ASN-01	3400	De Lutte Formation	347		C
CK-01	Undefined	Undefined	328		C
CK-02	Undefined	Undefined	293		C
D12-05-S1	3500	Silverpit Formation		321	D
D15-FA-102	3700	Silverpit Formation	336		D
DE-10	2200	Undefined	315		C
DE-11	2200	Undefined	310		C
DE-12	2200	Undefined	300		C
DVD-02	2800	Z2 Basal Anhydrite Member	344		D
	3000	Z1 Upper Anhydrite Member		334	D
DVZ-01	4100	Z3 Salt Member	315		D
E18-05	4400	Limburg Group	330		C
	4400	Limburg Group		332	D
EVA-01	3300	Undefined	314		D
F03-FB-104	3500	Z1 Lower Claystone Member	313		D
F15-05	2700	Vlieland Claystone Formation	332		D
	3600	Volpriehausen Clay-Siltstone Member		350	B
GRK-13	3300	Ten Boer Member	35		C
GRK-15	3300	Ten Boer Member	36		C
GRK-47	3300	Ten Boer Member	354		D
GRL-01	3600	De Lutte Formation	334		D
GSB-01	3300	Tubbergen Formation	298		D
J-01	Undefined	Undefined	340		C
K06-06	3800	Silverpit Formation	320		C
	3800	Silverpit Formation		319	D
K06-08	3900	Lower Slochteren Member		323	B
K07-10	3200	Ten Boer Member	314		D
K16-05	1800	Vlieland Claystone Formation	323		C
K16-05-S1	2100	Z3 Carbonate Member		322	C
L05-06	4900	Limburg Group	340		D
	4900	Limburg Group		331	D
L05-09	4700	Lower Slochteren Member	330		D
L07-C-02	3600	Main Claystone Member	323		C
L08-12	4200	Silverpit Formation	334		D
	4300	Lower Slochteren Member		335	B
L08-14-S1	4200	Lower Slochteren Member		325	D
L08-15	4700	Lower Slochteren Member	347		C
	4700	Lower Slochteren Member		345	D
L08-P-05-S1	5000	Lower Slochteren Member	327		C
L09-09	3200	Upper Zechstein Salt	315		D
LIVA-01	4140	Undefined	330		D
M07-02	3100	Ten Boer Member	300		D
MID-302	3200	Z3 Carbonate Member		328	D
NOR-35	3500	Limburg Group	351		D
P06-S-01	3000	Detfurth Claystone Member	302		C
	3100	Upper Volpriehausen Sandstone Member		300	B
P09-09	3600	Main Claystone Member	311		B
	3600	Main Claystone Member		318	A
P18-05	2700	Maurits Formation	328		D
Q10-05	2300	Lower Volpriehausen Sandstone Member		322	B
Q16-08	3900	Upper Detfurth Sandstone Member	330		C
	4000	Lower Volpriehausen Sandstone Member		331	C
SGZ-01	2200	Holland Greensand Member	306		C
VRS-401	1200	Ommelanden Formation	290		D
WGD-01	2200	Limburg Group	310		C

Appendix B: Workflow TNO dataset

In this Appendix a more detailed description is given of the workflow to process the data of the 852 wells in the TNO dataset (Figure 47).

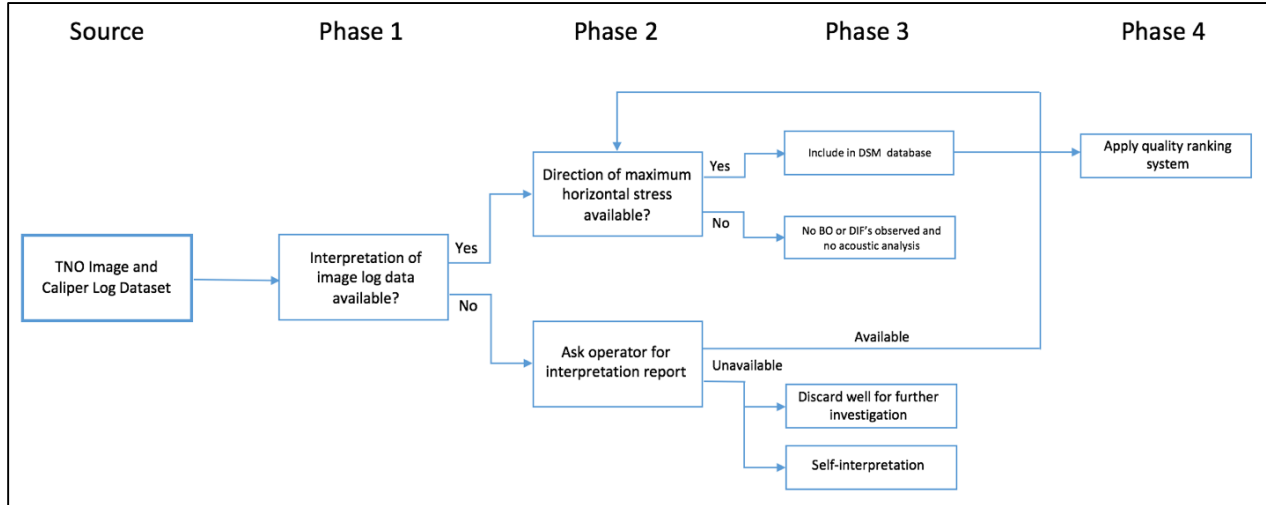


Figure 47: Workflow for processing the TNO dataset. BO = Break-out and DIF = Drilling-induced fracture.

The first step in the workflow is to differentiate between wells of which an interpretation report of the log data is available and wells with not such a report. In the situation where a report is available, the type and amount of stress information differs considerably between the wells. If, on the other hand, no report has been found, it is crucial to note that this does not imply that the operator hasn't conducted such an interpretation. It is still possible that an interpretation has been made, but that it is not available in the public domain. Therefore, additional information should be requested at an operator as it might be stored in its internal database.

In most wells with an interpretation report, the break-out, drilling-induced fracture and/or acoustic anisotropy azimuth is indicated at different depths. An example of such an interpretation report is displayed in Figure 48 where the break-out strike and dip have been interpreted with the use of an OBMI electrical imaging tool. Over the entire interval, it is seen that the break-outs have a fairly constant direction as all break-outs are oriented in a NE-SW direction. Another way in which the data is presented in reports is shown in Figure 49. All break-out directions in the Carboniferous interval of the offshore well K08-12-S1 are visualized with the use of a rose diagram. This rose diagram indicates that most break-outs are encountered between 0 and 30° from the North, which implies that the S_H direction can be found between 270 and 300°. In contrast to these extensive reports, there have also been multiple wells in which only a single direction of S_H is noted for the entire well.

All horizontal stress data that can be extracted from these reports is collected in the Dutch Stress Map (DSM) database, which eventually is processed into maps. The considerable differences in data type and quantity are of importance for the quality ranking of the well, and this is discussed in more detail in Section 4.3. Prior to visualizing the S_H orientations, each well will receive a quality ranking, which is based on the data type and quantity in the well.

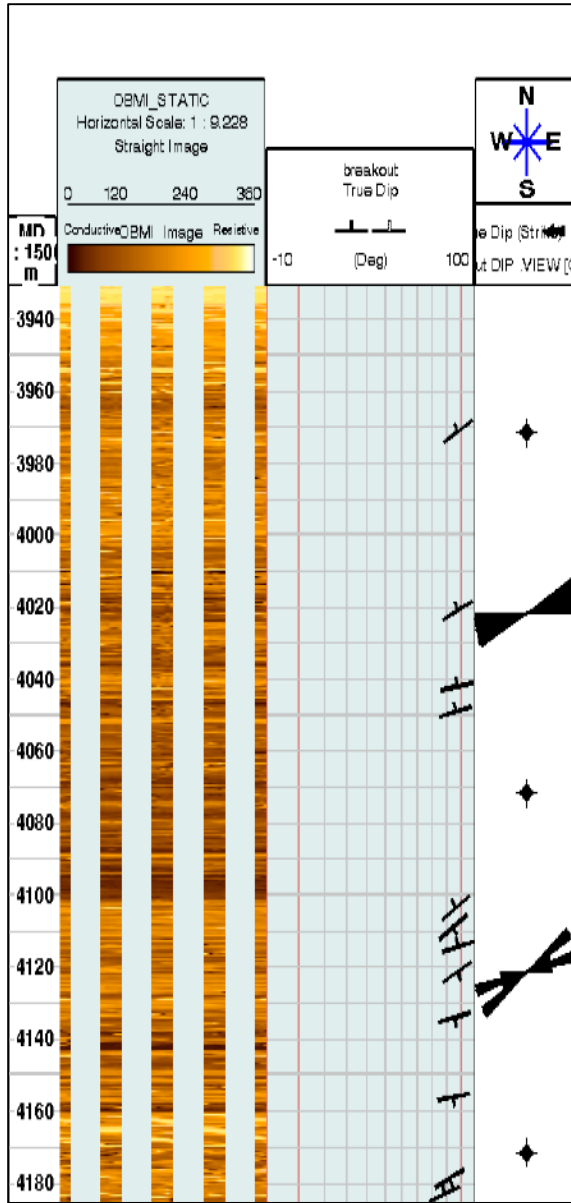


Figure 48: Part of the OBMI log concerning well K12-G-09 in the Dutch offshore field K12-G. The interpreted break-outs are displayed on the centre log and indicate over the entire interval a quite constant NE-SW orientation (source: Appendix H).

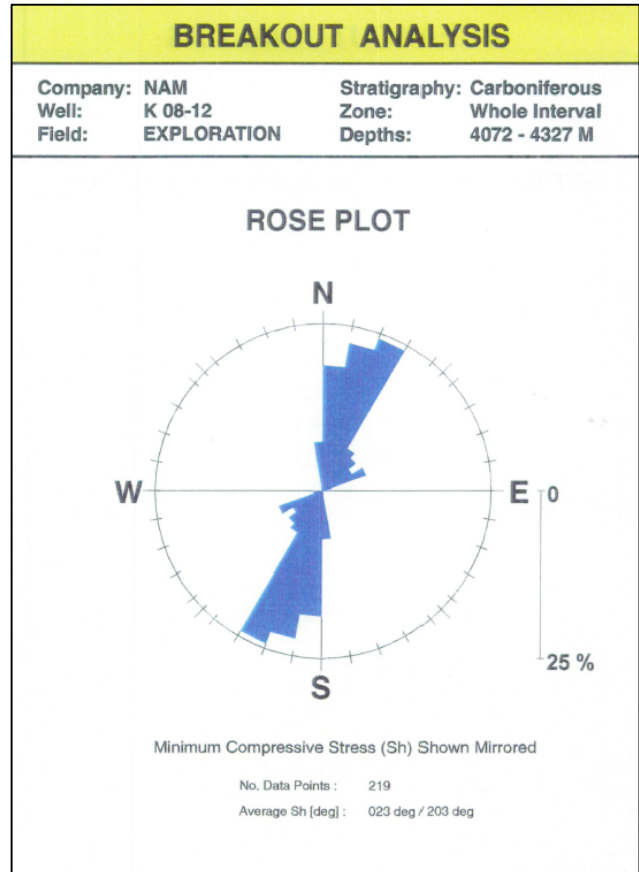


Figure 49: Rose diagram based on the break-outs found in the Carboniferous interval of well K08-12-S1. The majority of the break-outs display a NNO – SSW S_H orientation, which means a WNW – SSE S_H orientation (source: Appendix H).

Appendix C: Dutch Stress Map database

An extensive overview of the stress data that is collected from three different sources (TNO, Rondel & Everaars and Van Eijs) is given in this Appendix.

For the TNO dataset, Section 4.1.2 has indicated that 56 wells contain useful horizontal stress information and in Tables 15 to 23 this data is displayed for each well. Per well it shows the direction of S_H based on either break-outs, drilling-induced fractures and/or acoustic analysis. Besides that, it gives the tool type used and in the majority of the wells the corresponding stratigraphy. In some wells the direction of S_H is given without the depth at which the observation has been done. Hence, no stratigraphy is noted in these wells. The wells highlighted in grey already exist in the WSM dataset, however, they are still included as it results in additional data points with depth. Deviated wells with deviation angles of more than ten degrees are highlighted in red.

Table 15: TNO dataset (source: Appendix H).

Well	Tool type(s)	Measured depth [m]	Stratigraphy	S_H [degrees from North]		
				Break-outs	Drilling-induced fractures	Acoustic analysis
BLF-106	CBIL	Undefined	Undefined	315		
D12-A-02	CBIL & EARTH Imager	3707.8	Silverpit Formation			295
	XMAC-F1	3887.5	Limburg Group	323		
		3923.6	Limburg Group	318		
		3945.6	Limburg Group	306		
		3976.4	Limburg Group	324		
		4019.4	Limburg Group	319		315
		4027.8	Limburg Group	316		
		4039.6	Limburg Group	317		
		4049	Limburg Group	316		
		4065.4	Limburg Group	306		
		4115	Limburg Group	306		
		4124.3	Limburg Group	302		
		4151.6	Limburg Group	298		
D15-05-S1	CBIL & EARTH Imager	3370	Silverpit Formation	315		
E17-A-01	OBMI & UBI	3799.5	Lower Silverpit Claystone Member	332.2		
		3800.2	Lower Silverpit Claystone Member	330		
		4097.3	Hospital Ground Formation	335.7		
E17-A-02	OBMI & UBI	Undefined	Undefined	315		
E17-A-03	OBMI & UBI	3855.4	Hospital Ground Formation	340		
		3862	Hospital Ground Formation	335		
		3882	Hospital Ground Formation	326		
		3909	Hospital Ground Formation	325		
		3954.5	Hospital Ground Formation	336		
E18-03	FMS	4155	Lower Silverpit Claystone Member	305		
		4165	Lower Slochteren Member	305		
		4175	Step Graben Formation	325		
		4185	Step Graben Formation	310		
		4195	Step Graben Formation	325		
		4205	Step Graben Formation	325		
		4215	Hospital Ground Formation	325		
		4225	Hospital Ground Formation	315.5		
		4235	Hospital Ground Formation	325		
		4245	Hospital Ground Formation	325		
		4255	Hospital Ground Formation	335		
		4265	Hospital Ground Formation	325		
		4275	Hospital Ground Formation	330		
		4285	Hospital Ground Formation	345		
		4295	Hospital Ground Formation	335		
		4305	Hospital Ground Formation	335		
		4315	Hospital Ground Formation	330		
		4325	Hospital Ground Formation	330		
		4335	Hospital Ground Formation	335		
		4345	Hospital Ground Formation	335		
		4355	Hospital Ground Formation	335		
		4365	Hospital Ground Formation	325		
		4375	Hospital Ground Formation	325		

Table 16: TNO dataset (source: Appendix H).

Well	Tool type(s)	Measured depth [m]	Stratigraphy	Break-outs	S _H [degrees from North]		
					Drilling-induced fractures	Acoustic analysis	
E18-03		4385	Hospital Ground Formation	330			
		4395	Hospital Ground Formation	335			
		4405	Hospital Ground Formation	335			
		4415	Hospital Ground Formation	341			
		4445	Hospital Ground Formation	320			
		4455	Hospital Ground Formation	325			
		4465	Hospital Ground Formation	325			
		4475	Hospital Ground Formation	345			
		4485	Hospital Ground Formation	345			
		4545	Hospital Ground Formation	345			
		4605	Maurits Formation	355			
		4775	Klaverbank Formation	345			
		4785	Klaverbank Formation	335			
		4805	Klaverbank Formation	335			
		4845	Klaverbank Formation	325			
	E18-05	UBI	4322.5	Limburg Group	325		
			4360.7	Limburg Group	325		
4384.5			Limburg Group	337.5			
4419.5			Limburg Group	327.5			
4422.4			Limburg Group	315			
4436.3			Limburg Group	337.5			
4441.3			Limburg Group	337.5			
4451			Limburg Group	320			
4477.9			Limburg Group	337.5			
4504			Limburg Group	337.5			
4510.3			Limburg Group	327.5			
4515			Limburg Group	330			
4522.9			Limburg Group	325			
4532			Limburg Group	330			
4547.9			Limburg Group	325			
E18-07	EARTH Imager	4645	Silverpit Formation	315	320		
		4670	Silverpit Formation		0		
		4793	Step Graben Formation		335		
		4795	Step Graben Formation	335			
		4880	Step Graben Formation	343	345		
F06-05							
F06-06-S2							
F16-04	FMS	3328.5	Solling Formation	292.5			
F16-05	CBIL & EARTH Imager XMAC-F1	4167	Silverpit Formation	330			
		4198.5	Silverpit Formation		330		
		4212.6	Silverpit Formation			337.5	
		4214	Silverpit Formation	330			
		4222	Silverpit Formation	323			
		4226	Silverpit Formation	330			
		4244	Silverpit Formation	330			
		4262	Lower Slochteren Member	335			
		4265.5	Lower Slochteren Member		330		
		4281	Step Graben Formation	340			
		4309	Step Graben Formation	335			
		4315	Step Graben Formation	335			
		4326	Step Graben Formation		335		
		4332	Step Graben Formation	335			
		4366	Step Graben Formation	337			
		4388	Step Graben Formation	340			
		4390	Step Graben Formation		340		
4410	Hospital Ground Formation	335					

Table 17: TNO dataset (source: Appendix H).

Well	Tool type(s)	Measured depth [m]	Stratigraphy	Break-outs	S _H [degrees from North]			
					Drilling-induced fractures	Acoustic analysis		
F16-05		4417.5	Hospital Ground Formation			335		
		4433	Hospital Ground Formation	337				
		4442.5	Hospital Ground Formation		335			
		4456	Hospital Ground Formation	335				
		4476	Hospital Ground Formation	335				
		4488	Hospital Ground Formation	333				
		4499.5	Hospital Ground Formation			292.5		
		4499.5	Hospital Ground Formation			292.5		
		4511	Hospital Ground Formation	335				
		4542	Hospital Ground Formation	340				
	F16-A-03-S1	CBIL	4766.5	Silverpit Formation			0	
		XMAC-F1	4766.5	Silverpit Formation			22.5	
			4816	Limburg Group	335			
			4817.3	Limburg Group			315	
			4820	Limburg Group	345			
		4824	Limburg Group	335				
		4840	Limburg Group	350				
		4854	Limburg Group	325				
		4864	Limburg Group	340				
GSB-01		SHDT	Undefined	Undefined	315			
K05-12		UBI	3556.3	Silverpit Formation	315			
			3560.9	Silverpit Formation	315			
	3597.8		Silverpit Formation	315				
	3620		Silverpit Formation		320			
	3736.5		Lower Slochteren Member	315				
	3743		Limburg Group	315				
	3747.1		Limburg Group	315				
	3748.1		Limburg Group	315				
	3751.7		Limburg Group	315				
	3761		Limburg Group	315				
	3787.1		Limburg Group	315				
	3806.8		Limburg Group	315				
	3823.5		Limburg Group	315				
	3830.9		Limburg Group	315				
	3839		Limburg Group	315				
	3870.1		Limburg Group	315				
	3870.6		Limburg Group	315				
	3880		Limburg Group		310			
	3889.1		Limburg Group	315				
	3908.1		Limburg Group	315				
	3991.5		Limburg Group	315				
	3992.7		Limburg Group	315				
	K05-ENC-04		OBDT	3633	Silverpit Formation	295		
3648		Silverpit Formation		325				
3672		Silverpit Formation		315				
3722		Silverpit Formation		335				
3748		Silverpit Formation		295				
3922		Lower Slochteren Member		25				
3992.7		Limburg Group		315				
K06-GT-03	OBDT	Undefined	Undefined	325				
		3540	Lower Slochteren Member	345				
K07-09	CBIL	3281	Upper Slochteren Member	305				
K07-10	CBIL	3052.7	Z1 Carbonate Member		310			
		3170.1	Upper Slochteren Member	307				
		3209.8	Ameland Member	307				
		3307.6	Step Graben Formation	315				
		3350.8	Step Graben Formation	337.5				
		3375.3	Step Graben Formation	315				
		3399.2	Step Graben Formation	337.5				
		3438.7	Hospital Ground Formation	315				
		K08-12-S1	CBIL	3695.8	Ameland Member	324		
				4144.9	Hospital Ground Formation	292.5		
				4251.6	Hospital Ground Formation	337.5		
		K09AB-B-02	UBI	4306.2	Maurits Formation	292.5		
4592.6	Upper Slochteren Member			358.6				
4621.3	Upper Slochteren Member			6.2				
4774.8	Lower Slochteren Member			359				

Table 18: TNO dataset (source: Appendix H).

Well	Tool type(s)	Measured depth [m]	Stratigraphy	Break-outs	S _H [degrees from North]			
					Drilling-induced fractures	Acoustic analysis		
K12-G-09	OBMI	3971.5	Upper Slochteren Member	328				
		4021.2	Upper Slochteren Member	333				
		4042.3	Upper Slochteren Member	350				
		4049.5	Upper Slochteren Member	340				
		4103.7	Ameland Member	325				
		4109.2	Ameland Member	325				
		4114.5	Ameland Member	345				
		4121.6	Ameland Member	330				
		4134.2	Ameland Member	355				
		4156.3	Lower Slochteren Member	350				
		4178.9	Lower Slochteren Member	335				
		4183.3	Lower Slochteren Member	335				
		4217.8	Lower Slochteren Member	355				
		4231.5	Lower Slochteren Member	335				
		4242.4	Lower Slochteren Member	335				
		4271.8	Limburg Group	315				
		K16-06-S1	CBIL & STAR Imager XMAC-F1	2561.4	Z3 Carbonate Member			315
				2628.5	Z3 Carbonate Member		325	
				2656	Z3 Carbonate Member		325	
				2757.5	Z2 Salt Member		320	
2773.4	Z2 Salt Member					315		
2863.2	Red-brown Salt Clay Member			335				
2866	Red-brown Salt Clay Member			330				
2895	Z1 Anhydrite Member				315			
2929	Z1 Anhydrite Member				297.5			
2943.9	Z1 Anhydrite Member					315		
2966.5	Z1 Anhydrite Member				320			
3013.9	Z1 Carbonate Member			313				
3014.5	Z1 Carbonate Member			315				
3104.5	Slochteren Formation			292				
3125.9	Slochteren Formation					337.5		
3128.5	Slochteren Formation	312.5						
3137.2	Slochteren Formation	308						
3141.6	Slochteren Formation	305						
K18-08	CBIL & HDIP	3834.5	Upper Slochteren Member	40				
		3851.5	Upper Slochteren Member	70				
		3901	Ameland Member	30				
K18-09								
L05-06	FMS	4875.5	Limburg Group		315			
L05-09	FMS	4726.2	Lower Slochteren Member	315				
		4729.3	Lower Slochteren Member	292.5				
		4731	Lower Slochteren Member	315				
		4738.5	Lower Slochteren Member	315				
		4740.3	Lower Slochteren Member	292.5				
		4745	Lower Slochteren Member	315				
		4748.3	Lower Slochteren Member	315				
		4750.8	Lower Slochteren Member	292.5				
		4752.3	Lower Slochteren Member	315				
		4755.5	Lower Slochteren Member	292.5				
		4758	Lower Slochteren Member	315				
		4761.8	Lower Slochteren Member	315				
		4764.1	Lower Slochteren Member	292.5				
		4764.2	Lower Slochteren Member	315				
		4774.1	Limburg Group	315				
		4777.2	Limburg Group	315				
		4801.8	Limburg Group	315				
		L05-10	CBIL & HDIP	3685	Terschelling Sandstone Member	352.5		
				3735	Friese Front Formation	335		
				3785	Friese Front Formation	337.5		
4523	Lower Slochteren Member			337.5				
4581	Hospital Ground Formation			337.5				
4633	Hospital Ground Formation			337.5				
4801.8	Limburg Group			315				
L05-11	CBIL & STAR Imager	3873	Basal Solling Sandstone Member	355				
		3909	Hardeggen Formation	10				
		3915	Hardeggen Formation	3				
		3921	Hardeggen Formation	347				
		3925	Hardeggen Formation	5				
		3929	Hardeggen Formation	5				
		3934	Hardeggen Formation	345				

Table 19: TNO dataset (source: Appendix H).

Well	Tool type(s)	Measured depth [m]	Stratigraphy	S _H [degrees from North]				
				Break-outs	Drilling-induced fractures	Acoustic analysis		
L05-11		3939	Hardegens Formation	5				
		3961	Lower Detfurth Sandstone Member	345				
		3984	Volpriehausen Clay-Siltstone Member	343				
		4005	Volpriehausen Clay-Siltstone Member	353				
		4009	Volpriehausen Clay-Siltstone Member	350				
		4039	Volpriehausen Clay-Siltstone Member	0				
		4053	Volpriehausen Clay-Siltstone Member	340				
		4059	Volpriehausen Clay-Siltstone Member	336				
		4074	Lower Volpriehausen Sandstone Member	340				
		4104	Rogenstein Member	0				
		4427	Main Claystone Member	347				
		4432	Z2 (Stassfurt) Formation	345				
		4464	Z2 Carbonate Member	348				
		4821	Slochteren Formation	340				
		4826	Slochteren Formation	345				
		4830	Slochteren Formation	342				
		4837	Slochteren Formation	350				
		4847	Slochteren Formation	345				
		4856	Slochteren Formation	340				
		4871	Slochteren Formation	325				
		4878	Slochteren Formation	328				
		4942	Limburg Group	340				
		4947	Limburg Group	340				
		L05-B-02	CBIL & HDIP	4885	Upper Silverpit Claystone Member	340		
				4921	Upper Silverpit Claystone Member	325		
				4928	Lower Slochteren Member	320		
4943	Lower Slochteren Member			320				
4953	Lower Slochteren Member			315				
L05-C-02-S1	CBIL & EARTH Imager XMAC-F1	5008	Limburg Group	297				
		5287	Lower Slochteren Member			0		
		5287	Lower Slochteren Member			315		
L06-06	CBIL & EARTH Imager XMAC-F1	5351	Limburg Group	338				
		5358	Limburg Group	350				
		4984.3	Silverpit Formation			292.5		
		5015	Silverpit Formation			225		
		5381	Lower Slochteren Member	345				
		5387	Lower Slochteren Member	343				
		5413	Lower Slochteren Member	350				
5425.6	Lower Slochteren Member			326.3				
L08-14-S1	FMS	5454	Lower Slochteren Member	345				
		5525	Limburg Group	356				
		4118	Ameland Member	295				
		4124	Ameland Member	297				
		4134	Ameland Member	288				
		4138	Ameland Member	310				
		4140	Ameland Member	300				
		4148	Ameland Member	305				
		4203	Lower Slochteren Member	301				
		4216	Lower Slochteren Member	346				
		4236	Lower Slochteren Member	318				
		4267	Limburg Group	318				
		4288	Limburg Group	340				
		4677	Lower Slochteren Member	348				
		L08-15	FMS	4677	Lower Slochteren Member	348		
4677	Lower Slochteren Member			348				
L08-16-S1	CBIL & EARTH Imager XMAC-F1	3789	Ten Boer Member	320				
		3810	Ten Boer Member	323				
		3998	Ameland Member	338				
		4006	Ameland Member			315		
		4008	Ameland Member	325				
		4036	Lower Slochteren Member	345				
		4054	Lower Slochteren Member	340				
		4057.3	Lower Slochteren Member			315		
		4133	Limburg Group	330				
		4143	Limburg Group	336				
		4146	Limburg Group	335				
		4154	Limburg Group	340				
		4164.5	Limburg Group			337.5		
L08-P-05-S1	UBI	4184	Limburg Group	315				
		4195	Limburg Group	333				
		4957.1	Silverpit Formation	326				
		4965.9	Silverpit Formation	317.4				
		4965.9	Silverpit Formation	317.4				

Table 20: TNO dataset (source: Appendix H).

Well	Tool type(s)	Measured depth [m]	Stratigraphy	Break-outs	S _H [degrees from North]			
					Drilling-induced fractures	Acoustic analysis		
L08-P-05-S1		4967	Silverpit Formation	324				
		4969	Silverpit Formation	331.9				
		4970.2	Silverpit Formation	323.3				
		4978.1	Lower Slochteren Member	328.3				
		4982.9	Lower Slochteren Member	326.5				
		4990.9	Lower Slochteren Member	329.6				
		4994.4	Lower Slochteren Member	321.3				
		4995.1	Lower Slochteren Member	321.5				
		4999.8	Lower Slochteren Member	325.1				
		5003.1	Lower Slochteren Member	322.4				
		5006.1	Lower Slochteren Member	328.9				
		5007.6	Lower Slochteren Member	329.6				
		5012	Lower Slochteren Member		325			
		5017	Lower Slochteren Member		325			
		5024	Lower Slochteren Member		325			
		5030	Lower Slochteren Member		325			
		5075	Lower Slochteren Member		325			
		5082.7	Step Graben Formation	319.1				
		5083.9	Step Graben Formation	311.8				
		5089	Step Graben Formation		325			
		5091	Step Graben Formation		325			
		5092.3	Step Graben Formation	321.4				
		5097.3	Step Graben Formation	322.3				
		5102.4	Step Graben Formation	312.1				
		5105.8	Step Graben Formation	326.3				
		5107	Step Graben Formation	321.6				
		L08-P4-02-S2	UBI	4775	Lower Slochteren Member	330		
				4812.5	Lower Slochteren Member	330		
				4823.5	Lower Slochteren Member	330		
				4829	Lower Slochteren Member	330		
				4837	Lower Slochteren Member	330		
4851	Lower Slochteren Member			330				
4855	Lower Slochteren Member			330				
4859.5	Lower Slochteren Member			330				
4893	Lower Slochteren Member			330				
4906	Limburg Group			330				
4908	Limburg Group			330				
L09-12	CBIL			2953	Main Röt Evaporite Member	316		
				3008.5	Upper Solling Claystone member	314		
				3019.5	Upper Solling Claystone member	358		
		3097	Hardeggen Formation	348				
		3109.3	Detfurth Claystone Member	352				
		3127.9	Detfurth Claystone Member	15				
		3205.9	Volpriehausen Clay-Siltstone Member	10				
L10-33	FMS	3545	Z1 Anhydrite Member		330			
		3552	Z1 Carbonate Member	327				
		3554	Z1 Carbonate Member	320	320			
		3557	Z1 Carbonate Member	323				
		3560	Z1 Carbonate Member	325				
		3564	Ten Boer Member		320			
		3565	Ten Boer Member	315				
		3571	Ten Boer Member	310				
		3576	Ten Boer Member	318				
		3579	Ten Boer Member	317				
		3598	Upper Slochteren Member	300				
		3605	Upper Slochteren Member	319				
		3648	Upper Slochteren Member		290			
		3729	Ameland Member	318				
		3730	Ameland Member		325			
		3732	Ameland Member	332				
		3743	Ameland Member		335			
		3749	Ameland Member	322				
		3750	Ameland Member		332			
		3752	Ameland Member	317				
3763	Lower Slochteren Member		330					
3777	Lower Slochteren Member	345						
3785	Lower Slochteren Member		320					
3792	Lower Slochteren Member		310					
3795	Lower Slochteren Member	315						
L10-M-01	FMS	3840	Upper Slochteren Member	315				

Table 21: TNO dataset (source: Appendix H).

Well	Tool type(s)	Measured depth [m]	Stratigraphy	Break-outs	S _H [degrees from North]	
					Drilling-induced fractures	Acoustic analysis
L14-07	FMS	3190	Upper Slochteren Member		330	
		3289	Upper Slochteren Member		350	
		3303	Ameland Member		327	
		3306	Ameland Member		353	
		3328	Ameland Member		320	
		3335	Ameland Member		325	
		3338	Ameland Member		325	
		3352	Caumer Subgroup		353	
		3368	Caumer Subgroup		350	
		3375	Caumer Subgroup		328	
		3379	Caumer Subgroup		340	
		3384	Caumer Subgroup		313	
		3390	Caumer Subgroup		273	
		3408	Caumer Subgroup		317	
		3417	Caumer Subgroup		316	
		3426	Caumer Subgroup		329	
		3467	Caumer Subgroup		325	
M07-06	CBIL & EARTH Imager	2481	Volpriehausen Clay-Siltstone Member			337.5
	XMAC-F1	2535.5	Lower Volpriehausen Sandstone Member			292.5
P02-NE-02	UBI	2987.1	Z1 Carbonate Member	316.5		
		2991.4	Z1 Carbonate Member	322.6		
		2995.8	Z1 Carbonate Member	308.2		
		3007.6	Slochteren Formation	319.8		
		3008.4	Slochteren Formation	321.9		
		3009.7	Slochteren Formation	318.7		
		3010.9	Slochteren Formation	313.6		
		3013.4	Slochteren Formation	324.5		
		3018.8	Slochteren Formation	307.2		
		3020.1	Slochteren Formation	304.4		
		3052.7	Slochteren Formation	311.9		
		3055.2	Slochteren Formation	303		
		3065.5	Slochteren Formation	300.6		
		3070.9	Slochteren Formation	302.5		
		3071.9	Slochteren Formation	302.1		
		3089.7	Slochteren Formation	309.2		
		3091.2	Slochteren Formation	321		
		3112.8	Slochteren Formation	354.1		
		3138.4	Slochteren Formation	327.1		
		3145.8	Slochteren Formation	335.1		
		3146.9	Slochteren Formation	295.4		
		3151.7	Slochteren Formation	300.9		
		3152.8	Slochteren Formation	297.1		
		3155.2	Slochteren Formation	319.4		
		3156.4	Slochteren Formation	305.8		
		3159.3	Slochteren Formation	293.3		
		3163.7	Slochteren Formation	298.7		
		3165	Slochteren Formation	303.1		
		3177.9	Slochteren Formation	308.1		
		3183.3	Slochteren Formation	301.3		
		3186.6	Slochteren Formation	300.2		
		3213.2	Slochteren Formation	300.4		
		3226.1	Slochteren Formation	299.9		
		3230.3	Slochteren Formation	320.9		
		3231.9	Slochteren Formation	300.8		
		3234.4	Slochteren Formation	245.8		
		3256.5	Slochteren Formation	336		
		3257.4	Slochteren Formation	320.8		
		3258.6	Slochteren Formation	333.5		
		3268.2	Slochteren Formation	323.2		
		3269.4	Slochteren Formation	321.8		
		3278.3	Slochteren Formation	297.7		
		3284.6	Slochteren Formation	303.7		
		3291.7	Slochteren Formation	288.2		
		3297.9	Slochteren Formation	290.9		
		3305	Slochteren Formation	291.9		
		3373	Slochteren Formation	315.7		
		3326.3	Slochteren Formation	309.4		
		3377.1	Slochteren Formation	315.8		
		3386.9	Slochteren Formation	311.9		
		3400.7	Slochteren Formation	306.6		

Table 22: TNO dataset (source: Appendix H).

Well	Tool type(s)	Measured depth [m]	Stratigraphy	Break-outs	S_H [degrees from North]	
					Drilling-induced fractures	Acoustic analysis
P02-NE-02		3404.7	Slochteren Formation	308.5		
		3405.9	Slochteren Formation	310.8		
		3407.3	Slochteren Formation	323		
		3408.5	Slochteren Formation	326.8		
		3410.4	Slochteren Formation	313.3		
		3416.9	Slochteren Formation	311.2		
		3430.3	Limburg Group	325.3		
P06-10	FMI	2935	Lower Muschelkalk Member		295	
P06-D-01	CBIL & STAR	2710	Basal Solling Sandstone Member		325	
		2730	Hardegese Formation	300	310	
		2750	Hardegese Formation	300	310	
		2770	Detfurth Claystone Member	300	305	
		2790	Lower Detfurth Sandstone Member	310		
		2810	Volpriehausen Clay-Siltstone Member	310		
		2830	Volpriehausen Clay-Siltstone Member		295	
		2850	Volpriehausen Clay-Siltstone Member	300	305	
		2910	Lower Volpriehausen Sandstone Member		290	
		2930	Lower Volpriehausen Sandstone Member		295	
		2950	Rogenstein Member		290	
		2970	Rogenstein Member		320	
		3005	Rogenstein Member		310	
		3230	Main Claystone Member		330	
		3250	Zechstein Upper Claystone Formation		315	
		3270	Z3 Carbonate Member		330	320
		3290	Z3 Carbonate Member		330	310
		3310	Z2 Middle Claystone Member		315	318.8
		3325	Z2 Middle Claystone Member		320	
		3510	Slochteren Formation		300	
		3590	Slochteren Formation		320	
		3610	Slochteren Formation		310	
		3650	Slochteren Formation		310	335
		3670	Slochteren Formation		310	
		3690	Slochteren Formation		315	
		3710	Slochteren Formation		310	
		3730	Slochteren Formation		320	
3750	Slochteren Formation		330			
3770	Slochteren Formation		320			
3790	Ruurlo Formation		310	70		
		3804	Ruurlo Formation		305	
P08-07	CBIL & EARTH Imager	2640	Röt Formation	315		
		2652.3	Röt Formation	305		
		2671.3	Röt Formation	305		
		2677.4	Solling Formation	320		
		2716.8	Hardegese Formation	310		
		2722.6	Hardegese Formation	305		
		2745.5	Hardegese Formation	320		
		2790.3	Detfurth Claystone Member	310		
		2793.5	Detfurth Claystone Member	310		
		2807	Detfurth Claystone Member	320		
		3043.2	Lower Bundsandstein Formation	315		
		3048.1	Lower Bundsandstein Formation	305		
		3053.5	Lower Bundsandstein Formation	305		
		3076.1	Lower Bundsandstein Formation	315		
		3084.2	Lower Bundsandstein Formation	320		
		P09-09	FMI	3040.5	Muschelkalk Formation	325
3115.5	Röt Claystone Member			310		
3140.5	Röt Claystone Member			315		
3165.5	Röt Claystone Member			315		
3215.5	Basal Solling Sandstone Member			315		
3265.5	Lower Detfurth Sandstone Member			285		
3365.5	Lower Volpriehausen Sandstone Member			295		
3390.5	Lower Volpriehausen Sandstone Member			305		
3655.5	Main Claystone Member			320		
3680.5	Main Claystone Member			310		
3705.5	Zechstein Upper Claystone Formation			310		
3730.5	Zechstein Upper Claystone Formation			315		
3755.5	Z3 Carbonate Member			315		
3780.5	Z2 Fringe Sandstone Member			305		
3805.5	Z2 Fringe Sandstone Member			305		
3830.5	Red-brown Salt Clay Member			305		

Table 23: TNO dataset (source: Appendix H).

Well	Tool type(s)	Measured depth [m]	Stratigraphy	Break-outs	S _H [degrees from North]			
					Drilling-induced fractures	Acoustic analysis		
P09-09		3855.5	Z1 Fringe Sandstone Member	305				
		3880.5	Z1 Fringe Carbonate Member	305				
		3905.5	Z1 Lower Claystone Member	325				
		3930.5	Z1 Lower Claystone Member	330				
		3955.5	Z1 Lower Claystone Member	315				
		3980.5	Slochteren Formation	315				
		P09-09-S1	FMI	4005.5	Slochteren Formation	315		
				4030.5	Slochteren Formation	315		
				4055.5	Slochteren Formation	310		
				4080.5	Slochteren Formation	310		
4105.5	Slochteren Formation			310				
P18-A-06	UBI	4130.5	Slochteren Formation	330				
		4155.5	Slochteren Formation	330				
		4526	Detfurth Claystone Member		300			
		4551	Detfurth Claystone Member		305			
		4551.9	Detfurth Claystone Member	328.2				
		4584	Lower Detfurth Sandstone Member		295			
		4600	Lower Detfurth Sandstone Member		305			
		4603.3	Volpriehausen Clay-Siltstone Member	321.9				
		4658	Volpriehausen Clay-Siltstone Member		310			
		4677	Lower Volpriehausen Sandstone Member		315			
		4687	Lower Volpriehausen Sandstone Member		323			
		4691	Lower Volpriehausen Sandstone Member		303			
		4700	Lower Volpriehausen Sandstone Member		314			
		4705	Lower Volpriehausen Sandstone Member		304			
		4713	Lower Volpriehausen Sandstone Member		316			
Q01-28	CBIL & EARTH Imager XMAC-F1	4726	Lower Volpriehausen Sandstone Member		322			
		4737	Lower Volpriehausen Sandstone Member		310			
		2905.6	Röt Claystone Member	341				
		2905.7	Röt Claystone Member	333				
		2905.9	Röt Claystone Member	338				
		2906.1	Röt Claystone Member	341				
		2906.4	Röt Claystone Member	351				
		2906.8	Röt Claystone Member	351				
		2907	Röt Claystone Member	0				
		2907.2	Röt Claystone Member	31				
		2907.6	Röt Claystone Member	3				
		2907.9	Röt Claystone Member	331				
		2908.1	Röt Claystone Member	354				
		2908.4	Röt Claystone Member	332				
		2915.3	Röt Formation			315		
		2988.3	Solling Formation			315		
		3022.3	Detfurth Formation			315		
		3046.3	Volpriehausen Clay-Siltstone Member		342			
		3111.8	Volpriehausen Formation			315		
		3225.3	Rogenstein Member	302				
3225.8	Rogenstein Member	342						
3226	Rogenstein Member	345						
3226.3	Rogenstein Member	333						
3226.6	Rogenstein Member	336						
3227.2	Rogenstein Member	315						
3227.6	Rogenstein Member	308						
3292.5	Lower Buntsandstein Formation			337.5				
3293	Main Claystone Member		343					
Q04-08	FMI	2511	Volpriehausen Clay-Siltstone Member	292.5				
Q13-07-S2	CBIL	3225	Volpriehausen Clay-Siltstone Member		322.5			
Q13-12	OBMI & UBI	1868.5	Rijswijk Member	306				
		1892.2	Rodenrijs Claystone Member	280				
		1984.8	Alblasserdam Member	311				
		2160.5	Alblasserdam Member	288.7				

In the research of Rondel and Everaars (1993), 42 wells were analysed and Tables 24 and 25 indicate for most wells the depth of the horizontal stress measurement, as well as the corresponding stratigraphy. The wells that are highlighted in red have either not observed break-outs, the deviation angle of the well is too large ($> 10^\circ$) or the deviation azimuth is used to derive the direction of S_H .

Table 24: Dataset of Rondel and Everaars (1993).

Well	Measured depth [m]	Stratigraphy	S_H [degrees from North]
AMR-01			
AMR-08	2945	Slochteren Formation	310
ANN-03			
ANV-03	1552.5	Upper Holland Marl Member	340
BIR-13			
BHM-02	3853	Tubbergen Formation	320
COV-13	3600	Maurits Formation	300
COV-17			
COV-31	2550	De Lutte Formation	75
COV-33			
COV-41	3230.3	Tubbergen Formation	295
COV-51	2905	Tubbergen Formation	45
	2920	Tubbergen Formation	315
	2940	Tubbergen Formation	45
	3000	Tubbergen Formation	315
CLD-01	2787.5	Tubbergen Formation	320
DAL-04	3200	Tubbergen Formation	300
	3200	Tubbergen Formation	30
DAL-14			
DVD-01			
ESV-01	1749.8	Lower Holland Marl Member	335
	2123.3	Ruurlo Formation	355
EMM-12			
EMM-13			
EMC-01	Undefined	Undefined	345
GSV-01			
GLH-01	3200	Ruurlo Formation	325
	3650	Ruurlo Formation	305
HLE-01	1700.8	Ruurlo Formation	330
	1730.5	Ruurlo Formation	355
HRS-02			
HGL-01	1832.5	Lower Zechstein Salt	285
	1832.5	Lower Zechstein Salt	280
KOL-01	2985	Z2 Carbonate Member	50
	2997.5	Z1 Anhydrite Member	50
	3003	Z1 Anhydrite Member	345
	3061.8	Ten Boer Member	345
	3061.8	Ten Boer Member	75
	3205	Ameland Member	75

Table 25: Dataset of Rondel and Everaars (1993).

Well	Measured depth [m]	Stratigraphy	S_H [degrees from North]
KPD-04			
MKN-01	1615	Upper Holland Marl Member	320
	1700	Slochteren Formation	320
MDN-01			
MNG-01			
RSW-06	1996	Upper Röt Claystone Member	297.5
	1996	Upper Röt Claystone Member	30
SML-01			
STK-01	2150	Upper Muschelkalk Member	330
	2425	Upper Röt Claystone Member	330
TUB-09	Undefined	Undefined	297.5
VRS-05			
WAV-09	1349.3	Main Claystone Member	320
	1392.5	Main Claystone Member	320
WYK-26	1162.5	Lower Holland Marl Member	335
WSM-01			
WSK-01	4233.3	Geverik Member	45
ZND-04			
ZVH-01			
ZBR-01	2801	Ruurlo Formation	35

Table 26 displays the dataset of Van Eijs (2015) in which a distinction is made between directions of S_H based on break-outs, drilling-induced fractures or acoustic analysis. In all wells the measured depth and corresponding stratigraphy are stated, except for the break-out measurement in well NRZ-01.

Table 26: Dataset of Van Eijs (2015).

Well	Tool type(s)	Measured depth [m]	Stratigraphy	S_H [degrees from North]	
				Break-outs	Drilling-induced fractures Acoustic analysis
BTA-01	Four-arm caliper	3070	Rogenstein Member	270	
BRW-05					
KWR-01-S1	Acoustic Scanning tool	3304.4	Slochteren Formation	336	
		3454	Limburg Group	336	
		3468	Limburg Group	336	
NRZ-01	Four-arm caliper	Undefined	Undefined	300	
RDW-01	Acoustic Scanning tool	3273.7	Slochteren Formation	340	
		3276.5	Slochteren Formation	340	
		3278.5	Slochteren Formation	340	
		3380.8	Limburg Group	340	
		3387.5	Limburg Group	340	
ZRP-02					
ZRP-03-S1					

Appendix D: Quality ranking system

For the three datasets (TNO, Rondel & Everaars and Van Eijs) a quality ranking system has been developed, which is less restrictive and therefore a better distribution can be obtained among the five quality classes. In contrast to the WSM system, one quality ranking system has been made for both break-outs and drilling-induced fractures. These two stress indicators have been combined as the presence of both will make the S_H direction in a well more reliable (Williams et al., 2015). In other words, the orientation of S_H will be less reliable when it is solely based on break-outs or drilling-induced fractures and this is reflected in the quality ranking system.

As noted in Section 4.3, the difference between the five quality classes is only based on the number of break-outs and/or drilling-induced fractures in one well (Table 27). The combined length of the stress indicators and the standard deviation have not been included, as for the first parameter crucial data is lacking in most reports. For the latter, no relation has been found between the number of break-outs or drilling-induced fractures in a well and the standard deviation. No decrease in the standard deviation has been observed when the number of data points in a well increase and therefore it has not been incorporated in the quality ranking system of Table 27.

Table 27: Quality ranking system for break-outs and drilling-induced fractures in a well. For the B- to D-quality labels, multiple conditions are stated but a borehole needs to satisfy only one of these conditions.

A - Quality	B-Quality	C-Quality	D-Quality	E-Quality
More than 10 break-outs and more than 10 DIF's	More than 10 break-outs and less than 10 DIF's	More than 10 break-outs and no DIF's	Less than 10 break-outs and no DIF's	No break-outs and DIF's
	Less than 10 break-outs and more than 10 DIF's	No break-outs and more than 10 DIF's	No break-outs and less than 10 DIF's	
	Less than 10 break-outs and less than 10 DIF's			

A separate quality ranking system has been made for the wells in which an acoustic anisotropy analysis has been performed. This implies that some wells obtain two quality labels when both stress-induced borehole features and an acoustic anisotropy have been identified. Table 28 shows the quality ranking system based on the uncertainty in the S_H direction, which is derived from the acoustic analysis.

Table 28: Quality ranking system for wells in which an acoustic analysis has been performed. The quality label depends on the degree of uncertainty in the S_H orientation.

A-Quality	B-Quality	C-Quality	D-Quality	E-Quality
0 - 5°	5 - 10°	10 - 15°	15 - 20°	20 - 25°












In Table 29 an overview is given of the quality labels of all new (sub)-vertical boreholes that are added to the DSM database. With respect to the acoustic analysis data, it can be seen that all wells have either an uncertainty which falls in the C- or E-quality category. This is due to the fact that the XMAC-F1 tool and Sonic Scanner in most cases indicate the direction of S_H as NNW-SSE or WNW-ESE, which implies an uncertainty of 11.25° (C-quality). An E-quality label is assigned to the data when the horizontal stress direction has an uncertainty of 22.5° , which is the case when the S_H direction is given as NW-SE.

Table 29: List of quality labels for the 61 (sub)-vertical wells. The quality ranking is based on stress-induced borehole features and/or acoustic analysis.

Quality ranking			Quality ranking		
Well	BO & DIF	Acoustic analysis	Well	BO & DIF	Acoustic analysis
E17-A-02	E		M07-06	E	C
E17-A-03	D		P08-07	C	
E18-05	C		P09-09	C	
F06-05			P09-09-S1	D	
F06-06-S2			Q04-08	D	
F16-04	D		AMR-08	D	
			ANV-03	D	
GSB-01	E		BHM-02	D	
K05-12	A		COV-13	D	
K05-ENC-04	D		COV-31	D	
K07-09	C		COV-51	D	
K07-10	C		CLD-01	D	
K07-FB-101	B		ESV-01	D	
K08-12-S1	C		EMC-01	D	
K09AB-B-02	D		GLH-01	D	
K12-G-09	C		HLE-01	D	
K16-06-S1	B	C	HGL-01	D	
K18-08	D		MKN-01	D	
K18-09			TUB-09	D	
L05-06	D		WAV-09	D	
L05-09	C		WYK-26	D	
L05-10	D		WSK-01	D	
L05-11	B		ZBR-01	D	
L05-B-02	D		BTA-01	D	
L06-06	D	E	BRW-05		
L08-14-S1	B		KWR-01-S1	D	
L08-16-S1	C	C	NRZ-01	D	
L09-12	D		RDW-01	D	
L10-33	A		ZRP-02		
L10-M-01	D		ZRP-03-S1		
L14-07	B				

Appendix E: Dutch Stress Maps

Table 30: Colour coding system for the different stratigraphies (Gradstein et al., 2012).

Stratigraphic group	Colour
Chalk Group	
Rijnland Group	
Scruff Group	
Schieland Group	
Upper Germanic Trias Group	
Lower Germanic Trias Group	
Zechstein	
Rotliegend	
Limburg Group	
Confidential	
Undefined	

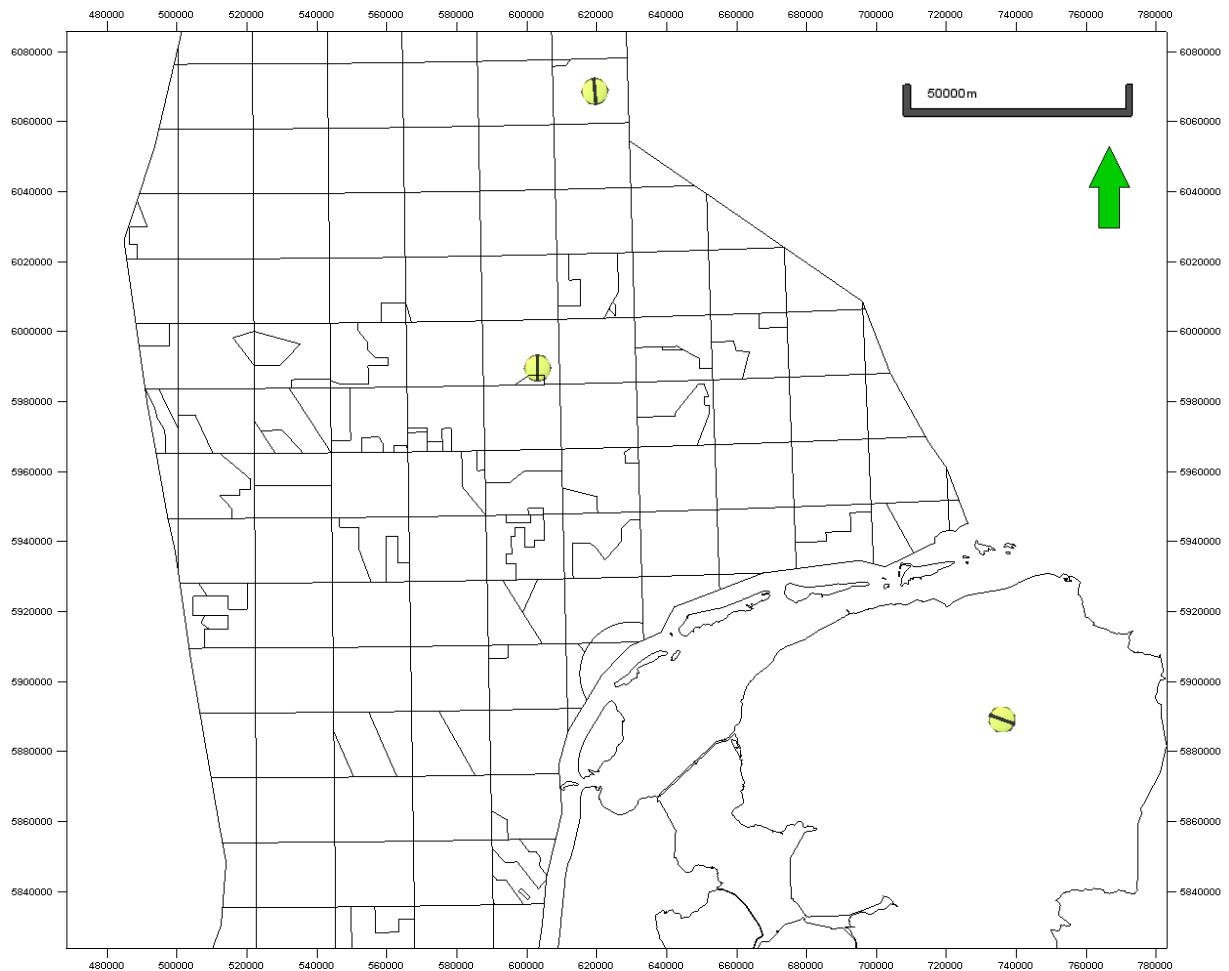


Figure 50: Dutch Stress Map indicating for each well the average S_H direction in the Chalk Group.

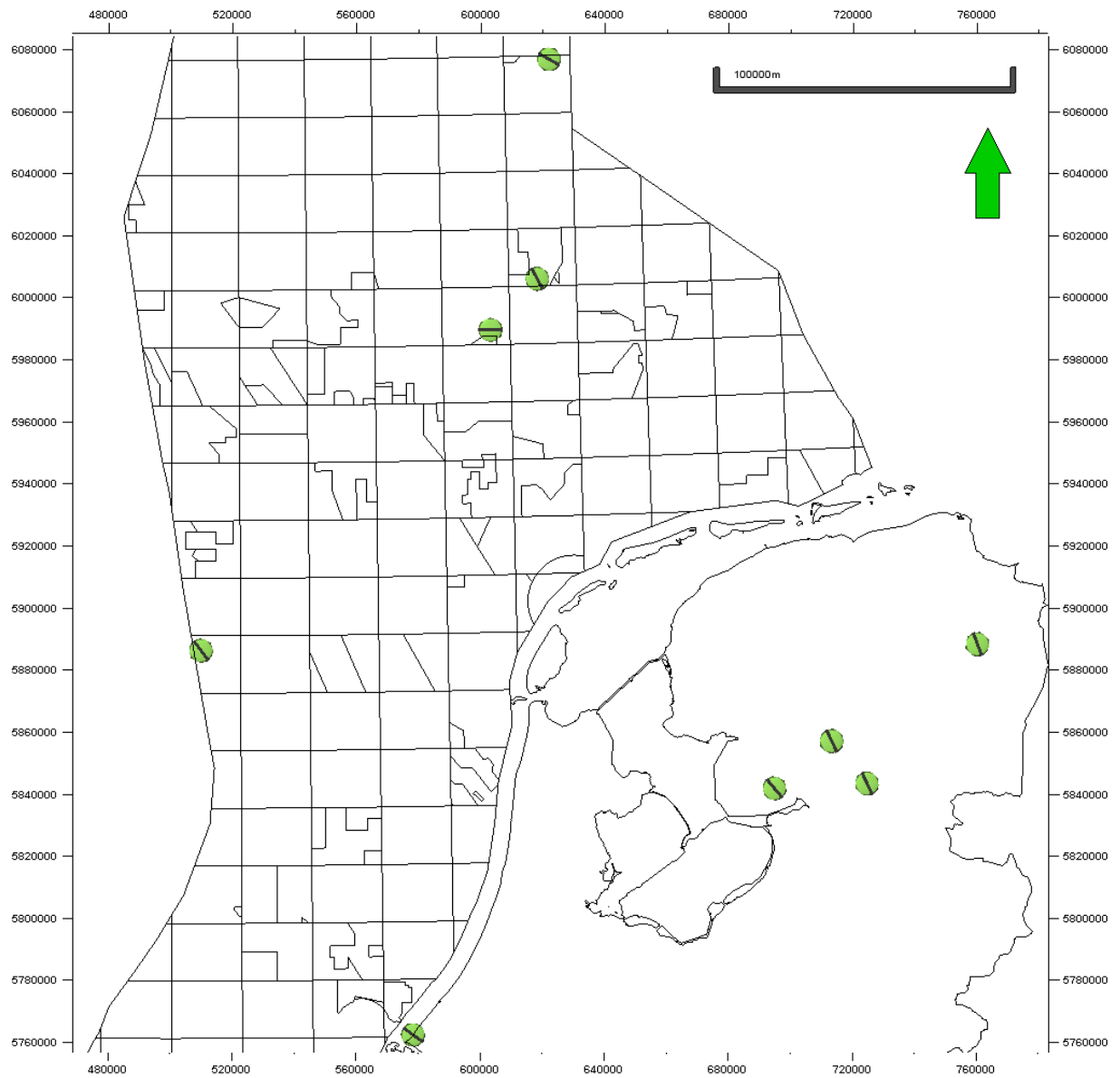


Figure 51: Dutch Stress Map indicating for each well the average S_H direction in the Rijnland Group.



Figure 52: Dutch Stress Map indicating for one well the average S_H direction in the Scruff Group.



Figure 53: Dutch Stress Map indicating for one well the average S_H direction in the Schieland Group.

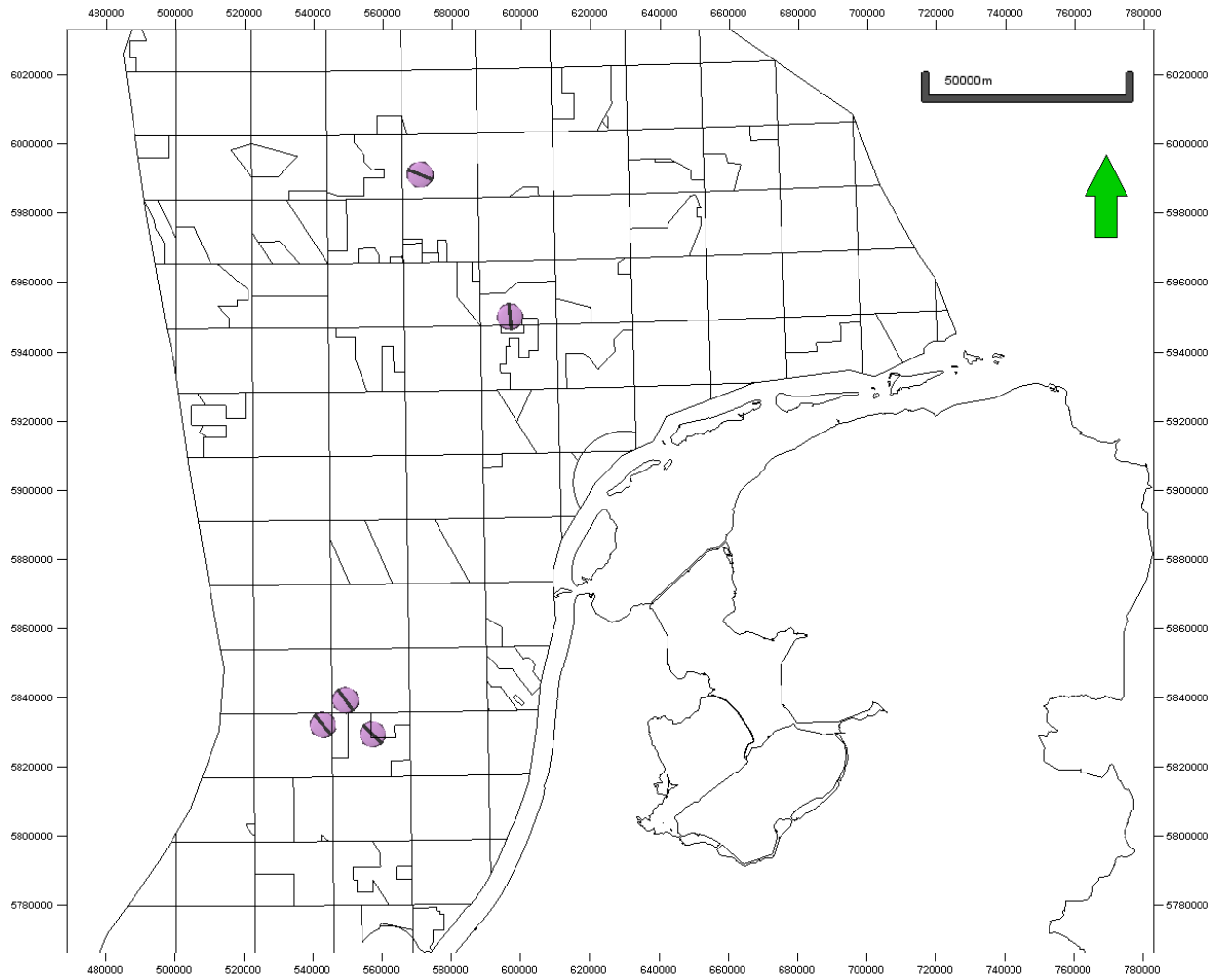


Figure 54: Dutch Stress Map indicating for each well the average S_H direction in the Upper Germanic Trias Group.



Figure 55: Dutch Stress Map indicating for each well the average S_H direction in the Lower Germanic Trias Group.

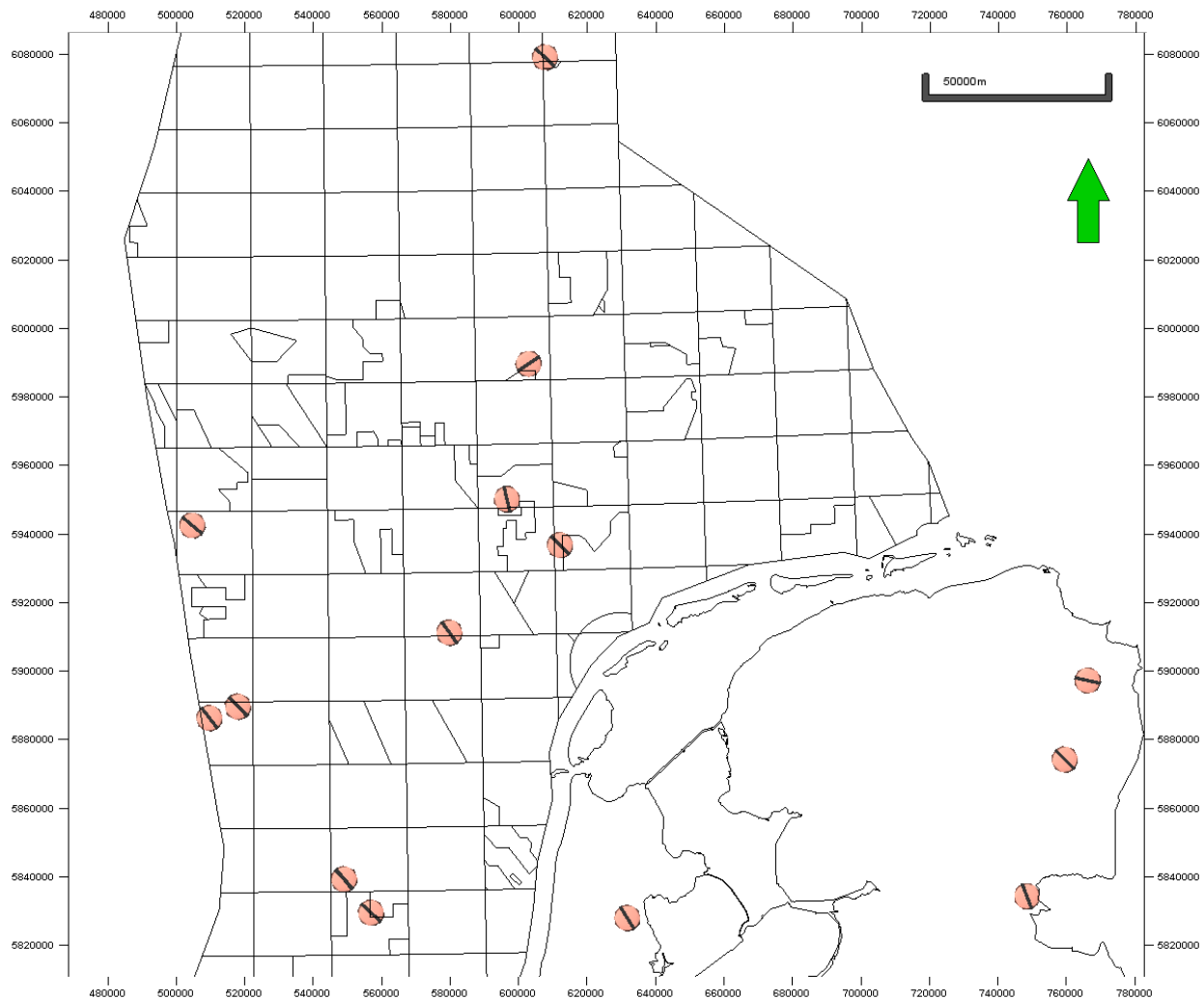


Figure 56: Dutch Stress Map indicating for each well the average S_H direction in the Zechstein.

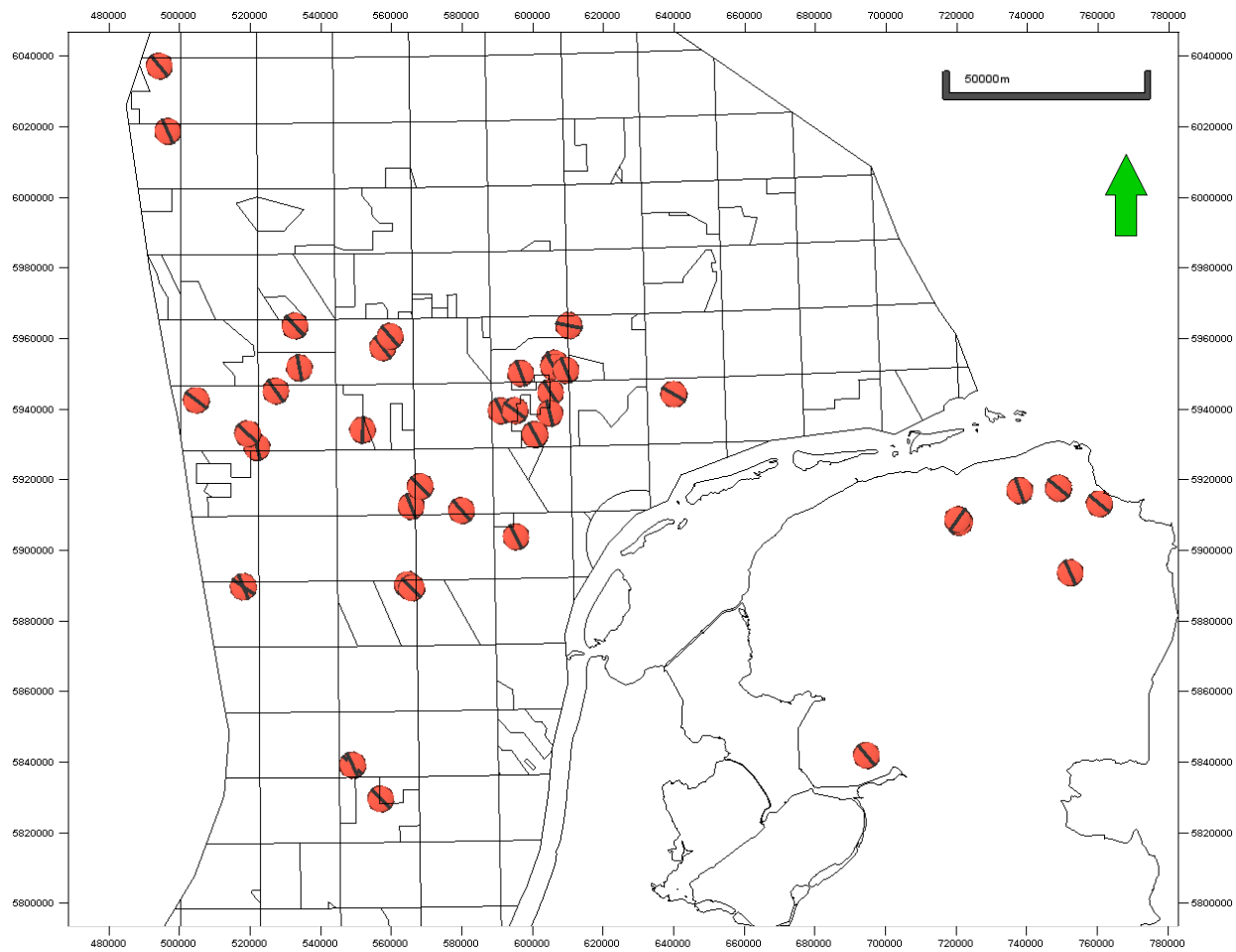


Figure 57: Dutch Stress Map indicating for each well the average S_H direction in the Rotliegend.

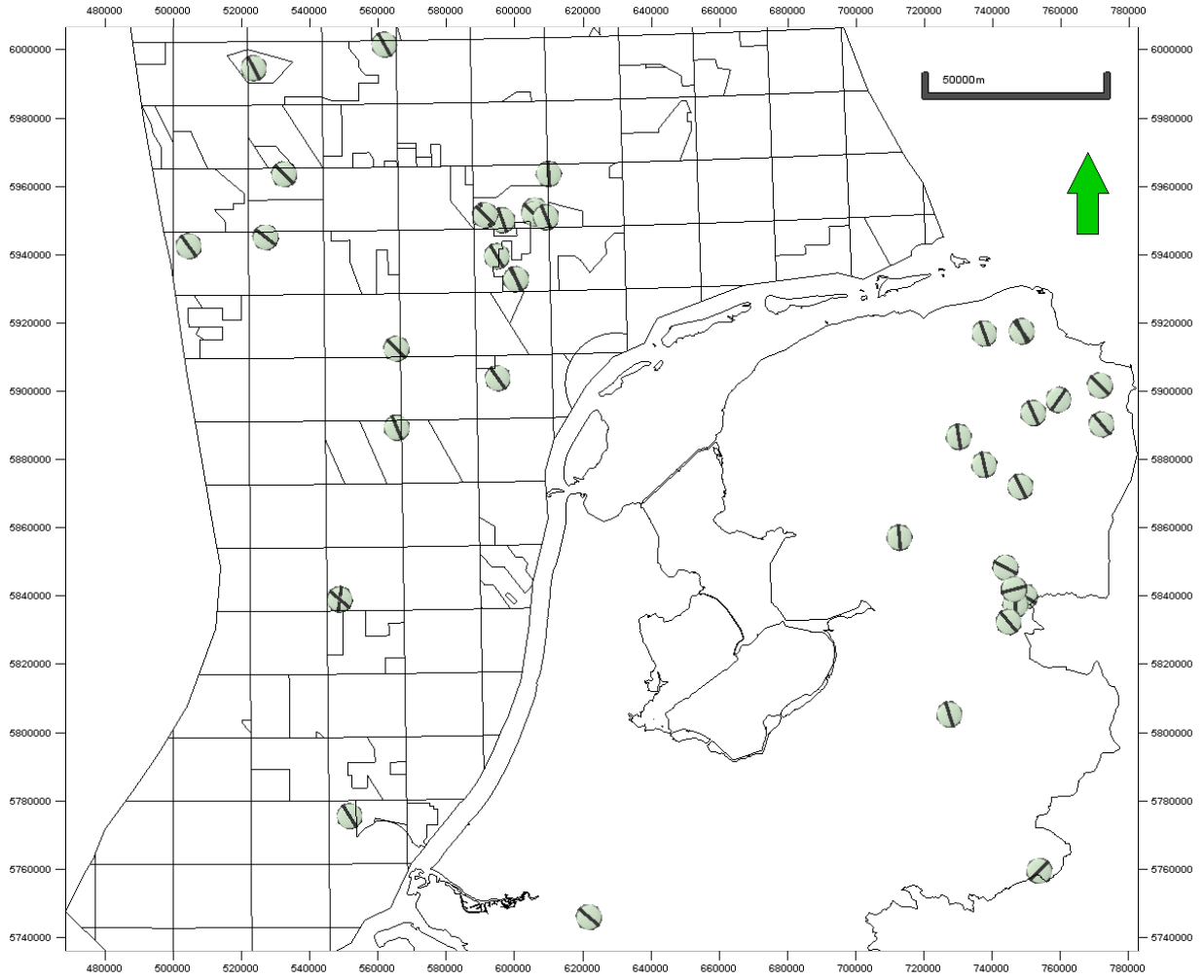


Figure 58: Dutch Stress Map indicating for each well the average S_H direction in the Limburg Group.

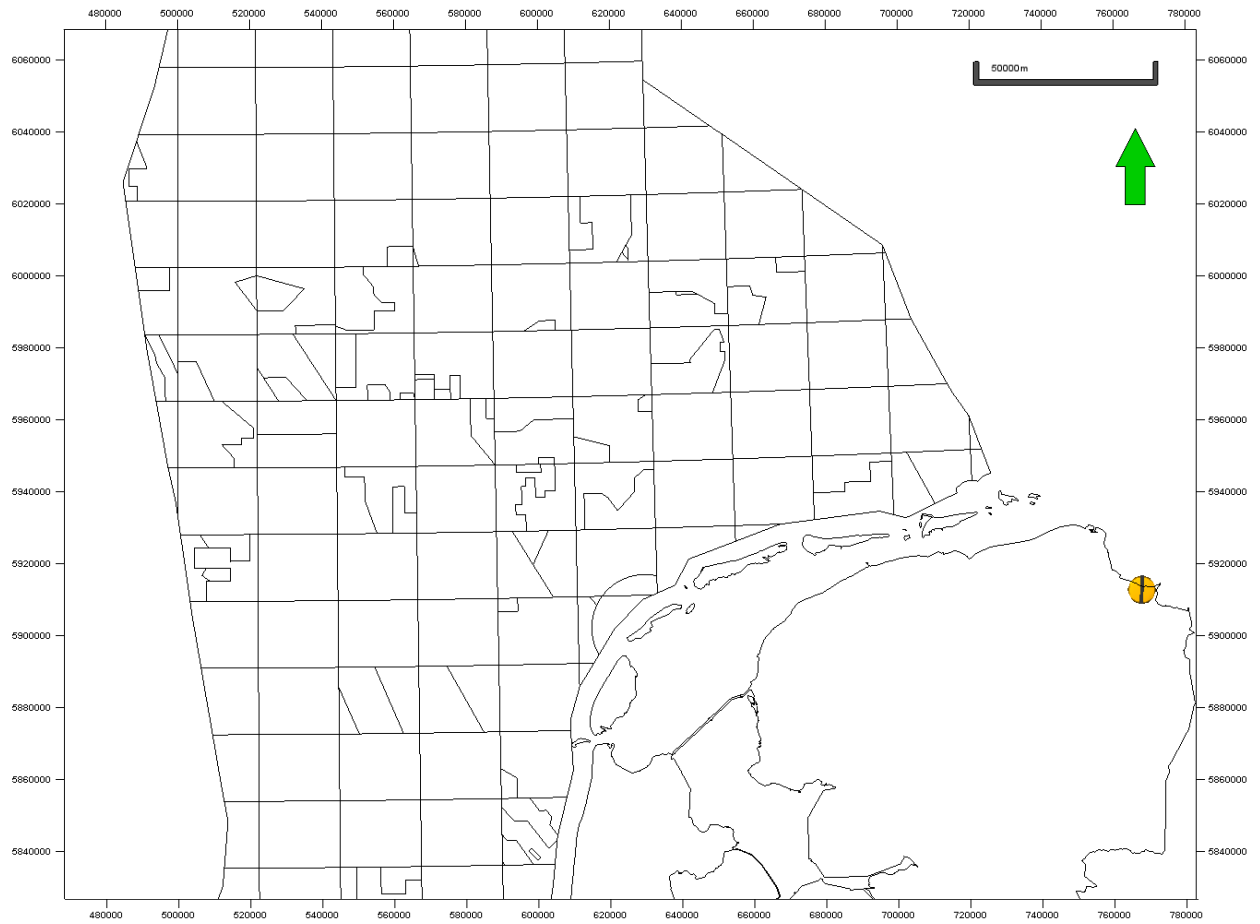


Figure 59: Dutch Stress Map indicating for a confidential well the average S_H direction.

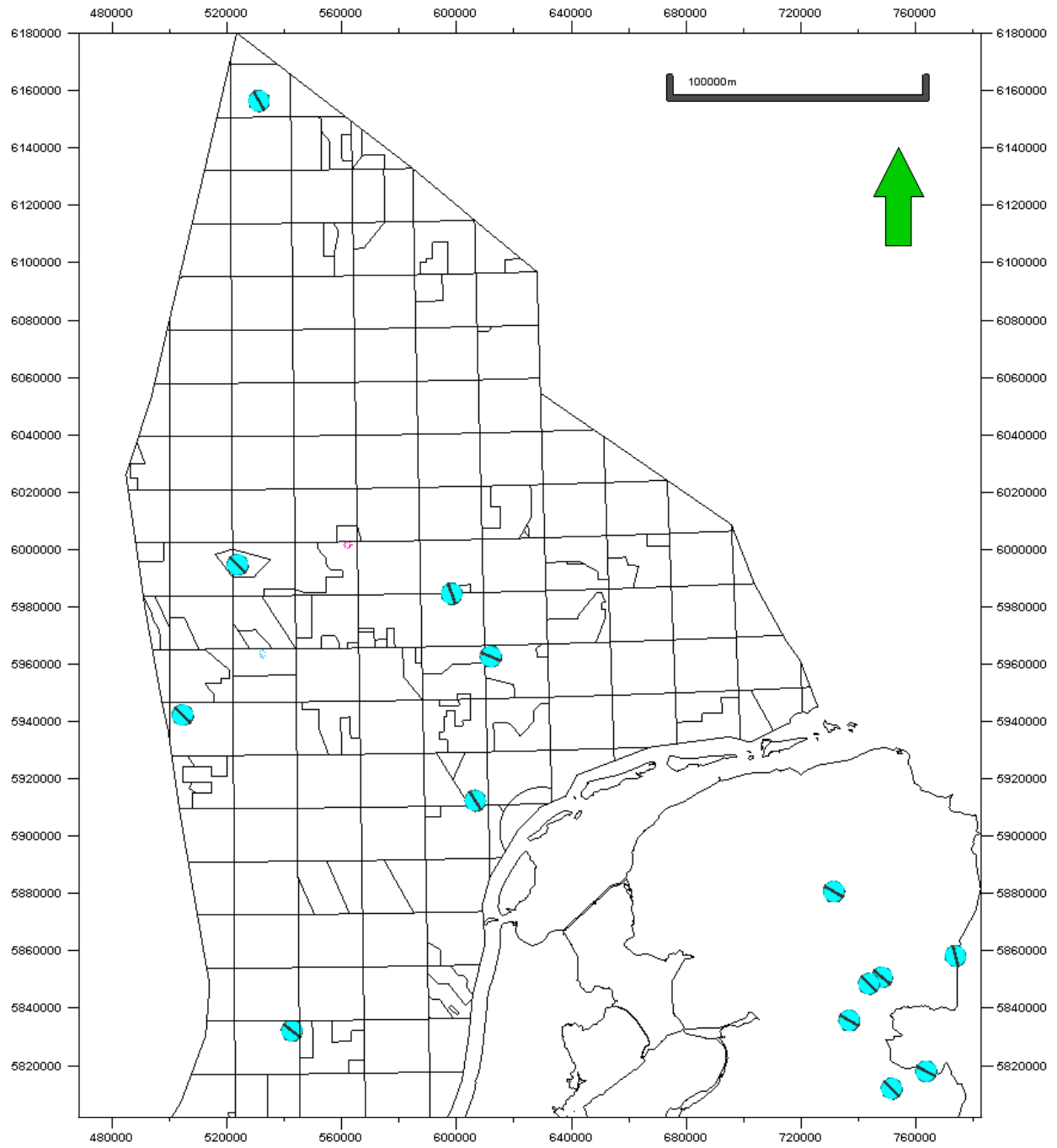


Figure 60: Dutch Stress Map indicating for each well the average S_H direction in the undefined stratigraphies.

Appendix F: Sources 1D geomechanical model

Table 31: Stratigraphic groups observed in well ZRP-01 with the corresponding bulk and fluid densities.

Stratigraphy	Bulk density [kg/m ³]	Source	Fluid density [kg/m ³]	Source
Upper North Sea Group	2050	Verweij et al. (2016)	1030	
Lower North Sea Group	1950	Verweij et al. (2016)	1030	
Chalk Group	2350	NAM B.V. (2013)	1030	
Rijnland Group	2350	NAM B.V. (2013)	1030	
Lower Germanic Trias Group	2350	NAM B.V. (2013)	1030	
Zechstein	2500	NAM B.V. (2013)	1030	
Rotliegend	2350		1030	
Limburg Group	2700		1030	

Table 32: Stratigraphic groups observed in well ZRP-01 with the corresponding elastic properties.

Stratigraphy	Young's Modulus [GPa]	Source	Poisson's ratio [-]	Source
Upper North Sea Group	2	NAM B.V. (2013)	0.30	NAM B.V. (2013)
Lower North Sea Group	2	NAM B.V. (2013)	0.30	NAM B.V. (2013)
Chalk Group	10	NAM B.V. (2013)	0.25	NAM B.V. (2013)
Rijnland Group	16	NAM B.V. (2013)	0.25	NAM B.V. (2013)
Lower Germanic Trias Group	16	NAM B.V. (2013)	0.25	NAM B.V. (2013)
Zechstein	50	NAM B.V. (2013)	0.30	NAM B.V. (2013)
Rotliegend	27.5		0.18	
Limburg Group	40	NAM B.V. (2013)	0.20	NAM B.V. (2013)

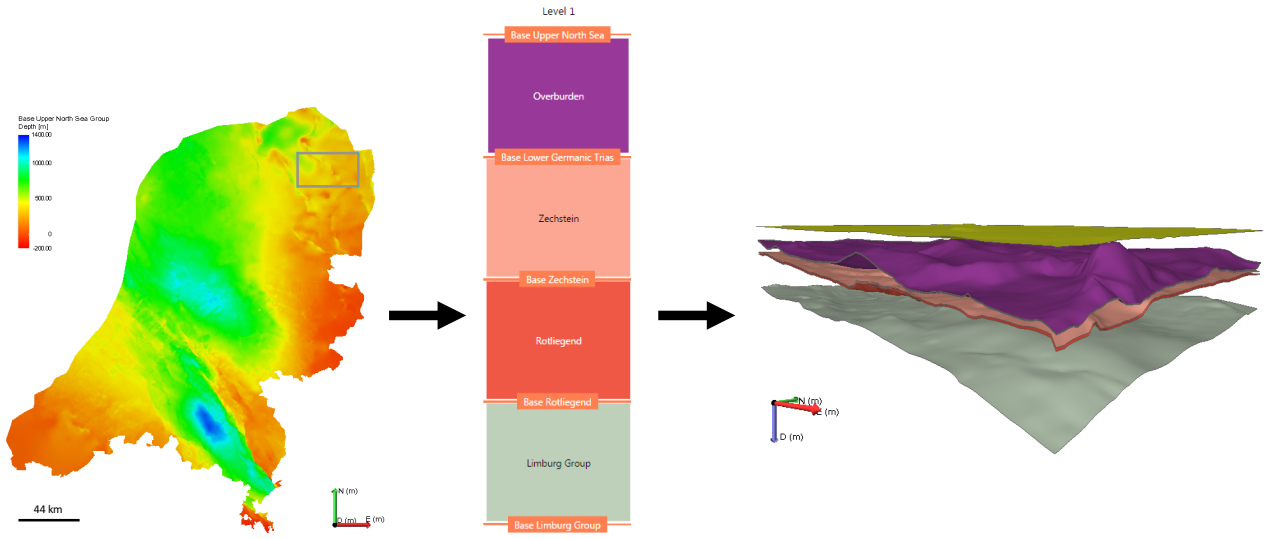
Appendix G: Workflow 3D geomechanical model

In addition to the model overview given in Section 8.1.1, this Appendix describes in detail the steps for developing the 3D geomechanical model in the JewelSuite Subsurface Modelling software.

The main input for the model discussed in Section 8 are the depth surfaces that have been mapped by NLOG (2015) for the Dutch onshore and which are publically available on their website. In Figure 39 the base of the Lower Germanic Trias Group has already been shown but the following base surfaces have been imported in the same way: Upper North Sea Group, Zechstein, Rotliegend and Limburg Group. With these horizons, a stratigraphic model is then created to define the different stratigraphic units and the order in which they occur. This is illustrated in step 2 of Figure 61 where the stratigraphic column of the investigated area is shown. Important to note is that this equal thickness column does not imply that the stratigraphic units have equal thicknesses in the actual 3D geomechanical model.

Subsequently, a 3D structural model is developed (step 3, Figure 61) by combining the imported depth surfaces, the stratigraphic model and a fault model. However, a fault model is not included in this particular structural model as no fault mapping has been performed for the investigated area. Following the construction of a 3D structural model, a 3D mesh structural model is created as shown in Figure 61. In JewelSuite, an empty 3D mesh structural model is defined after which the surfaces of the 3D structural model are assigned to this empty model. A mesh is then created for each surface by defining the so-called coarsening parameters. These parameters (*number of nodes on a single edge* and *mesh gradient*) determine the resolution of each surface and thus the computational time of the 3D mesh in Abaqus. For all four surfaces, 25 nodes have been assigned to each edge, whereas the mesh gradient (defined as the contrast between coarsened and non-coarsened parts of the surface), is set to one (Baker Hughes, 2016). Step 4 in Figure 61 shows the resulting mesh of the Base Lower Germanic Trias and it can be seen that JewelSuite makes use of a 3D tetrahedral mesh. This mesh type enables the modelling of irregular geometries such as salt domes, and therefore perfectly serves as input for this geomechanical simulation (Baker Hughes, 2016).

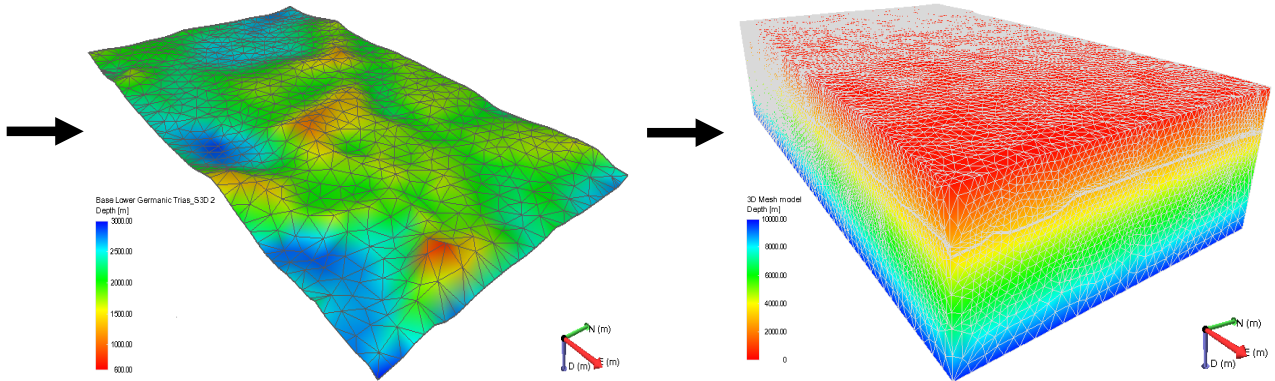
Prior to creating the 3D mesh in Abaqus, a quality control and validation procedure is performed to prevent errors during simulations. Besides that, the elements in the model have been defined as “non-pore pressure” implying that for each surface pore pressure should not be considered (Baker Hughes, 2016). The model is then exported to Abaqus and step 5 in Figure 61 shows the 3D mesh that has been made and which serves as basis for the actual simulation case. In the simulation case, the material properties (density, Young’s modulus and Poisson’s ratio) of each stratigraphic unit are defined, which has already been shown in Table 8. For this model, all other input parameters have not been changed and thus keep their default value. Finally, before exporting the 3D geomechanical model to Abaqus for simulation, the initial stress state is characterized by defining the azimuth of S_H and the ratios of S_H/S_v and S_H/S_v at specific depths.



(1) Depth surfaces

(2) Stratigraphic model

(3) 3D structural model



(4) 3D mesh structural model

(5) 3D mesh

Figure 61: Workflow for the development of a 3D geomechanical model in the JewelSuite Subsurface Modelling software.

Appendix H: Sources Dutch Stress Map database

Table 33: Overview of the data sources for the 56 new wells that have been identified in the TNO dataset.

Well	Data source
BLF-106	Western Atlas (1997). CBIL Structural Interpretation Report.
D12-A-02	Baker Atlas GEOScience (2003). Well D12-A-02: Processing and Geological Analysis of Borehole Images from CBIL and EARTH IMAGER Logs.
D15-05-S1	Baker Atlas GEOScience (2007). Well D15-05X: CBIL & EARTH Imager data - Processing and geological interpretation.
E17-A-01	Schlumberger (2009). Well E17a-A1: OBMI-UBI Processing & Structural Interpretation.
E17-A-02	Gas de France-Suez E&P Nederland B.V. (2009). Well Proposal E17a-A2.
E17-A-03	Schlumberger (2010). Well E17a-A3: OBMI-UBI Processing & Structural Interpretation.
E18-03	Schlumberger (1995). Well E18-03: Dipmeter and borehole break-out analysis.
E18-05	Schlumberger (2001). Well E18-05: Processing & Structural Interpretation of UBI Images.
E18-07	Schlumberger (2009). Well E18-07: EARTH Imager data - Processing and Geological interpretation.
F06-05	
F06-06-S2	
F16-04	Wintershall Noordzee B.V. (2002). Well F16-4: Processing & Structural Interpretation of FMS Images.
F16-05	Baker Atlas GEOScience (2004). Well F16-5: Processing and Geological Analysis of Borehole Images from CBIL and EARTH Imager Logs.
F16-A-03-S1	Baker Atlas GEOScience (2005). Well F16-A3: Processing and Geological Analysis of Boreholes Images from DCBIL Logs.
GSB-01	Schlumberger (2009). Mechanical Earth Model - GSB-1, Drenthe III License, Netherlands.
K05-12	Schlumberger (2002). Well K5-12: Processing & Structural Interpretation of UBI Images.
K05-ENC-04	Schlumberger (2000). Caliban Breakout Orientation Log.
K06-GT-03	Total E&P Netherlands (2010). Well K6-GT3: Hydraulic Fracturing Feasibility Study.
K07-09	Western Atlas (1996). Well K7-9: CBIL Interpretation Report.
K07-10	Western Atlas (1996). Well K7-10: CBIL Interpretation Report.
K07-FB-101	Western Atlas (1997). CBIL Interpretation Report of Well K07-11, K07-field.
K08-12-S1	Western Atlas (1997). CBIL Interpretation Report Well K08-12.
K09AB-B-02	Schlumberger (1997). Well K9-9: UBI Processing and Interpretation Report.
K12-G-09	Schlumberger (2009). Well K12-G9: OBMI Processing and Structural Interpretation.
K16-06-S1	Baker Atlas GEOScience (2004). Well K16-6X: Processing and Geological Analysis of Borehole Images from DCBIL and STAR Logs.
K18-08	Baker Atlas GEOScience (2006). DCBIL and HDIP data: Processing and Geological interpretation.
K18-09	
L05-06	Schlumberger (2001). Interactive Workstation Analysis of FMS Electrical Borehole Images.
L05-09	Schlumberger (2002). Well L5-9: Processing & Structural Interpretation of FMS Images.
L05-10	Baker Atlas GEOScience (2003). Well L5-10: Processing and Geological Analysis of Borehole Images from CBIL & HEXDIP Logs.
L05-11	Baker Atlas GEOScience (2008). STAR - CBIL Logs.
L05-B-02	Baker Atlas GEOScience (2003). Well L5-B2: Processing and Geological Analysis of Borehole Images from CBIL and HEXDIP Logs.
L05-C-02-S1	Baker Atlas GEOScience (2005). Well L5-C2X: Processing and Geological Analysis of Borehole Images from DCBIL and EARTH Imager logs.
L06-06	Baker Atlas GEOScience (2004). Well L6-6: Processing and Geological Analysis of Borehole Images from DCBIL and EARTH Imager Logs.
L08-14-S1	Schlumberger (1998). Well L8-14: Formation Microscanner (FMS) - Processing & Interpretation Report.
L08-15	Schlumberger (2001). Well L8-15: Slimhole Formation Microscanner (FMS) - Processing & Interpretation Report.
L08-16-S1	Baker Atlas GEOScience (2004). Well L8-16X: Processing and Geological Analysis of Borehole Images from CBIL and EARTH Imager Logs.
L08-P-05-S1	Schlumberger (1997). Well L/8-P5X: UBI Processing and Interpretation Report.
L08-P4-02-S2	Schlumberger (2001). Well L8-P4-02x: Ultra-Sonic Borehole Imager (UBI) - Processing & Interpretation Report.
L09-12	Z&S Geology Ltd. (1996). Well L09-12: CBIL Image Interpretation.
L10-33	Schlumberger (1998). Well L10-33: Formation Microscanner (FMS) - Processing & Interpretation Report.
L10-M-01	Schlumberger (1999). Well L10-34: Formation Microscanner (FMS) - Processing & Interpretation Report.
L14-07	Schlumberger (1998). Well L14-7: Formation Microscanner (FMS) - Processing & Interpretation Report.
M07-06	Baker Atlas GEOScience (2004). Well M7-6: Acoustic Analysis.
P02-NE-02	Schlumberger (1997). Well P2-NE-2 Pilot: UBI Processing & Interpretation Report.
P06-10	Schlumberger (2001). Well P6-10: Fullbore Formation Micro-Imager (FMI) - Processing & Interpretation Report.
P06-D-01	Baker Atlas GEOScience (2000). Well P6-9: CBIL Images and Structural Results.
P08-07	Baker Hughes (2011). Well P08b-07: Processing and Interpretation of EARTH Imager and CBIL Images.
P09-09	Schlumberger (2000). Caliban Breakout Orientation Log.
P09-09-S1	Schlumberger (2000). Caliban Breakout Orientation Log.
P18-A-06	Schlumberger (1997). Well P18-2A6: UBI Processing & Interpretation Report.
Q01-28	Baker Atlas GEOScience (2009). Well Q1-28: Structural Interpretation of EARTH Imager and CBIL Images.
Q04-08	Schlumberger (1998). Fullbore Formation Micro-Imager (FMI) - Processing & Interpretation Report.
Q13-07-S2	Western Atlas (1990). CBIL Image Analysis of Well Q13-07 - Final Report.
Q13-12	Schlumberger (2011). Well Q13-12: OBMI-UBI Processing & Geological Interpretation.